RESONANT TERAHERTZ TRANSMISSION OF PLASMONIC SUBWAVELENGTH HOLE ARRAYS

BY

ABUL K. AZAD

Bachelor of Science
University of Dhaka
Dhaka, Bangladesh
1996

Master of Science
Oklahoma State University
Stillwater, OK USA
2003

Submitted to the Faculty of the
Graduate Collage of
Oklahoma State University
in partial fulfillment of
the requirements for
the Degree of
DOCTOR OF PHILOSOPHY
May, 2006

RESONANT TERAHERTZ TRANSMISSION OF PLASMONIC SUBWAVELENGTH HOLE ARRAYS

Thesis approved:

Dr. Weili Zhang

Thesis Advisor

Dr. Alan Cheville

Dr. Daniel Grischkowsky

Dr. Xincheng Xie

Dr. A. Gordon Emslie

Dean of the Graduate College

ACKNOWLEDGEMENT

First of all, I would like to express my heartfelt gratitude to Dr. Weili Zhang, my major advisor, for providing the opportunity to be a part of the THz research group at Oklahoma State University. His patient guidance, encouragement, and scientific excellence made possible the completion of this thesis. Over the past few years he has been giving me all kind of supports that one could expect from an ideal advisor.

I would also like to thank Dr. Daniel Grischkowsky for introducing me in the world of THz, for supporting me in hard times, and for guiding me in the spirit of scientific truth and excellence. My appreciation is extended to Dr. Alan Cheville for his timely delivered suggestions and for continuous help to overcome scientific dilemma in a simplified neatest way. I would like to thank Dr. Xincheng Xie for his stimulating lectures and discussions about the electromagnetism and for his capability of making the difficult concept understandable.

A very special thanks to Dr. John O'Hara who has been supporting me from the day I entered to the THz group, Dr. Rajind Mendis, Yuguang Zhao, Ranjan Singh, Adam Bingham, and Matt Reiten.

A heartfelt thanks to my late parents - Muzaffar and Abishkar; and my sisters - Monu, Renu, Tibbat, Parul, Maloti, Manik, and Mukti. Their continuous encouragement and support always inspires me to accomplish outstanding achievement.

A unique gratitude to my beautiful wife, Rubina, and my angel daughter, Aelma. Rubina makes my life lively here in Stillwater and gives me a nice home full of loves, happiness and attentions. Her continuous efforts and goodwill made it possible for me to pay full attention to my research. She is exceptional.

Finally, I like to express my thanks to the Almighty Allah to reward me such a life and excellent opportunity for the higher study.

TABLE OF CONTENTS

Chapter **Page**

LIST OF FIGURES

Figure **Page**

LIST OF TABLES

LIST OF THE SYMBOLS

SPPs	Surface plasmon polaritons
ε_m	Complex dielectric constant of metal
ε_{rm} , ε_{r2}	Real dielectric constant of metals
ε_{im} , ε_{i2}	Imaginary dielectric constant of metals
ω_p	Plasma frequency
ω	Angular frequency, rad/s
N	Free electron density
e	Electric charge of an electron
m_0	Mass of the free electron
h	Plank's constant
$\boldsymbol{E}(\mathbf{r},t)$	Electric field
$\boldsymbol{B}(\mathbf{r},t)$	Magnetic flux density
$\boldsymbol{E}_z$	Electric field amplitude in z-direction
$\boldsymbol{E}_x$	Electric field amplitude in x-direction
$\boldsymbol{H}_y$	Magnetic field amplitude in y-direction
$\boldsymbol{D}$	Electric flux density

c	Velocity of light in free space, 3×10^{8} m/s
ρ	Charge density
J	Current density
$\boldsymbol{P}$	Polarization
$\boldsymbol{M}$	Magnetization
ε_0	Permittivity of free-space, 8.854×10^{-12} F/m
μ_0	Permeability of free-space, $4\pi\times10^{-7}$ H/m
σ_s	Surface charge density
K	Surface Current density
TE	Transverse electric
TM	Transverse magnetic
k_x	Wavevector along x-direction
k_z	Wavevector along z-direction
ε_1	Dielectric constant of the dielectric medium
ε_2	Complex dielectric constant of metal
Δk_x	Change in the wavevector along x-direction
θ_0	Angle of incidence of light
a, L	Grating period
G	Grating momentum
n, m	Order of mode
k_{sp}	Wavevector of surface plasmon polaritons

TDS	Time-domain-spectroscopy
SOS	Silicon-on-sapphire
w_2, w_3	THz beam waist
E_{ref}	Reference electric field amplitude
E_{sam}	Sample electric field amplitude
d	Diameter of the aperture
λ	Wavelength in free space
λ_{sp}	Resonance wavelength of SPP
$\lambda_{Wwood}^{m,n}$	Wavelength of Wood's anomaly minima
ε_r	Real dielectric constant
ε_i	Imaginary dielectric constant
σ_r	Real conductivity
σ_i	Imaginary conductivity
m^*	Effective mass of free carrier
Γ, ω_Γ	Carrier damping rate
RIE	Reactive ion etching
UV	Ultra violet
SEM	Scanning electron microscope
LDPE	Low density poly-ethylene
MAOS	Metal-array-on-silicon
FMA	Free-standing-metal-array
$\varepsilon_\infty, \varepsilon_{Si}$	High frequency dielectric constant

σ_{rm}	Real conductivity of metal
σ_{im}	Imaginary conductivity of metal
$T_{amplitude}$	Amplitude transmission
T_{Power}	Power transmission
L_x	Propagation length of SPP
δ_m	Skin depth of metal
τ	Carrier collision time
C_n	Fraction of carrier initial velocity retained after *n*th collision

CHAPTER I

INTRODUCTION

An experimental study of extraordinary terahertz (THz) transmission through subwavelength metallic hole arrays structured on metal films, doped semiconductors, and optically excited semiconductor is presented. The extraordinary transmission of THz pulses through such a metallic or metal-like hole arrays is attributed to the resonant excitation of surface plasmon polaritons, the electromagnetic waves that are trapped on the conducting surface because of their interaction with the free electrons of the conductors. The resonant interactions between the surface charge oscillation of metals and the electromagnetic field of incidence photons are known as surface plasmon polaritons (SPPs).

1. 1 Extraordinary optical transmission and SPPs

The extraordinary transmission of light through the arrays of subwavelength holes perforated on an optically thick metallic surface was discovered by Ebbesen [1, 2]. The zero order transmission was found to be orders of magnitude higher than that predicted by the standard aperture theory of metallic film. However, similar transmission measurement on a nonmetallic hole arrays made from germanium film has shown no enhanced transmission. The discovery of Ebbesen has inspired great interest to explore the underlying physics.

Extensive theoretical and experimental studies have been carried out to explain the physical phenomena behind the enhanced optical transmission process [3-9]. The dependence of optical transmissions through the metallic hole arrays were investigated by varying different parameters of the array's structure such as period of the array, diameter of the holes, thickness of the metal films, and constituent metals. The experimental result demonstrates that the transmission spectra consist of well defined maxima and minima whose positions can be controlled by changing periods of the arrays. The metallic subwavelength hole arrays are considered as the active optical elements. The SSPs excited on periodically structured metal by the incident light tunnel through the subwavelength holes and reradiate as light on the opposite side. Schröter *et. al.* [3] performed numerical calculations for the transmission through silver gratings with very small slits and observed a qualitative agreement of enhanced transmission with Ebbesen's results. Schröter's evaluation of near field in the media above and below the metals suggested that extraordinary transmission maxima corresponds to the excitation of surface plasmons on either sides of the metal films.

The optical transmission of metallic subwavelength hole arrays shows that the constituent metals play a crucial role in controlling the enhanced transmission [7]. It has also been demonstrated that the transmission enhancement depends only on the dielectric properties of the metals within the skin depth of the two in-plane surfaces but not on those of the core material of the arrays and the hole walls. In optical frequencies the optimum metals is described by the ratio of the real (ε_{rm}) and imaginary (ε_{im}) dielectric constants. Metals with higher values of $|\varepsilon_{rm}/\varepsilon_{im}|$ show higher enhancement with smaller resonance line width. SPPs are very sensitive to the dielectric constant of the surrounding materials. By changing the dielectric of the surrounding medium one can essentially control the resonance peak wavelength as well as the transmission intensity of the light. In Ref. 8 Altewischer demonstrated the true quantum nature of the surface plasmons. In the earlier experimental and theoretical works, it was assumed that the hole shape or polarization of the incident light does not have any significant contribution to the enhanced transmission. However, the recent works demonstrated strong influence of hole shape and polarization of incident light on the enhanced transmission [10, 11]. Lezec *et. al.* [12] demonstrated, it is possible to realize enhanced and collimated transmission even through a single hole. To obtain this enhancement and collimation both surfaces of the metallic film should have periodic corrugations [13, 14].

The extraordinary transmission through subwavelength hole arrays is expected to find numerous applications in near-field microscopy, high resolution nano-photolithography, high-density optical data storage and optical displays. Such metallic hole arrays have promising use as active optical filters whose band pass wavelength can be changed dynamically when incorporating with the piezo-electric material as the dielectric constant of such surrounding medium changes with externally applied voltage. The interesting properties of SSPs can localize and concentrate the electromagnetic waves in the subwavelength scale which lead to the potential applications in developing integrated photonic devices [15, 16].

1. 2 THz SPPs and enhanced THz transmission

Most of the work related to the extraordinary transmission through subwavelength metallic hole arrays has been accomplished in the optical frequency regime where the optimal metals are characterized by the real part of dielectric constant whose absolute value is normally much higher than the corresponding imaginary component. At longer wavelength, such as THz and microwave regimes, imaginary dielectric constant is orders of magnitude higher than that of the corresponding real component. The ratio $|\varepsilon_{rm}/\varepsilon_{im}|<<1$ was believed to be the limitation to observe the enhanced transmission in the longer wavelength regime. However, significant enhancement of the transmission can be realized even for the small values of $|\varepsilon_{rm}/\varepsilon_{im}|$ by appropriate periodic corrugation on the metallic surface. As mentioned by Moreno *et. al.* [14], the corrugation on the surface leads to an effective impedance for the surface modes which favors to the resonant coupling of the surface plasmons with incident electromagnetic wave and hence facilitates enhanced transmission.

Very recently, enhanced transmissions of THz electromagnetic waves have been demonstrated through subwavelength metallic hole arrays [17-23]. Enhanced THz transmission through the subwavelength metallic hole arrays is attributed to the resonant excitation of THz SPPs. Enhanced transmission also observed through a single hole while incorporating with the periodic corrugations on both surfaces. The experimental results showed that the hole shape had a significant effect on the THz transmission magnitude. Dielectric properties of the metals in THz region approach to the ideal metal which can lead to observe some interesting spectral characteristics that are not present in the optical region, for example, observation of fractional SPP propagating mode [19] on metal-silicon interface. THz SPPs were also excited at an interface between a thin dielectric film and metal surface, demonstrating the potential applications of SPPs in bio-sensing [24].

In the THz region highly doped semiconductors pretend to have metallic behaviors as the real part of dielectric constant ε_{rm} possesses a negative value. Doped semiconductors are considered as alternatives of metals to demonstrate enhanced THz transmission. Extraordinary THz transmissions have been demonstrated through the subwavelength hole arrays made from doped silicon [25-27]. Effects of the hole shape, polarization of the incident THz beam, and the arrays-thickness have been studied. It has also been observed that higher enhancement can be observed with silicon that has higher doping concentration. Transmitted THz peak is highly sensitive to the change of the of the dielectric properties of the surrounding materials. THz transmissions through the subwavelength hole arrays made from semiconductors have been controlled by thermal switching [28-29]. By changing the temperature which eventually changes the free carrier concentration in the semiconductor, it was successfully demonstrated that such an array can be an active elements for the THz photonic circuits.

In the THz region, surface plasmons resonance has potential applications in plasmonic terahertz interconnects, THz imaging, THz sensing, and next generation photoconductive antennas for THz generation and detection. Enhanced THz transmission might also be used for THz near field microscopy. Incorporating with THz wave guides [30] and planar THz quasioptics [31], subwavelength hole arrays capable to couple with incident THz radiation via resonant SPPs can lead to the fabrication of novel photonic devices.

1. 3 Organization of this thesis

The purpose of this thesis is to demonstrate the enhanced THz transmission through subwavelength hole arrays and the understanding of the physical mechanism behind this high transmission. THz transmission through such hole arrays made from doped silicon and metal films of thickness ranging from optically-thick to optically-thin have been studied. SPPs enhanced resonance peak is demonstrated to have high sensitivity to the change of surrounding dielectric medium. Hole arrays made from electrically poor conductors can also be used for efficient resonant transmissions beside those made of good conductors. Metallic hole arrays of sub-skin-depth thickness can contribute to the formation of SPPs and nine tenths of maximum transmission can be achieved by an array of metal thickness only one third of the skin depth when compare with the transmission of an optically thick array. SPPs resonances have been observed in THz transmission spectra through the subwabelength hole arrays made from fairly transparent silicon under intense optical illumination.

Chapter II outlines the conceptual formulation of surface plasmons polaritons within the frame work of classical electrodynamics. The dispersion relation of SPP for metal-dielectric interface is presented. An over view of coupling mechanism of SPPs to the freely propagated electromagnetic radiation is given. Several experimental techniques for the efficient coupling of electromagnetic wave have been discussed with examples in both optical and THz frequency ranges.

Chapter III provides the detailed description of the experimental setup for terahertz time-domain spectroscopy (THz-TDS). Optoelectronic techniques for transmission and detection of pulsed THz radiation are described along with the beam steering and collimating optics. A focused beam THz-TDS system capable of focusing down the THz beam up to a beam waist of 3.5 mm is discussed. A conceptual understanding of THz-TDS and frequency dependent parameters extraction from the time domain data are also explained.

Chapter IV presents the experimental result of THz transmission through subwavelength hole arrays made from doped silicon. First part describes a theoretical calculation of the complex dielectric constants based on the simple Drude theory. The second part presents sample fabrication process. Third part shows the experimental results of polarization dependent THz transmission through elliptical hole arrays. Next part compares the experimental results with theoretical calculation. The last part of this chapter shows the experimental results of the effect of surrounding materials.

Chapter V describes SPP-enhanced THz transmission through the hole arrays made from different metals. Effect of dielectric constants on peak amplitude transmission has been investigated in this chapter. First section outlines the sample fabrication process. Second section shows the calculation of dielectric properties of metal. Next two sections show the data acquisition and data analysis methods. Section 6 describe the experimental results of transmission through metallic hole arrays made on silicon substrate. THz transmission through freestanding metallic hole arrays made from different metals is discussed in section 7. The last section gives a qualitative explanation of the transmission enhancement based on the propagation length of surface plasmons on metal surfaces. Experimental results demonstrate that metal with higher propagation length shows higher enhancement.

Chapter VI presents the effect of metal thickness on enhanced transmission. Experimental result demonstrates that the transmission enhancement maximizes when the metal thickness approaches the skin depth. Enhanced transmission, as high as nine tenths of maximum value, can be achieved with an hole arrays having metal thickness of only one-third of the skin depth. First section represents a theoretical formulation of skin depth of metals at THz frequency and then calculates skin depths from the published values of dielectric constant of metals. Next section shows the sample fabrication technique. Third section shows measured THz pulses and spectra. Fourth section presents the experimental results of THz transmission. A critical thickness has been observed below which resonance structure is absent in the transmission spectrum. Above the critical thickness the resonance structure appears in the spectrum whose amplitude increases exponentially with film thickness and saturates towards the maximum when film thickness attains skin depth.

Chapter VII presents the demonstration of optically excited SPPs. A subwavelength hole array made from lightly doped silicon which is fairly transparent to the THz radiation in the absence of optical excitation. First section outlines the experimental details and the next two sections explain the THz transmission under the influence of intense optical illumination. Next section shows the change of the dielectric constants with optical pump power. The dielectric properties of the arrays changes dynamically with external optical excitation. Under the influence of the intense optical excitation the real part of the dielectric constant turns to negative and hence supports SPPs. The transmission properties of the unexcited arrays show complicated out-of-plane photonic crystal effect and change to SPPs resonance peak when excited with 111 mW of average optical power. Finally, Chapter VIII briefly summarizes the thesis.

CHAPTER II

THEORY OF SURFACE PLASMONS POLARITONS

2. 1 Surface Plasmons Polaritons (SPPs)

A plasmon is the quantum of the collective excitation of free electrons in solids. By ignoring the lattice effect in first approximation, the free electrons of a metal can be treated as an electron-plasma or an electron-liquid of density of about 10^{23} cm^{-3}. Consider a longitudinal density fluctuation of free electrons propagates through the volume of the metal. The dielectric constant of such a metal can be written as $\varepsilon_m(\omega) = 1 - (\omega_p/\omega)^2$, where $\omega_p = \sqrt{Ne^2/m_0}$ is the bulk or volume plasma frequency, N is the volume electron density. The quanta of these volume plasmons have energy $h\omega_p$ of the order of 10 eV. The electromagnetic properties related to the electron plasma effects are significantly different from the properties of ordinary dielectrics. Electromagnetic radiation having frequency smaller than the plasma frequency can not propagate through such a medium because the dielectric constant possesses a negative value. In this frequency range the wavevector of the electromagnetic radiation is imaginary and hence no propagation mode exists in such medium.

Surface plasmons are the electron plasma oscillations near a metal surface. Ritchie [32] has theoretically proved that the surface plasmons arise from the formal solution of Maxwell's equations. Maxwell's theory shows that electromagnetic surface wave can propagate along a metallic surface or metallic film with a broad spectrum of eigen frequencies from $\omega = 0$ to $\omega = \omega_p / \sqrt{2}$.

In general, the origin of an electromagnetic surface excitation is the physical displacement of charge carriers, atoms, or molecule which forms a time dependent polarization of magnetization. Due to the Coulomb restoring forces displaced charge undergoes acceleration and hence an electromagnetic field forms at the metallic surface. A combined excitation consisting of surface plasmon and a photon is called a surface plasmon polariton (SPP). A SPP is a collective oscillation of charges formed at a metal-dielectric interface as a consequence of excitation by photons. The SPP has dual characteristics, it shows plasma like character inside the metal while free electromagnetic type character inside dielectric [33]. Electromagnetic fields associated with SPPs decay exponentially in to the space perpendicular to the surface and have their maximum in the surface [34] as shown in Fig. 2-1.

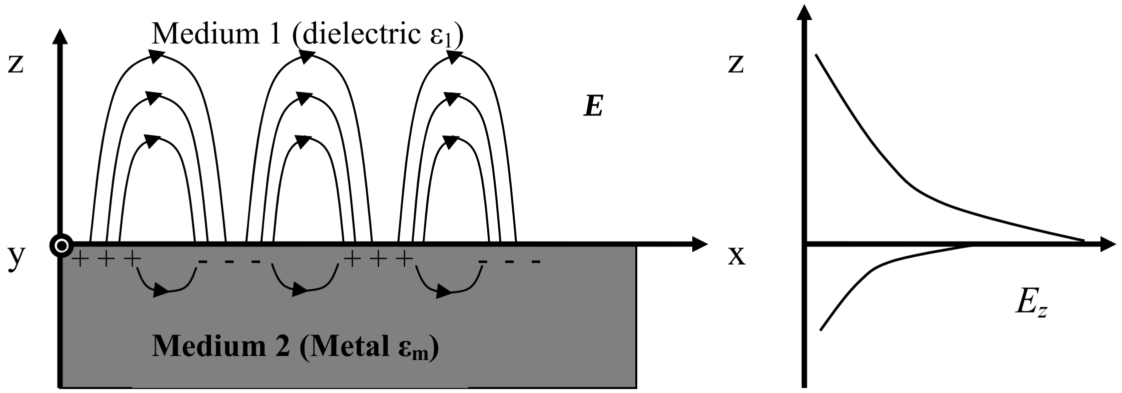

(a) (b)

Figure 2-1 (a) Schematic diagram of SPPs propagating on a surface defined by xy plane at z =0 along x direction. (b) Exponentially decay field $\boldsymbol{E_z}$ as a function of z, where z>0 is inside dielectric and z<0 is inside metal. SPP is p-polarized wave because electric field vector ***E*** is in the plane of incident (xz). Magnetic field $\boldsymbol{H_y}$ is along y direction out of the page.

2. 2 Dispersion relation of SPPs

The dispersion relation associated with SPP can be obtained by solving Maxwell's field equations under the appropriate boundary conditions. The Maxwell's equations are a set of coupled first order partial differential equations state how an electric field $\boldsymbol{E}(\mathbf{r}, t)$ and a magnetic field $\boldsymbol{B}(\mathbf{r}, t)$ are related to each other. Maxwell's equations can be written as [34]

$$\nabla \times \boldsymbol{E} = -\frac{1}{c}\frac{\partial}{\partial \boldsymbol{t}}\boldsymbol{B}$$

$$\nabla \times \boldsymbol{H} = J + \frac{\partial}{\partial \boldsymbol{t}}\boldsymbol{D} \tag{2-1}$$

$$\nabla \bullet \boldsymbol{D} = \rho$$

$$\nabla \bullet \boldsymbol{B} = 0$$

where, ***E*** and ***H*** are the electric and magnetic field quantities, ***D*** and ***B*** are the electric and the magnetic flux density, c is the speed of light in vacuum, ρ and ***J*** are the charge and the current density, respectively. When dealing with fields in matter, ***D*** and ***H*** are related to ***E*** and ***B*** through the polarization ***P*** and magnetization ***M*** of the matter as,

$$\boldsymbol{D} = \varepsilon_0 \boldsymbol{E} + \boldsymbol{P}$$
$$\boldsymbol{H} = \frac{1}{\mu_0}\boldsymbol{B} - \boldsymbol{M}$$

The solutions of Maxwell's equations must satisfy a set of boundary conditions at the interface between media. The components of ***D*** and ***B*** on the either side of the boundary which are perpendicular to the interface can be written as $(D_{1\perp} - D_{2\perp}) = \sigma_s$ and $(B_{1\perp} - B_{2\perp}) = 0$. Again the tangential components of ***E*** and ***H*** on either side of the boundary are therefore related by $(E_{1\|} - E_{2\|}) = 0$ and $(H_{1\|} - H_{2\|}) = K$ with σ_s and K are the surface charge and surface current density, respectively.

In order to solve Maxwell's equation for a nonmagnetic conductor, we set the magnetic permeability μ=1 and for simplicity set $\rho = \sigma_s = K = 0$. To find the appropriate boundary conditions, the definition of the SPP is considered again. SPP is the coherent fluctuation of charges on the surface of a metal-dielectric interface. These charge fluctuations, which can be localized in the z-direction within Thomas-Fermi screening length, are excited and accompanied by a p-polarized (TM) electromagnetic field. The field is maximum at the surface z = 0 and vanish at $|z| \rightarrow \alpha$ when the surface lies in the xy plane at z = 0, as shown in the Fig. 2-2. The medium 1 and medium 2 on each side of the interface are homogeneous.

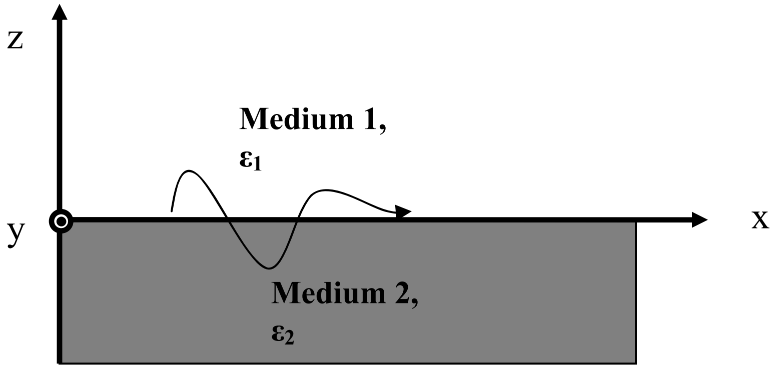

Figure 2-2 Schematic diagram of p-polarized SPP propagating in a surface defined by xy plane. Electric field decays exponentially in both mediums perpendicular to the surface. Direction of magnetic field $\boldsymbol{H_y}$ is out of the page.

To described such a wave three field components are required, which are $\boldsymbol{E_x}$, $\boldsymbol{E_z}$, and $\boldsymbol{H_y}$. The general form of the electric field can be written as,

$$\boldsymbol{E} = \boldsymbol{E}_0^{\pm} \exp\left[+i\left(k_x x \pm k_z z - \omega t\right)\right] \tag{2-2}$$

where, + for z ≥ 0 in medium 1, - for z ≤ 0 in medium 2, k_z is the imaginary wave vector along z-direction ,and k_x is the wave vector along x-direction. The fields can be written as,

$$\begin{aligned} \boldsymbol{E}_{xj} &= \hat{x}E_{xj}\exp\left[+i\left(k_{xj}x \pm k_{zj}z-\omega t\right)\right] \\ \boldsymbol{E}_{zj} &= \hat{z}E_{zj}\exp\left[+i\left(k_{xj}x \pm k_{zj}z-\omega t\right)\right] \quad j=1,2 \\ \boldsymbol{H}_{j} &= \hat{y}H_{yj}\exp\left[+i\left(k_{xj}x \pm k_{zj}z-\omega t\right)\right] \end{aligned} \tag{2-3}$$

where j = 1, 2 represents the fields inside medium 1 and medium 2. For j = 1 '+' sign has to be considered and for j = 2 '-'sign has to be considered in equation 2-3.

By solving the Maxwell's equations with appropriate boundary conditions (detailed calculation is shown in appendix A), we obtained,

$$\begin{aligned} k_x^2 &= \varepsilon_1\left(\frac{\omega}{c}\right)^2 - k_{z1}^2 \\ k_x^2 &= \varepsilon_2\left(\frac{\omega}{c}\right)^2 - k_{z2}^2 \end{aligned} \tag{2-4}$$

Eq. 2-4 gives
$$k_{z1}^2 = \left(\frac{\omega}{c}\right)^2 \frac{\varepsilon_1^2}{\varepsilon_1+\varepsilon_2} \tag{2-5}$$

and
$$k_x = \frac{\omega}{c}\sqrt{\frac{\varepsilon_1\varepsilon_2}{\varepsilon_1+\varepsilon_2}} \tag{2-6}$$

Eq. (2-6) is the dispersion relation of SPPs. The quantities ε_1 and ε_2 are complex dielectric constant of materials which make the wave vector k_x a complex quantity. The decay length of the SPP along the propagation direction can be described by the imaginary part of k_x .

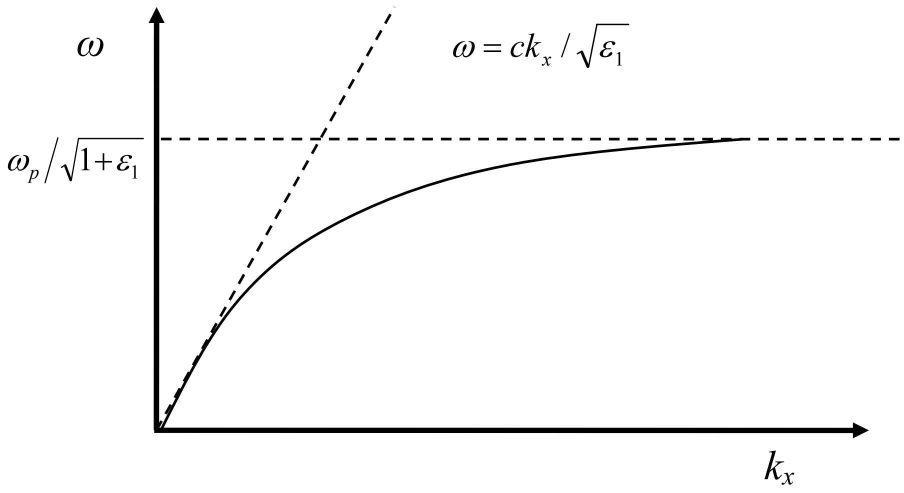

Figure 2-3 Solid line represents the dispersion relation of SPP and the dashed angled line represents the dispersion relation of light. At low frequency regime the SPP approaches to the light but still on the right of the light line. For $k_x \to \infty$ dispersion curve approaches to $\omega_p / \sqrt{1+\varepsilon_1}$.

The dispersion relation of SPP is schematically shown in Fig. 2-3 together with light dispersion in dielectric. The solid line represents the SPP and the dashed line represents the light. We see from the figure that at low frequencies the SPP dispersion relation follow the same slope as the freely propagating electromagnetic wave in medium 1. At high frequencies the SPP dispersion relation saturates at $\omega_p / \sqrt{1+\varepsilon_1}$, where ω_p is the plasma frequency of the conductor (medium 2). The SPP dispersion curve lies on the longer wave vector side and therefore, has a larger wave vector than that of a freely propagating wave, so the SPP cannot radiate light or cannot be excited by the freely propagating electromagnetic wave illumination from the adjacent medium. Therefore, light illuminating a smooth surface can not be directly coupled to the surface plasmon polaritons. Special experimental arrangement is essential to couple incident light to the SPPs.

2. 3 Excitation of SPP

Surface plasmons can be excited either by electrons or by photons. Electrons, penetrating a solid, transfer their momentum and energy to the electrons of the solid. The electrons in the solid scattered in different directions. The projection of the scattered momentum in the surface can excite surface plasmons. Electrons are good tool to study the dispersion relation at larger surface plasmon wave vector k_x. Electrons are not suitable for studying the surface plasmon properties at very low k_x values.

It has been seen from the dispersion relation that surface plasmon's wave vector lies on the right of the light line. At a certain frequency, the SP has larger wave vector than the light wave vector. Light cannot excite the surface plasmons of a smooth surface directly. Special arrangement is required to excite the surface plasmon with the incident photons. In order to excite SPs by the incident photon of energy $\hbar\omega$, the wave vector of photon $\hbar\omega/c$ has to increase by a value of Δk_x. There are several methods to excite SPs with electromagnetic radiations which are described in next sub-sections.

2. 3. 1 Grating Coupler

In this method, a metal grating of appropriate grating constant has been employed to couple the incident photon to excite the SPPs. Consider a light of wave vector $k = \omega/c$ incident on a grating of grating constant a, at an angle θ_0. The component of the incident wave vector on the surface can have wave vector

$$k_x = \frac{\omega}{c}\sin\theta_0 \pm nG \tag{2-7}$$

where, n is an integer, and $G = \frac{2\pi}{a}$ is the grating momentum. The SPPs takes place when the wave vector on the surface (2-7) matches with the SP's wave vector given by Eq. (2-6),

$$\begin{aligned} k_x &= \frac{\omega}{c}\sin\theta_0 \pm nG = \frac{\omega}{c}\sqrt{\frac{\varepsilon_2}{1+\varepsilon_2}} = k_{sp} \\ k_x &= \frac{\omega}{c}\sin\theta_0 \pm \nabla k_x = k_{sp} \end{aligned} \tag{2-8}$$

which shows that by appropriate choice of grating constant helps the incident light to be coupled with the surface plasmons. A reverse process of converting light to surface plasmon polaritons can be accomplished by similar arrangement. In this case, the wave vector k_{sp} a propagating SPs along a grating or rough surface can be reduced their wave vector by an amount Δk_x to transform into light. THz SPPs has been demonstrated using grating coupler [35].

2. 3. 2 ATR Prism coupler

Two basic configurations of ATR prism coupling methods are employed depending on the thickness of the metal. The schematic diagrams are shown in Fig. 2-4. In this method the electromagnetic wave is transformed into an evanescent electromagnetic field which may couple to SPPs.

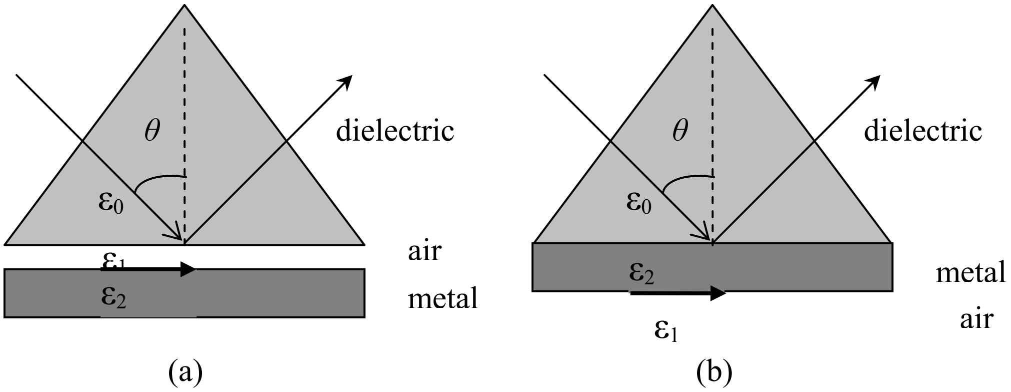

Figure 2-4 (a) Otto configuration: dielectric or air lies in between metal surface and prism. (b) Kretschmann-Reather configuration: Metal surface is in contact with prism.

To excite SPPs on a thick metal Otto configuration (Fig. 2-4 (a)) is the right choice. In this case the prism where the total internal reflection occurs is placed close to the metal surface, so the photon tunneling occurs through the air gap between the prism and metal surface. Recently, this technique has been demonstrated successfully by O'Hara [36] for exciting THz SPPs.

In the Kretschmann configuration (Fig. 2-4 (b)), the metal film is attached to the dielectric prism base. When metal film is illuminated through the dielectric prism at an angle of incidence greater than the angle of total internal reflection, component of the photon wave vector matches with the SPPs at the metal-air interface and excites the SP. Efficiency of SP coupling decreases as the film thickness increases.

2. 3. 3 Aperture coupler

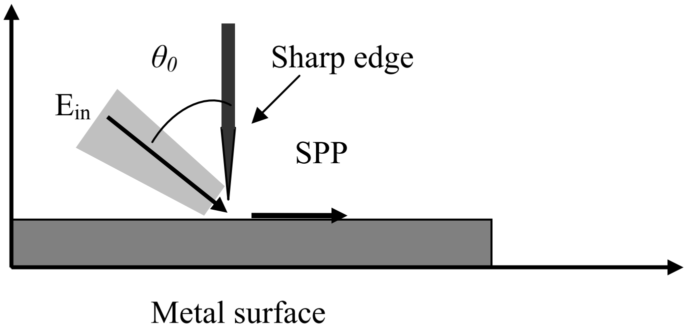

Figure 2-5 Schematic diagram of the aperture coupling method.

In aperture coupling method light incident at an angle θ_0 with the sample normal is focused through a small gap defined by a sharp edge and sample surface [33]. This geometry leads to scattering of the incident radiation and generates evanescent waves consists of continuum of wave vectors. The dispersion relation of part of this wave vectors matches with the SP in the metal surface and hence the excitation of SP is made possible. The surface plasmon is a p-polarized wave so it is necessary condition that the incident electromagnetic radiation should be p-polarized in order to excite SPP. Recently, coupling of THz SPs has been demonstrated [33].

2. 3. 4 Subwavelength metallic hole arrays coupler

Light coupling to the SP through subwavelength hole array on optically thick metal has been demonstrated as an efficient way [1] for the SPPs excitation. This is the method of choice for our experimental method. Subwavelength periodic hole array or corrugation made on the surface of metallic film. The periodic arrays give rise to a two dimensional grating momentum which helps the incident light to be coupled with the surface plasmons. The system has been demonstrated as an efficient way to couple SPPs without any other optical components (for example, lens or prism). The coupling of light to the surface plasmon along with the reverse process, which is conversion of SPP to radiative light, makes this array structure a suitable active photonic component.

Fundamentally, this method is similar as the grating coupling method. If the light with a wave vector $k = \omega/c$ incident on a grating of grating constant a, at an angle θ_0. The component of the incident wave vector on the surface can have wave vector

$$k_x = \frac{\omega}{c}\sqrt{\varepsilon_1}\sin\theta_0 \pm mG_x \pm nG_y = \frac{\omega}{c}\sqrt{\frac{\varepsilon_1\varepsilon_2}{\varepsilon_1+\varepsilon_2}} = k_{sp} \tag{2-9}$$

where m and n are integers, G_x and G_y are the grating momentum. For an hole arrays of square lattice $\left|G_x\right| = \left|G_y\right| = 2\pi/a$. It is possible to couple the SPPs of different resonant wavelengths by the geometrical configuration of the hole arrays.

CHAPTER III

EXPERIMENTAL THz-TDS SETUP

3. 1 Standard THz-TDS system

The THz time-domain spectroscopy setup used in this experiment is a modified version of a typical standard THz-TDS system [37]. A schematic diagram of standard THz-TDS system is given in Ref. 32. Photoconductive switch based [38] transmitter and receiver are used to generate and detect the THz electromagnetic wave. Both transmitter and receiver are coplanar metal transmission lines, photolithographically printed on semi-insulating GaAs and SOS, respectively. A pair of hyper-hemispherical, high resistivity silicon lenses along with a pair of off-axis parabolic mirrors is used to collimate and redirect the transmitted THz pulses towards the receiver. The parabolic mirrors and the silicon lenses are arranged in a confocal geometry to obtain a frequency-independent power transfer efficiency of almost unity. The sample under investigation is placed in the midway between the parabolic mirrors which is essentially the beam waist of the THz radiation.

Configuration of the transmitter chip (F-chip) is shown in Fig.3-1(a), where two 10 μm wide metal lines, photolithographically printed on semi-insulating GaAs substrate, are separated by a distance of 80 μm. Thickness of the metal is about 600 nm (100 nm of Ti + 500 nm of aluminum) and is partially embedded on the substrate material. The receiver chip (Max) configuration is shown in Fig. 3-1(b), where the metal lines of 5 μm wide are separated by 10 μm with an antenna structure of length 10 μm. There is a 5 μm gap at the middle of the receiver antenna. The receiver chip is fabricated on an ion-implanted silicon-on-sapphire (SOS) substrate. Metal was deposited on the chips using an e-beam evaporation system.

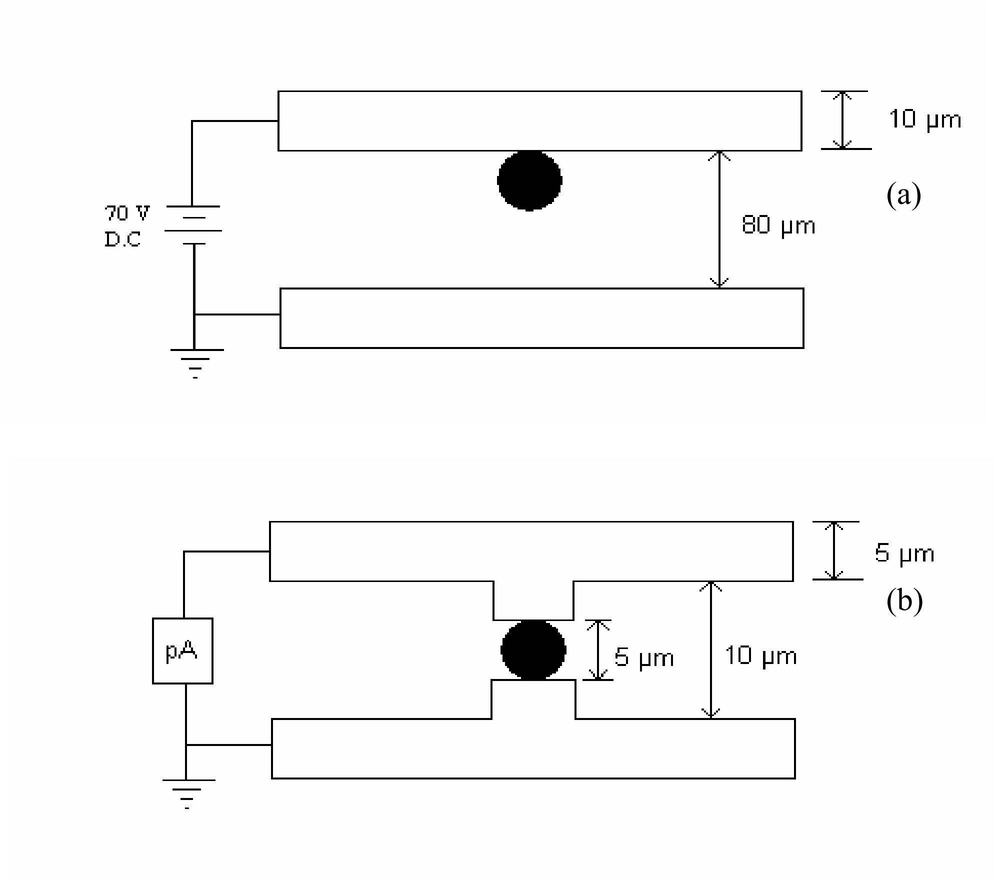

Figure 3-1 (a) THz Transmitter: F-Chip (b) THz Receiver: Max-Chip

A dc bias of 70 V is applied between the transmission lines of the transmitter chip. A self-mode-locked Ti:sapphire laser capable of generating 26-fs, 88-MHz femtosecond pulses having a nominal wavelength of 810 nm is used for generating and detecting THz pulses. The optical pulses are focused on the inner edge of the positive polarity-line of the transmitter as shown in Fig. 3-1(a). Each optical pulse generates electron-hole pairs which are subject to acceleration due to the applied bias fields and the subsequent acceleration of these carriers generates a nearly single-cycle THz electromagnetic radiation. The high-resistive silicon lens attached on the back side of the transmitter collimates the transmitted THz radiation into Gaussian beam with 1/e-amplitude waist of diameter 6 mm. Owing to the confocal geometry, this waist is in the focal plane of the parabolic mirror which focuses the THz beam to another waist (w_2) at mid-point between two parabolic mirrors. Waist w_2 has a frequency-dependent diameter which is proportional to wavelength and at 1 THz is approximately 7 mm [37].

The radiated THz electromagnetic pulses are collimated by another parabolic mirror and are focused to the antenna of the receiver chip with another silicon lens similar to the transmitter side. The receiver antenna, photoconductively switched by another femtosecond optical pulse from the same Ti:Sapphire laser, is sensitive to the polarization of the THz radiation. The receiver is connected to a lock-in amplifier through a low-noise current amplifier. When gated, the receiver generates a dc current which is proportional to the instantaneous electric fields of the received THz electromagnetic wave. By changing the relative time delay between the optical gating pulse and the detected THz pulse the entire pulse shape of the THz radiation can be mapped out as a function of the relative time delay which includes both amplitude and phase information. The generated THz pulses are linearly polarized along the plane perpendicular to the page.

While both transmitter and receiver are driven with an average optical power of 10-mW, the system is capable of generating a subps THz pulses of 4.5 THz usable bandwidth extending from 0.1 to 4.5 THz. For the THz spectroscopy measurements, the transmitted THz pulses are recorded with and without sample in the transmission path to obtain sample and reference signal. The frequency dependent parameters of the sample are obtained by comparing the Fourier transformed spectra of the corresponding time-domain pulses.

3. 2 8-F THz-TDS system

Standard THz-TDS system is modified by introducing an additional pair of parabolic mirrors in the middle of two major parabolic mirrors is shown in Fig. 3-2. The parabolic mirrors are arranged in 8-F confocal geometry which provides excellent beam coupling between the transmitter and receiver. The inner parabolic mirrors M_3 and M_4 are identical with a focal length of 50 mm. The Gaussian beam of THz pulses is focused to a frequency-independent beam waist (W_3) of diameter 3.5 mm [39] at the center between M_3 and M_4 mirrors. The transmitted THz reference pulse and the corresponding frequency spectrum are shown in Fig. 3-3.

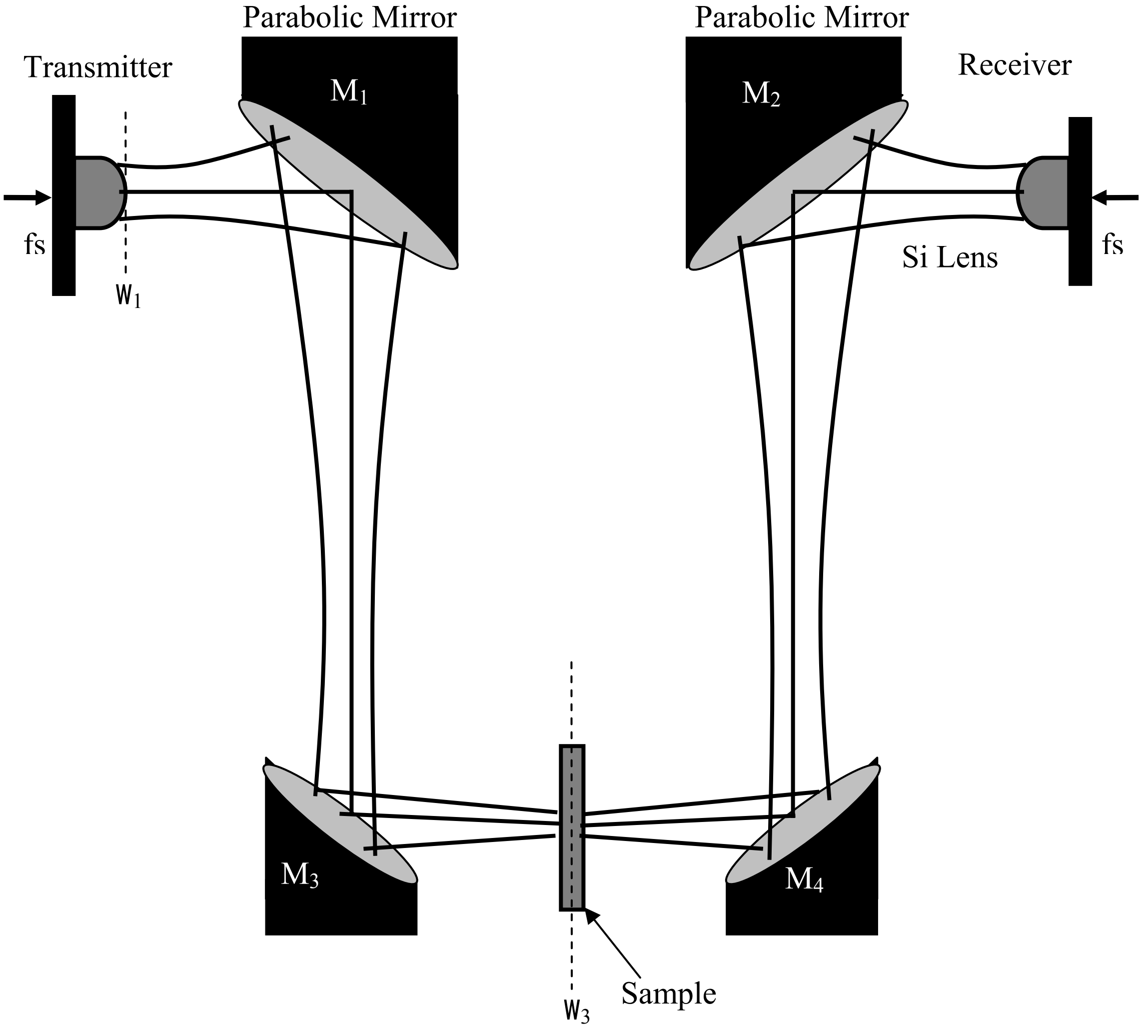

Figure 3-2 Schematic diagram of modified THz-TDS setup with an 8-F confocal geometry. Smallest beam waist is obtained between mirrors M_3 and M_4.

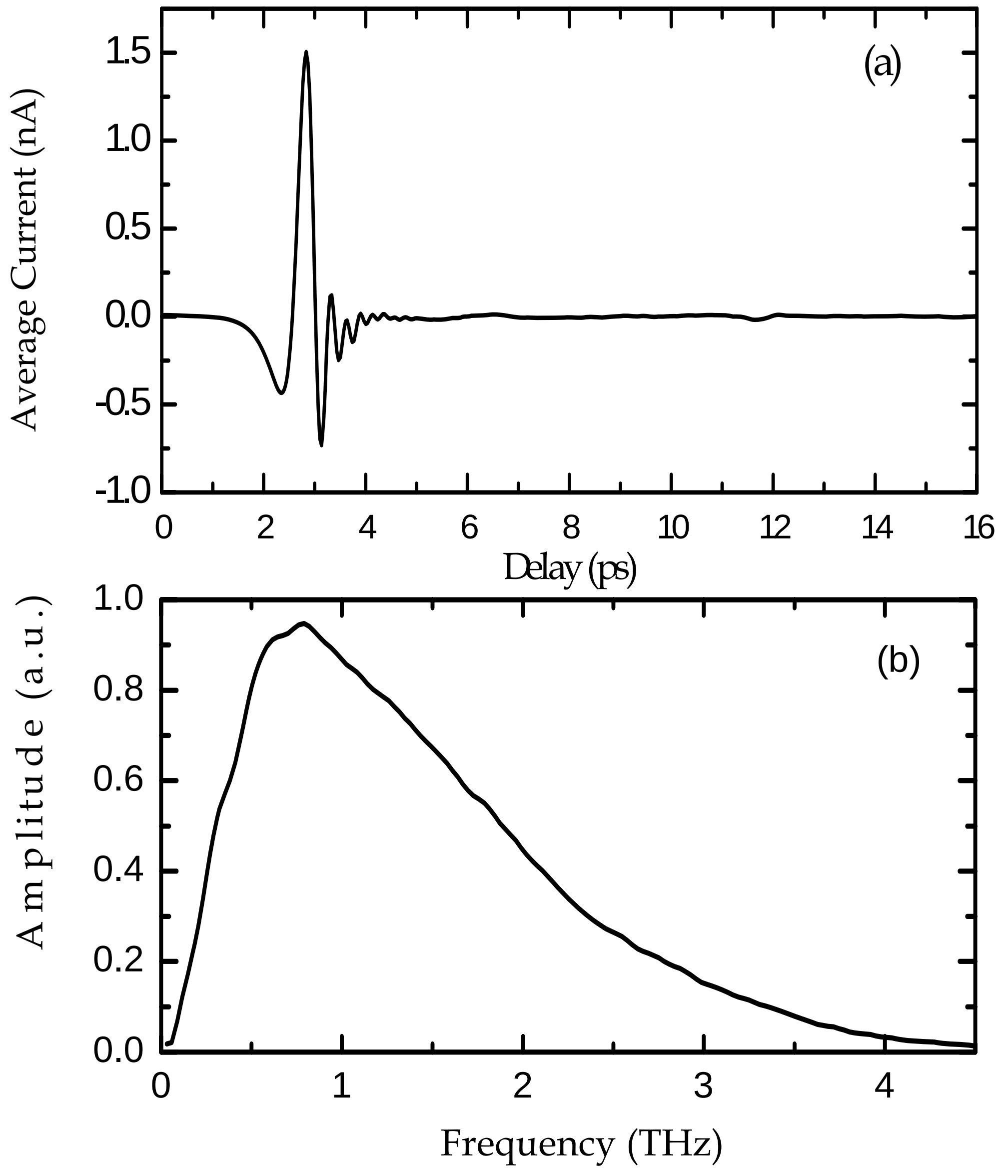

Figure 3-3 (a) Measured THz reference pulse of the system through air, (b) corresponding frequency spectrum of the reference pulse.

With 10 mW of optical input power in both transmitter and receiver, the system is capable of generating THz signal of bandwidth of 4.5 THz. This system is ideal for spectroscopic analysis of the sample with comparatively smaller dimensions. In order to eliminate the effects of the water vapor which absorb some of the frequency components in the THz regime, the entire THz system is enclosed in a box and purged with dry air during data acquisition.

3. 3 THz System stability

In order to perform precise measurement a THz system with high stability is required. In the THz-TDS system two consecutive THz pulses are measured, one through the reference medium and another through the material under investigation (sample). During the time domain data acquisition for both the reference and the sample, the THz pulses should be considerably stable to minimize errors in measurements. To investigate the stability of the system used here, five set of consecutive THz pulses are selected and each set of data contains a reference pulse (through free space) and a sample pulse (through silicon) alternatively. The frequency dependent reference THz pulse of every set of data is compared with that of the next consecutive data set as ratio $E_{ref}^{set3}(\omega) / E_{ref}^{set2}(\omega)$, and so on. The ratios are shown in Fig. 3-4.

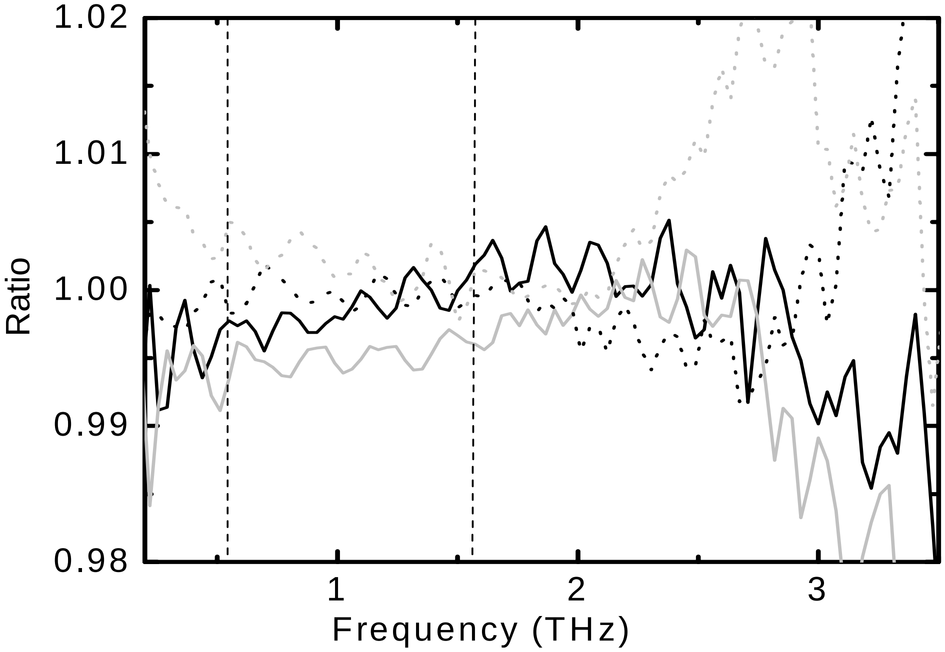

Figure 3-4 Ratios of the consecutive reference pulses: $E_{ref}^{set2}(\omega)/E_{ref}^{set1}(\omega)$ (solid black line), $E_{ref}^{set3}(\omega)/E_{ref}^{set2}(\omega)$ (solid grey line), $E_{ref}^{set3}(\omega)/E_{ref}^{set4}(\omega)$ (dotted black line), and $E_{ref}^{set4}(\omega)/E_{ref}^{set5}(\omega)$ (dotted grey line).

The vertical dashed lines show the position of the frequencies where the surface plasmon resonances are observed. Within the frequencies of interest THz system shows errors about ±0.5 %.

CHAPTER IV

EXTRAODINARY THz TRANSMISSION OF DOPED SILICON HOLE ARRAYS

In 1998, Ebbesen *et al.* [1] discovered extraordinary enhanced optical transmission through subwavelength hole arrays perforated on an optically thick metallic surface. Electromagnetic radiation by a subwavelength hole was an active research field for a long time. The established theory for the transmission of electromagnetic radiation predicts that the transmitted intensity decreases with the hole diameter as $(d/\lambda)^4$ [40], where d is the diameter of the hole and λ is the wavelength of the electromagnetic radiation. The transmitted intensity of Ebbesen's experiment is higher than unity when normalized to the area occupied by the holes. This extraordinary transmission is successfully explained in terms of resonant excitation of surface plasmon polaritons (SPPs) on metal-dielectric interfaces. The incident light resonantly couples to the SPPs which tunnel through the subwavelength holes and reradiate as light on the opposite side. The resonance frequency can be controlled by the period of the hole array, shape and size of the hole, dielectric properties of the metals and the surrounding dielectrics. To form and support the SPPs a metal-dielectric interface is preconditioned where the metal is described by the negative value of the real part of dielectric constant.

4. 1 Dielectric properties of doped silicon

In the THz frequency region, it has been demonstrated that highly doped semiconductors show metallic behavior because the real part of the dielectric properties posses negative value. For this experimental work, a highly doped n-type silicon wafer is chosen to be a metal like material. The silicon is chosen for not only the non toxicity but also carrier dynamics of doped silicon has been well studied [41]. The dielectric function of the doped silicon can be expressed by the Debye model as

$$\varepsilon(\omega) = \varepsilon_r(\omega) + i\varepsilon_i(\omega) = \varepsilon_{si} + \frac{i\sigma(\omega)}{\omega\varepsilon_0} \tag{4.1}$$

where ε_{si} dielectric contribution of silicon, ε_r and ε_i are the real and imaginary part of the dielectric constants, ω is the angular frequency, ε_0 is free space dielectric, and $\sigma(\omega)$ is the complex conductivity. The complex conductivity of the doped silicon can be well expressed by the simple Drude models as

$$\sigma(\omega) = \sigma_r(\omega) + i\sigma_i(\omega) = \frac{i\varepsilon_0\omega_p^2}{\omega + i\Gamma} \tag{4.2}$$

where σ_r and σ_i are the real and imaginary conductivity; Γ is the carrier damping rate; and ω_p is the plasma frequency. The plasma frequency ω_p is defined as $\omega_p = \sqrt{Ne^2/\varepsilon_0 m^*}$; where N is the carrier density, e is the charge of the electron, ε_0 is free space dielectric, and m^* is the effective mass of the electron. The effective electron mass of silicon is $0.26m_0$, where m_0 is the mass of free electron. The real and imaginary parts of the complex conductivity are given by,

$$\sigma_r(\omega) = \frac{\varepsilon_0 \omega_p^2 \Gamma}{\omega^2 + \Gamma^2}$$
$$\sigma_i(\omega) = \frac{\varepsilon_0 \omega_p^2 \omega}{\omega^2 + \Gamma^2} \tag{4.3}$$

The real and imaginary parts of the complex dielectric constants are given by,

$$\varepsilon_r(\omega) = \varepsilon_{si} + \frac{\omega_p^2}{\omega^2 + \Gamma^2}$$
$$\varepsilon_i = -\frac{\omega_p^2 \Gamma}{\omega(\omega^2 + \Gamma^2)} \tag{4.4}$$

Using equation 4.4, it is possible to calculate the carrier concentration dependent real and imaginary dielectric constant of the doped silicon for any fixed frequency.

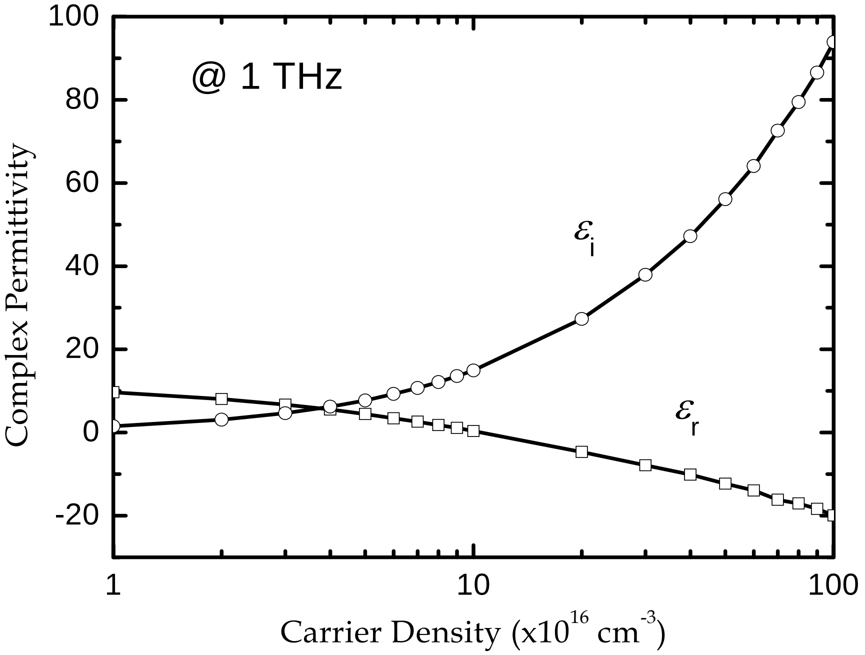

Figure 4-1 Complex permittivity, real (open square) and imaginary (open circle), of n-type doped silicon at 1 THz as a function of carrier density.

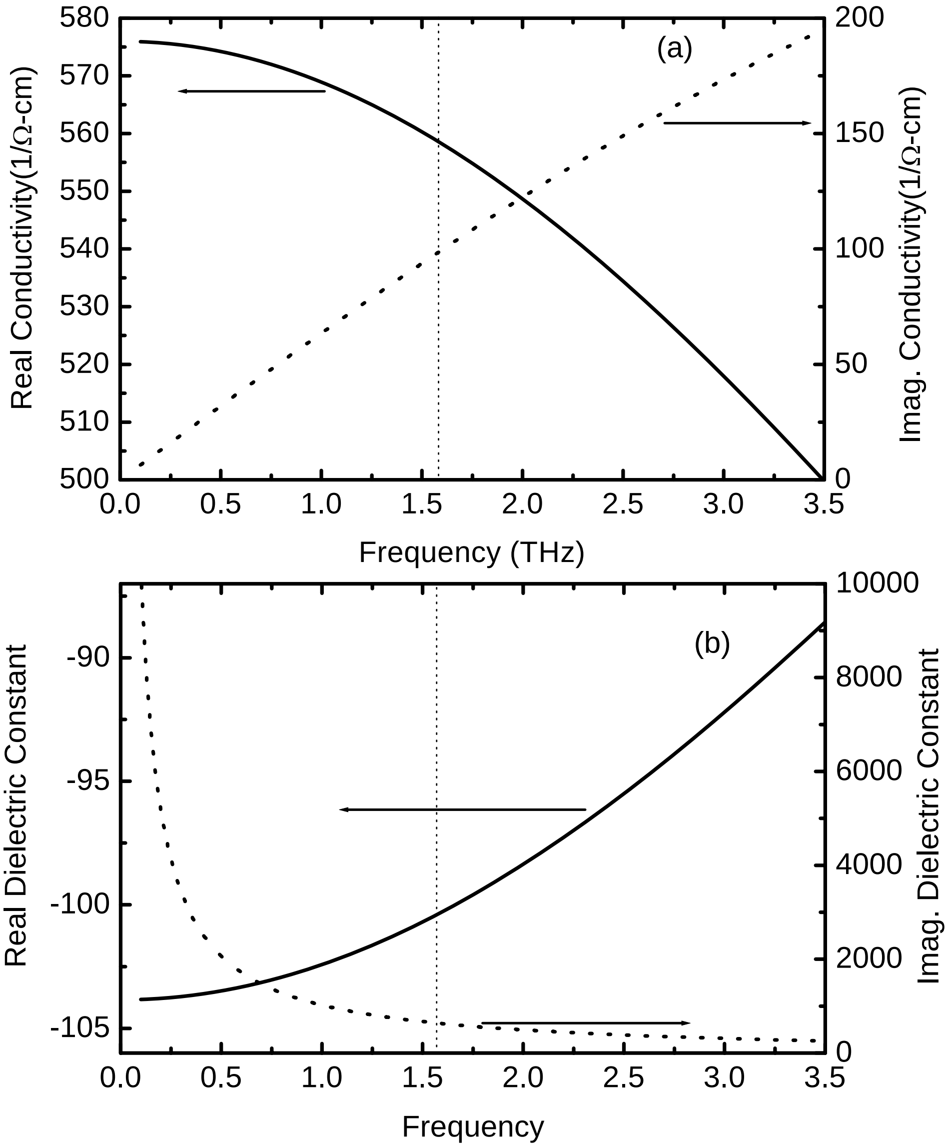

Figure 4-2 (a) Frequency-dependent real (solid line) and imaginary (dotted line) conductivity of doped silicon with carrier density of $3\times10^{19}\,\mathrm{cm}^{-3}$. (b) Corresponding complex dielectric constant: real part (solid line) and imaginary part (dotted line). The vertical dashed line shows the resonance position of SPPs.

Eqs (4.3) and (4.4) imply that by varying the doping concentration it is possible to tune up the dielectric properties of doped silicon. Of course, the plasma frequency ω_p and Γ will be the function of the doping concentration.

Fig. 4-1 shows that the metallic behavior of n-doped silicon, which is defined by the negative value of ε_r, can be realized at 1 THz when $N > 1\times10^{17}$ cm^{-3}. The sample used in this experiment was processed from a commercially available n-type, 50-µm-thick silicon wafer with a resistivity of $2\times10^{-3}\,\Omega-\text{cm}$ and a corresponding high carrier concentration of $3\times10^{19}\,\text{cm}^{-3}$. The calculated frequency-dependent conductivity σ_r and σ_i, and the corresponding dielectric properties ε_r and ε_i are shown in Figs. 4-2(a) and 4-2(b) which are calculated using Drude model. The real part of conductivity and dielectric constant are represented by solid line. The imaginary part of the conductivity and dielectric constant are represented by dashed line. To calculate the real and imaginary dielectric constant the estimated mobility is 120 cm^2/Vs from Ref. 41. The vertical dashed line represents the frequency of the fundamental surface plasmon resonance mode. Fig. 4-2 (b) illustrates that in the range of our frequency of interest the real dielectric constant has negative values which confirms the metallic behavior of this highly doped silicon.

4. 2 Sample Preparation

The carrier density and the thickness of the doped silicon are chosen to ensure that no THz transmission is observed through the unstructured silicon slab. In this experiment, the corresponding amplitude absorption length is less than 1 μm at 1 THz. The fabrication processes of the subwavelength hole arrays have included the conventional photolithography and RIE. The wafer was spin-coated with SU-8 2015 photoresist (Microchem) and exposed with a UV light source while under the mask. The wafer was coated with photoresist in two spinning cycles. The first cycle was spread cycle: applied photoresist and removed all bubbles carefully, then ramped to 500 rpm at 100 rpm/second acceleration. This will take 5 second. On the next cycle, the wafer was ramped to 2000 rpm at 300 rpm/second acceleration and hold for 30 second. The approximate thickness of the photoresist was 21 μm. The wafer was soft baked using hot plate at 65˚ C for 1 min pre-bake followed by 3 min of soft-bake at 95˚ C. A light field mask of rectangular hole arrays of dimension $100\times80\ \mu m^2$ arranged in a square arrays with a lattice constant of 160 μm was used for contact mode expose. The total exposer time was set 90 second. The post expose bake included hot plate 1 min at 65˚ C followed by 3 min at 95˚ C. The sample was developed using immersion methods in a full concentration RD6 developer. After development the RIE process has created through-holes on the bare silicon while the other part of the wafer was still protected by the photoresist. A mix gas flow of 12.5 sccm of SF_6 and 1.5 sccm of O_2 gas driven under a RF power of 400 W gave an etching rate of 5 μm/min. The front side of the wafer (the side covered with photoresist) has a rectangular hole shape which was deformed with the etching depth. At the front surface the hole shape has a dimension of 120×95 μm^2 and the side wall is not vertical shown in Fig. 4-3 (b). The side wall makes an approximate angle of 23˚. The holes on the back side have elliptical shape shown in Fig. 4-3 (a). However, the shape of the front surface, the subwavelength hole size still be determined by the smaller aperture of the back side. This was inspected by illuminating the sample with THz radiation from both sides and we had not noticed any distinguishable difference in the transmissions. Figure 4-3 shows the SEM picture of the hole array with a periodicity of 160 μm and the THz input side has elliptical holes of dimensions of 75 μm along the major axis (*y*) and 45 μm along the minor axis (*x*).

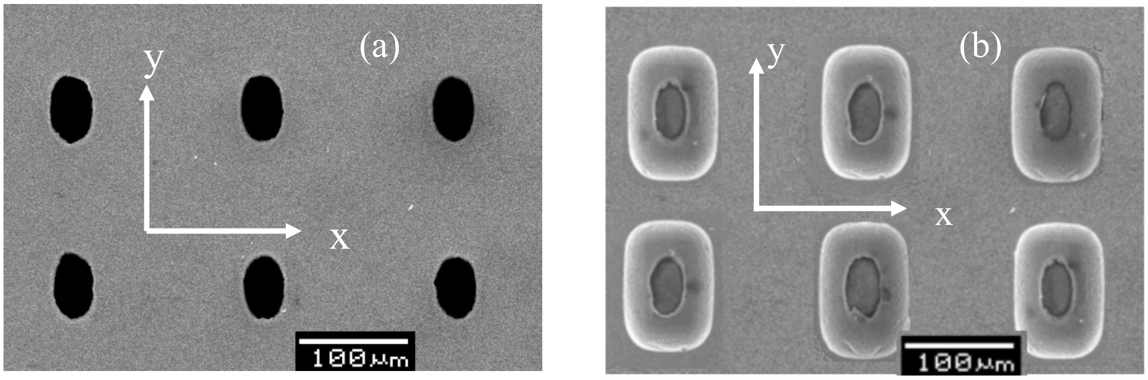

Figure 4-3 SEM image of the subwavelength, hole arrays fabricated on a highly doped, n-type, 50-μm-thick silicon wafer, with a period of 160 μm: (a) THz input side and (b) THz output side. Elliptical hole shape of input side determines the aperture which has dimensions of 75 μm along the major axis and 45 μm along the minor axis.

4. 3 Data acquisition

The transmission measurement is carried out using a focused beam terahertz time domain spectroscopy (THz-TDS) system is shown in chapter III. Driven with 10-mW fs pulses on both THz transmission and detection chips, the set-up generates up to 4.5 THz broadband electrical pulses. Sample and reference electrical fields are recorded in the time domain with and without sample in the THz transmission path and the frequency dependent transmission information is derived from the ratio of the corresponding spectra. The sample is attached to a mechanical holder and centered over a hole of 5 mm diameter. Another identical clear hole is used as the reference. The transmission measurements are performed with a linearly polarized THz beam impinging on the sample at normal incident. The diameter of THz beam at the waist of the focused beam is measured 3.5 mm which is small compared to diameters of reference and sample holes. Sample pulses are recorded for two different orientations. Generated THz pulse is linearly polarized parallel to the plane of optical table. Sample pulses are taken by placing the minor axis of the elliptical holes along the polarization of electric field (E||x) and then rotate by 90° and place the major axis of holes along polarization (E||y).

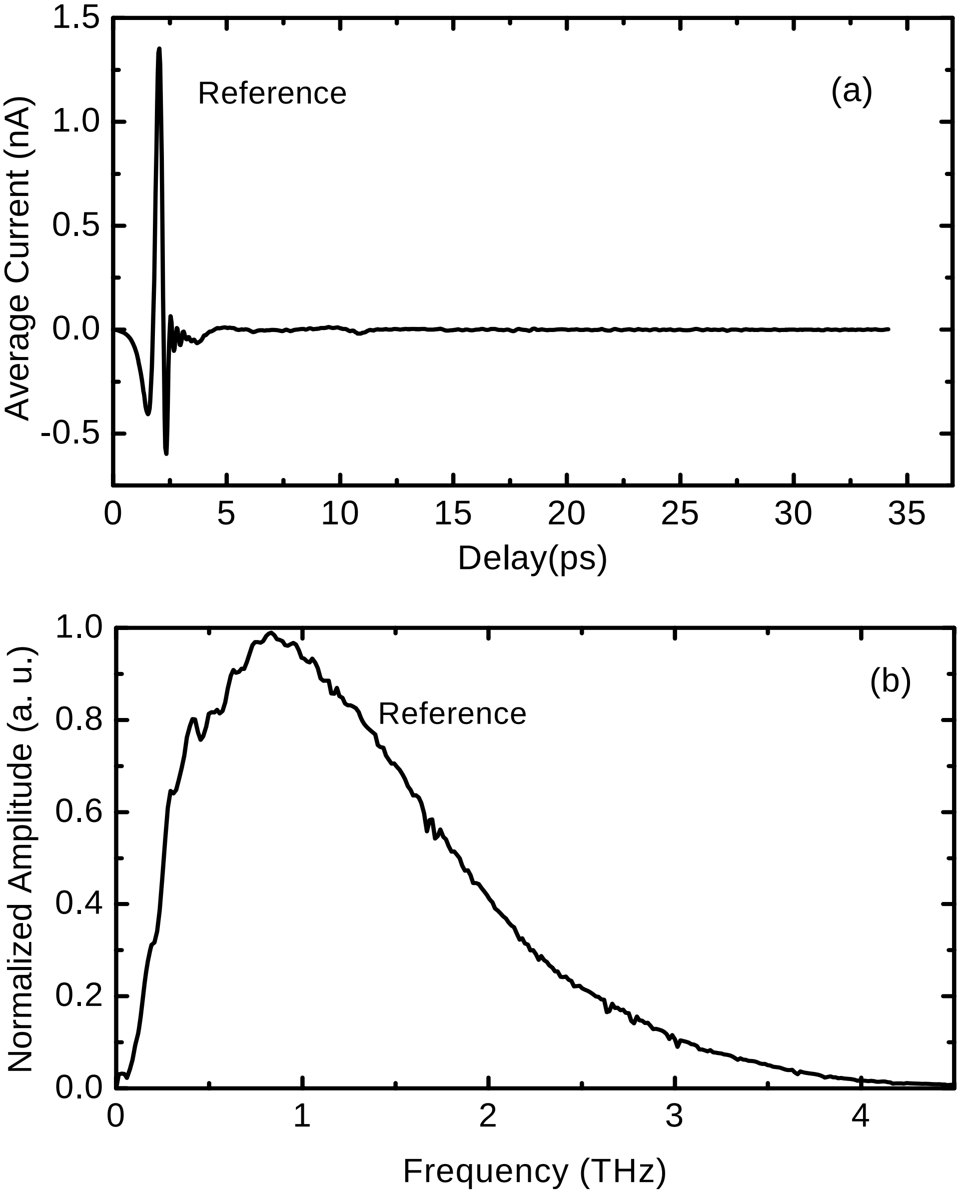

Figure 4-4 (a) Measured THz reference pulse through the clear aperture, (b) Corresponding frequency spectrum of THz pulse.

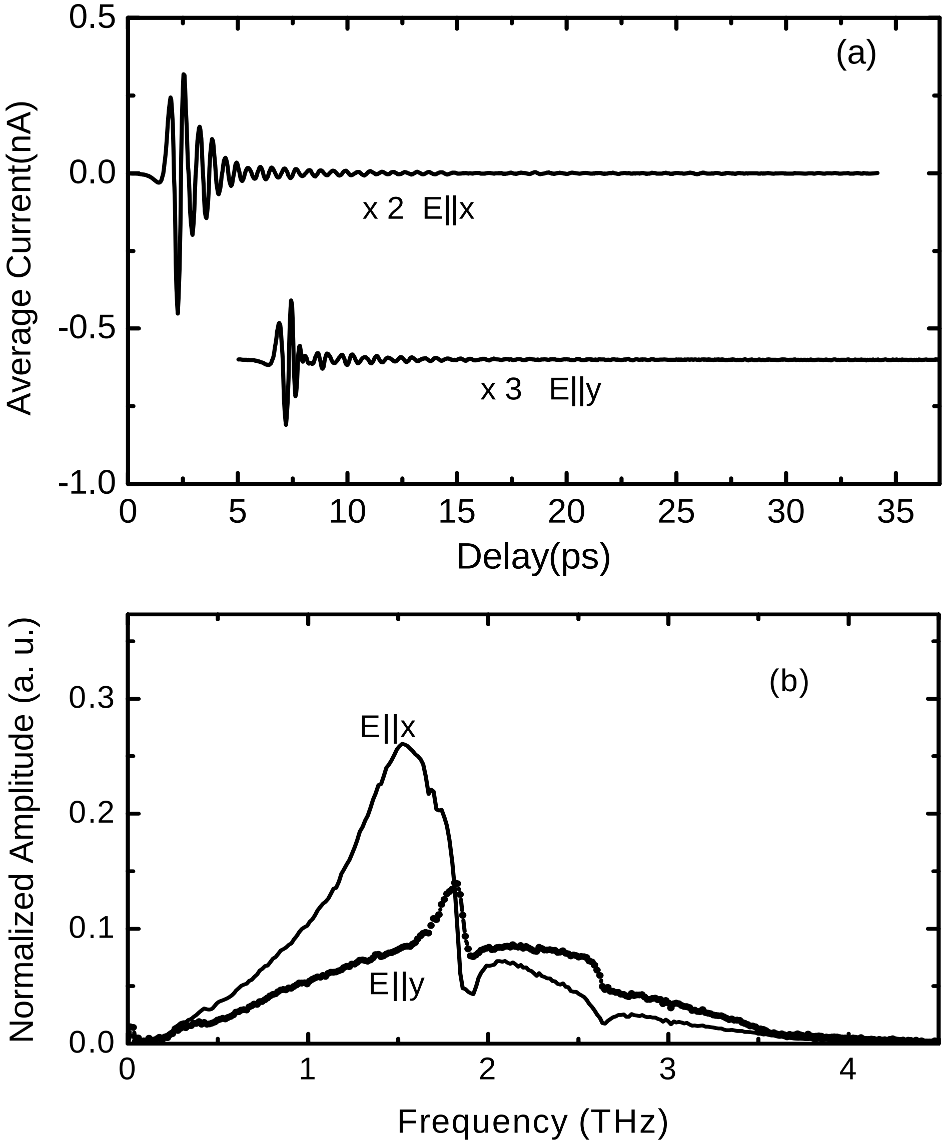

Figure 4-5 (a) Measured THz pulses through sample for two orthogonal orientations: E||x (upper) and E||y (lower). For clarity lower curve displaced vertically by -0.6 nA and horizontally by 5 ps. (b) Corresponding Fourier-transformed spectra.

4. 4 Theory of resonant tunneling of SPPs of hole arrays

SPPs are excited when their momentum matches the momentum of the incident photon and the grating as follows:

$$k_{sp} = k_x \pm mG_x \pm nG_y \qquad (4\text{-}5)$$

where k_{sp} is the surface plasmon wavevector; $k_x = (2\pi / \lambda)\sin\theta$ is the component of the incident photon's wavevector in the plane of the grating; G_x and G_y are the grating momentum wavevectors; and m and n are integers. For square-lattice hole arrays the grating momentum wavevectors are $G_x = G_y = 2\pi / L$, where L is lattice constant of arrays. In order to make a comparison of the experimental data, a surface plasma dispersion relation appropriate for a smooth metal-dielectric surface is considered. Presence of the hole arrays may cause a significant change in the dispersion relation but for the first approximation this change has been neglected. The dispersion relation of surface plasmons for a smooth metal-dielectric interface is

$$k_{sp} = \frac{\omega}{c}\sqrt{\frac{\varepsilon_1 \varepsilon_2}{\varepsilon_1 + \varepsilon_2}} \qquad (4\text{-}6)$$

where $\omega = 2\pi c / \lambda_{sp}$ is the angular frequency of SPs; c is the speed of light in vacuum; ε_1 is the dielectric constant of the of the surrounding material; $\varepsilon_2 = \varepsilon_{r2} + i\varepsilon_{i2}$ is the dielectric constant of the metal like grating materials, for which ε_{r2} and ε_{i2} are the real and imaginary part, respectively.

For normal incident, the resonant wavelengths for the excitation of SPPs of a square lattice structure are obtained by comparing Eq. (4-5) and Eq. (4-6) as

$$\lambda_{sp}^{m,n} \cong \frac{L}{\sqrt{m^2+n^2}}\sqrt{\frac{\varepsilon_1\varepsilon_2}{\varepsilon_1+\varepsilon_2}}, \tag{4-7}$$

In optical region most of the metal has negative ε_{r2} and the ratio between the real and imaginary part of the dielectric constant, $-\varepsilon_{r2}/\varepsilon_{i2} >> 1$. It has been experimentally demonstrated that SPPs assisted transmission increases with the higher value of $-\varepsilon_{r2}/\varepsilon_{i2}$ [42]. However, Moreno *et al.* [14] have demonstrated that appropriate periodic corrugation of the surface changes the effective dielectric constant which facilities the establishment of SPPs. As a result the enhanced transmission can be realized even with smaller ratio of $-\varepsilon_{r2}/\varepsilon_{i2}$. Based on the simple Drude theory the calculated real and imaginary dielectric constant at 1 THz are $\varepsilon_{r2} = -103$, and $\varepsilon_{i2} = 1020$, respectively, giving a ratio of $-\varepsilon_{r2}/\varepsilon_{i2} = 0.1$.

4. 5 Dependence of peak transmission on sample orientation

To determine the orientation-dependent enhanced transmission, the sample was first oriented in a way that the terahertz polarization is perpendicular to the major axis of the elliptical hole ($E||x$), then it was rotated by 90°, enabling the polarization of THz beam parallel to the major axis of the hole ($E||y$). The frequency dependent transmission amplitude spectra defined by the ratio of the sample and reference spectra for both orientations are shown in Fig. 4-6. For the case of $E||x$, the transmission spectrum shows a pronounced peak at 1.6 THz, well below the cutoff frequency, 2.0 THz determined by the 75-μm-sized holes. The peak of the transmission amplitude is due to the resonance of SPPs and can be attributed to the [±1, 0] surface plasmon mode as indicated by a dashed line in Fig. 4-6 (a).

We observe 42% relative amplitude transmission for the [±1, 0] mode at the silicon-air interface. Corresponding power transmission is shown in Fig. 4-6 (b) which shows 18% relative power transmission. To find the area normalized transmission, the relative transmission is multiplied by the fraction of the area occupied by the holes only. The area of ellipse is determined as $\pi(x \times y)/4$, where x and y is the length of the minor and major axes respectively. The area occupied by the holes is 10.35% of entire sample area. This leads to a normalized power transmission efficiency of 175%.

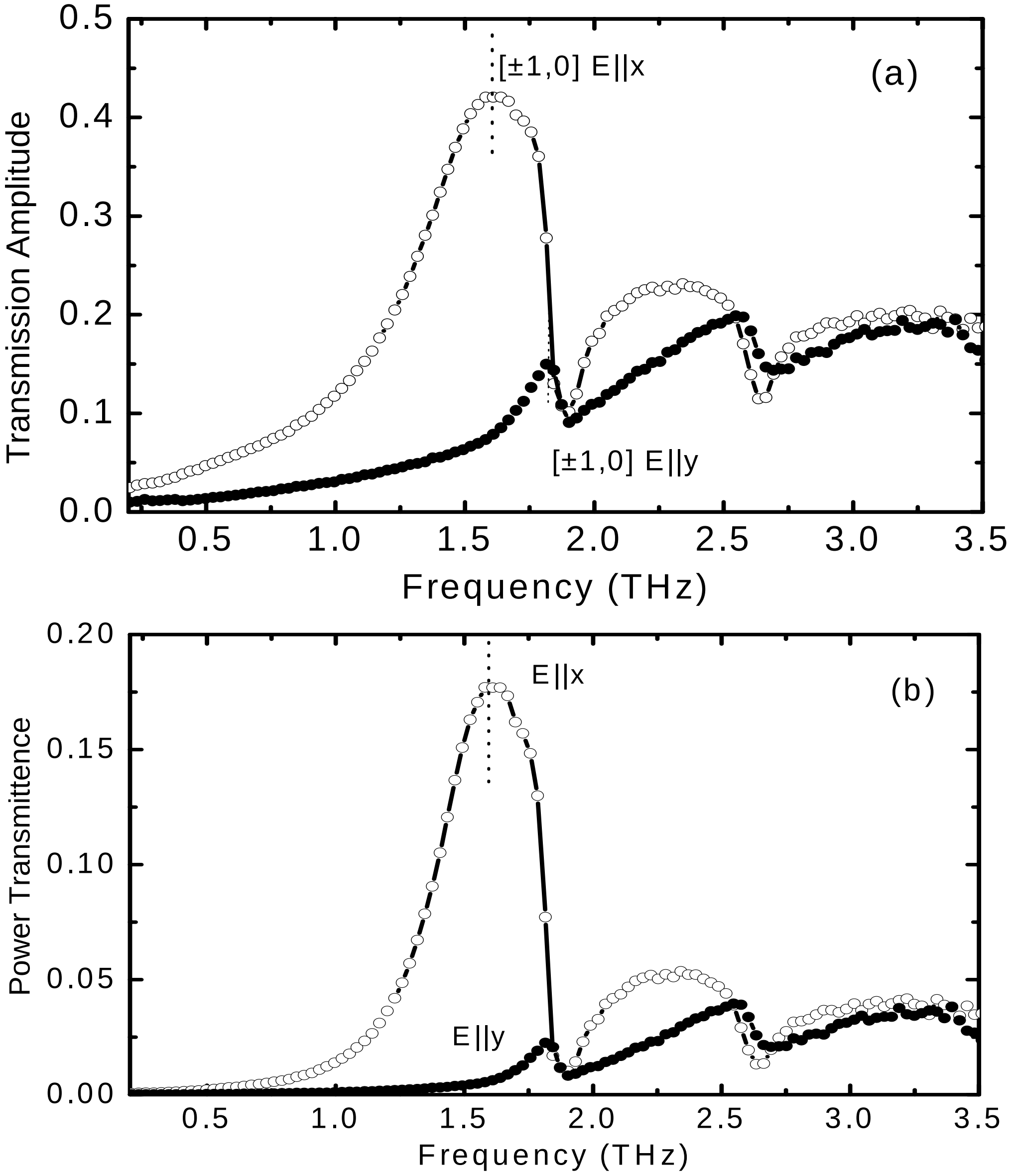

Figure 4-6 Frequency dependent transmission spectra of THz pulses though silicon array: (a) amplitude transmission and (b) Power transmission. Transmissions are measured for two orthogonal orientations: major axis of elliptical holes perpendicular to THz polarization (open circles) and major axis parallel to the polarization of THz beam (dots). The dashed line represents [±1, 0] resonance peaks.

In the $E||y$ orientation the resonance peak is located at 1.8 THz and has found an actual field transmission efficiency of 140% and corresponding power transmission efficiency 25% when normalized the hole area with the lattice area. We assign this peak to SP [±1, 0] mode as shown in Fig. 4-6. The effect of the hole structure on THz transmission has been demonstrated in Ref. 17, where a higher transmission magnitude was observed for a rectangular hole array than that of a circular holes with the same fundamental period. This difference in the amplitude transmissions in two different orientations is because of the preservation of the input linear polarization for the surface mode. When the major axis is perpendicular to the polarization of THz beam ($E||x$) it preserves the input linear polarization for the surface plasmon more than that of $E||y$ orientation. Recently, polarization dependent optical transmission through elliptical nanohole array through metal film is demonstrated [44]. The experimental result shows that the transmission is maximum when the polarization of the optical beam is perpendicular to the major axis of elliptical holes, which agrees with our results.

The prominent minima are observed for both orientations at frequency 1.87 THz, which can be identified as the result of Wood's anomaly observed in diffraction grating structures [45]. Wood's anomaly minima occurs when a diffracted order becomes tangent to the plane of grating. For a square lattice and normal incidence the wavelengths of Wood's anomaly minima are approximately given by [6]

$$\lambda_{\text{Wood}}^{m,n} = \frac{L}{\sqrt{m^2 + n^2}}\sqrt{\varepsilon_1}. \tag{4-8}$$

When the surrounding dielectric constant $\varepsilon_1 << \varepsilon_2$, the resonant wavelength for SPPs given in Eq. (4-7) differs very slightly from the wavelength of Wood's anomaly minima, in fact, they might partially overlap. Observed minima in the transmission spectra are well described by Eq. (4-8).

Measured transmission resonances appear at lower frequency than that expected by the Eq.(4-7). Discrepancy of the measured resonant frequency with the theoretical value can be described by the following reasons: Eq.(4-7) is an oversimplified approximation for thin metal film using surface plasmon dispersion appropriate for a smooth film and ignoring the fact that the holes in the film may cause both a significant change in plasmon dispersion and large coupling between the front and back surface of the metal film. The sample is made of highly doped silicon with periodic holes on it, which might need more pragmatic theory. The resonance transmission peaks might overlap with the Wood's anomaly minima, which can truncate the SPPs resonance amplitude and push the peak towards the lower frequency. Another reason of the discrepancy might arise from RIE assisted undercutting. To check the reproducibility of the measurements, the sample was flipped over and illuminated with THz pulses from the back. Transmission measurements were performed for both orientations and no perceptible differences either in the peak position and transmission amplitude has been observed.

4. 6 Dependence of the transmission peak on surrounding dielectrics interface

The dependence of the SPP-assisted transmission properties on the dielectric constant of the surrounding materials were investigated by measuring the zero order transmission through sandwiches made of the array and the desired materials. Four different interfaces were characterized including air-array-air, low-density poly-ethylene (LDPE)-array-LDPE, quartz-array-quartz, and silicon-array-silicon. The quartz slides used here are made from fused silica and the surrounding silicon is moderately doped n-type with a resistivity of 20 Ω cm. These surrounding materials are fairly transparent to the THz frequencies and have different refractive indices of 1, 1.51, 1.98 and 3.42, respectively, for Air, LDPE, quartz and silicon. The same subwavelength-structured sample was used as the array and the resonance peaks in the transmission spectra were confirmed by placing the major axis of the hole perpendicular to the THz polarization ($E||x$). The amplitude transmission spectra for different interfaces are shown in Fig. 4-7, where the [±1, 0] modes are represented by the dashed lines. The experimental result shows that the peak amplitude decreases when the surrounding material has a higher index and the corresponding resonance peak moves toward the lower frequency as predicted by Eq. (4-7). This result is also consistent with the experimental observation in the optical region.

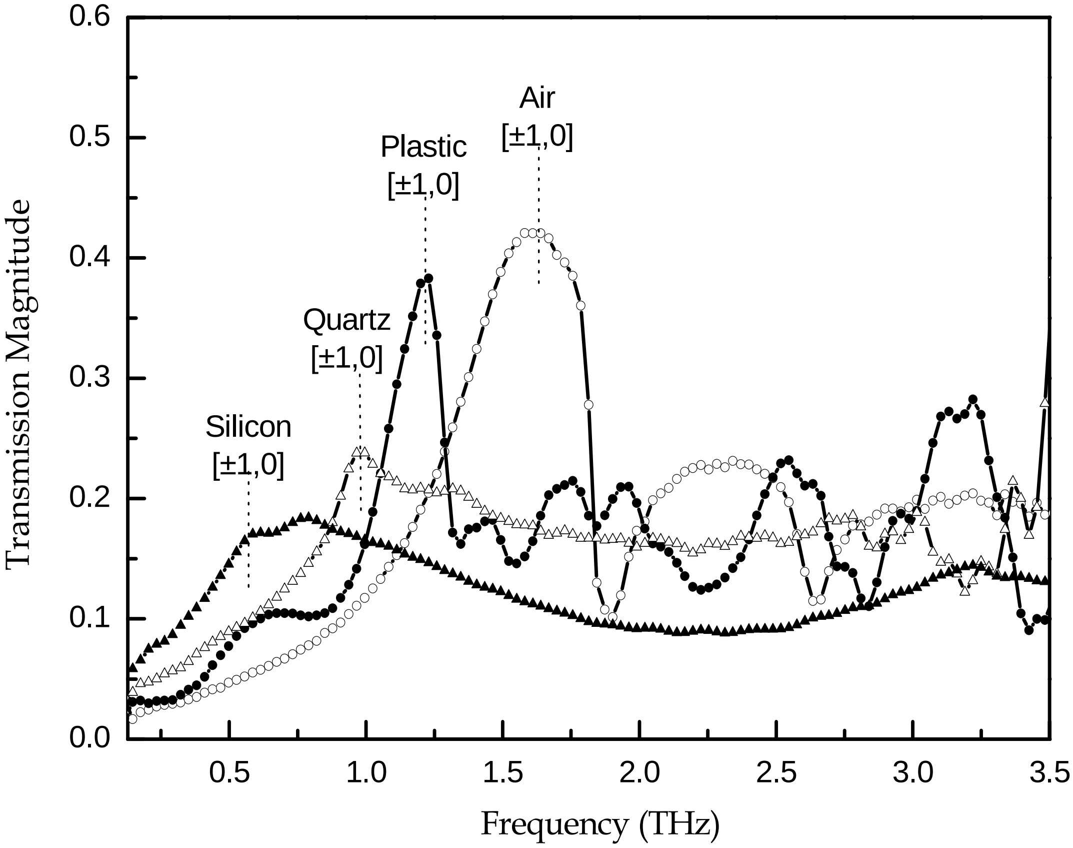

Figure 4-7 Comparison of transmission spectra for different dielectric-grating interfaces: air-grating-air (open circles), plastic-grating-plastic (dots), quartz-grating-quartz (open triangles) and silicon-grating-silicon (solid triangles). Dotted lines represent [±1, 0] resonance peaks.

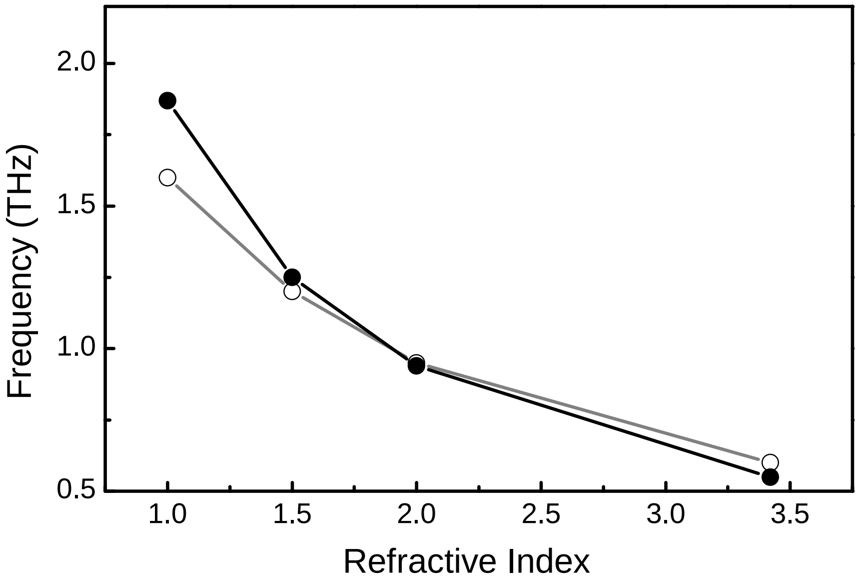

Figure 4-8 Comparison of SPPs [±1, 0] resonance frequency with respect to surrounding dielectric index of refraction: Measured (open circle) and calculated from Eq.4-4 (solid circle).

The low-index material clearly shows pronounced maxima and minima due to the resonant excitation of SPPs and Wood's anomaly, respectively. For high-index material, however, the pronounced maxima are relatively broader because of the merging of consecutive resonance peaks. Wood's anomaly effect is also appeared to be weaker due to the overlapping of the resultant peaks. The resonance peak position can be resolved by increasing the periodicity of the corrugation. Residual air in between the array and the surrounding material also might contribute to distort the transmission peaks which can be solved by using the liquid as a surrounding dielectric medium. This feature enables tuning the resonant frequency of SPPs dynamically by varying the index of refraction of the surrounding dielectric materials. The observed and the calculated resonance frequencies of the [±1, 0] mode as a function of the surrounding refractive index is plotted in Fig. 4-8.

Extraordinary transmission is observed below the cutoff frequency, is attributed to the tunneling through the excitation of the resonant SPPs. Transmission spectra show pronounced minima described by Wood's anomaly. We also investigate the dependence of the sample orientation on transmission efficiency, which shows that the maximum efficiency is obtained when the incident terahertz polarization is perpendicular to the major axis of the hole-structure. Furthermore, the effect of the surrounding dielectric is observed, which shows the possibility of use the same grating as a frequency selective SPPs assisted optoelectronic device in the THz frequency range.

CHAPTER V

EFFECT OF DIELECTRIC PROPERTIES OF METALS ON THz SPPs

5. 1 Metal's dielectric effect on optical SPP

This chapter demonstrates the effect of dielectric properties of metals on surface plasmons enhanced THz transmission through subwavelength hole arrays patterned on optically thick metallic films made from different metals. The effect of the metals' dielectric function on SPP-enhanced transmission has been investigated in the optical frequency region. Measured transmissions of light through the identical hole arrays made from different metals showed significant difference in the transmission peak and line shape. The complex dielectric function of metals, $\varepsilon_m = \varepsilon_{rm} + i\varepsilon_{im}$ has played an important role in supporting the SPP-assisted extraordinary optical transmission. For a good conducting metal the real part of dielectric constant ε_{rm} is negative, which is the essential condition for the formation of SPPs. Experimental results on the enhanced transmission through subwavelength metallic structures reveal that the optimal metals in the optical frequency regime are characterized by the higher value of the ratio between the real and imaginary dielectric constant, $-\varepsilon_{rm}/\varepsilon_{im}$. It was demonstrated that the transmission efficiency increases with higher ratio $-\varepsilon_{rm}/\varepsilon_{im}$ at optical frequencies where for most metals the ratio $-\varepsilon_{rm}/\varepsilon_{im} >> 1$ [7]. Owing to the difference in the ratio $-\varepsilon_{rm}/\varepsilon_{im}$, the transmission properties of light had a dramatic change in the arrays made of silver (Ag), gold (Au), and chromium (Cr) [1].

In the low frequency region, for example, at THz and microwave frequencies, the dielectric constant of metals is very high and for the non-transition metals, such as Ag, Au, Al, the imaginary dielectric constant ε_{im} is orders of magnitude higher than the absolute value of the real dielectric constant $|-\varepsilon_{rm}|$ [46]. This gives a ratio $-\varepsilon_{rm}/\varepsilon_{im} < 1$, which was believed to be a limitation to realize the enhanced transmission at low frequencies. However, SPP-enhanced transmissions have been observed experimentally in both the THz and microwave frequency regions because the periodic corrugation changes the effective dielectric functions and favors SPPs excitation.

Dielectric function of metals plays crucial role in the optical transmission. So, it is intriguing how the metal dielectric plays role in enhanced THz transmission. For this demonstration, hole arrays of identical dimensions are fabricated on different metals and the corresponding THz transmissions through these arrays are compared. Extraordinary THz transmissions are observed and attributed to the resonance excitation of THz SPPs. Peak resonances are investigated for [±1, 0] plasmon modes at 0.55 THz and 1.60 THz for metal-silicon and metal-air interfaces, respectively.

5. 2 Sample fabrication

Two different types of metallic subwavelength hole arrays samples have been prepared: (a) metal-array-on-silicon (MAOS), which has a structured metal film on a blank silicon substrate to investigate the metal-silicon [±1, 0] resonance mode; and (b) freestanding-metal-array (FMA) of metallic films to investigate the metal-air [±1, 0] resonance mode. The fabrication process of these samples includes conventional photolithography and metallization techniques. The MAOS samples were fabricated on a 0.64-mm-thick P-type silicon wafer with a resistivity of $\rho = 20\ \Omega$ cm. The wafer was first spin-coated with photoresist-adhesive promoter HMDS at 3000 rpm for 30 seconds. Then a positive photoresist S-1813 (Shipley) was applied and spun at 3000 rpm for another 30 seconds. At this speed the thickness of the photoresist layer was approximately 1.5 μm. The wafer was then exposed with a contact mode mask aligner using UV light (λ = 436 nm) while under the mask. For metallization three different metals were chosen, those are Ag, aluminum (Al), and lead (Pb). Metal thicknesses for the metallization were carefully chosen to be equal to the skin depth at particular resonance frequency (skin depth is discussed in chapter 6). A 120-nm-thick metal layer was chosen for Ag, and Al array and a 330-nm-thick metal layer was chosen for Pb sample. Metal films were then thermally evaporated on the patterned photoresist using a thermal evaporator (BOC Edward 306) at vacuum pressure of 2.5×10^{-5} mB and a deposition rate of ~3 nm. After the lift-off a pattern of 100 μm × 80 μm rectangular hole array arranged in square lattice with periodicity of 160 μm can be obtained on silicon substrate. A high resolution optical image of the Ag MAOS is shown in Fig. 5-1 (a).

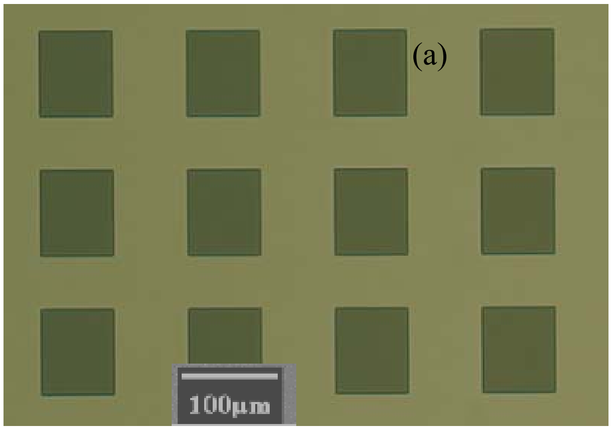

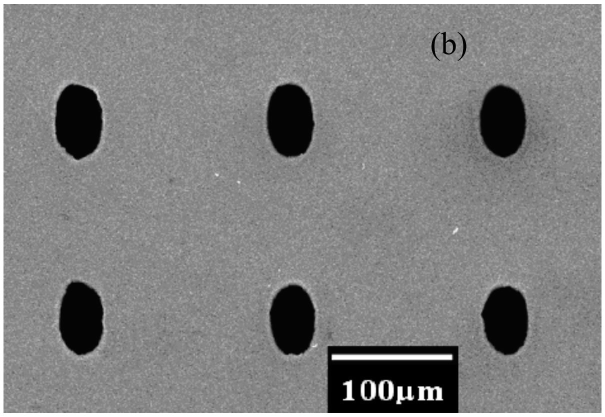

Figure 5-1 (a) High resolution optical image of Metal-Array-on-silicon sample. The hole has a physical dimension of 100 μm × 80 μm and periodicity of 160 μm. (b) SEM image of 'freestanding' metallic arrays. The elliptical hole has dimensions of 75 μm along the major axis and 45 μm along the minor axis with a periodicity of 160 μm.

The FMA array is prepared by depositing metal films on both surfaces of a 50-µm-thick silicon core array with pre-existing elliptical through holes patterned by reactive ion etching (RIE). The silicon core has a resistivity of $2\times10^{-3}\Omega$ and a corresponding amplitude absorption length less than 1 µm at 1 THz. The fabrication process of the silicon core is described in chapter 4 and the elliptical hole has dimensions of 45 µm along the minor axis and 75 µm along the major axis. The periodicity of the array sample is 160 µm. Such a structured core is considered as a freestanding-metal-array when metallized both surfaces of the core array with desired metal with a film-thickness equivalent to the skin depth of the metal. The film thickness was chosen 180 nm for all metals. A thermal evaporator was used for the metallization at a working vacuum pressure of 2.5×10^{-5} mB and a deposition rate of ~2nm/second. The SEM image of such a freestanding array made from Ag is shown in Fig. 5-1 (b).

For FMA-array preparation same core structure has been metallized with different metals. Before metallization of any metals the previous existing metal films were carefully removed using wet etching methods. Wet etching process of Ag and Al is essentially similar. The sample with metals was dipped in the solution made of 1:2 ratios of HCl and DI water at a temperature 80º C. To remove metals completely the process takes approximately 10 minutes. The sample is then washed with DI water and blown to dry with N_2 gas.

5. 3 Dielectric properties of metals

The effect of the dielectric properties of metals on the enhanced THz transmission was investigated on arrays made of various non-transition metals including Ag, Al, and Pb. The dielectric function of these metals can be well described by Drude model

$$\varepsilon_m(\omega) = \varepsilon_\infty - \frac{\omega_p^2}{\omega^2 + i\omega\omega_\tau} \qquad \text{(5-1)}$$

Separating the real and imaginary parts yields

$$\varepsilon_{rm} = \varepsilon_\infty - \frac{\omega_p^2}{\omega^2 + \omega_\Gamma^2},$$

$$\varepsilon_{im} = \frac{\omega_p^2 \omega_\Gamma}{\omega(\omega^2 + \omega_\Gamma^2)}$$

where ω_p is the plasma frequency, ω_τ is the carrier damping frequency, and ε_∞ is the high frequency dielectric constant. The complex conductivity of the metal is related to the dielectric constant as

$$\varepsilon_m(\omega) = \varepsilon_{rm} + i\varepsilon_{im} = \varepsilon_\infty + \frac{i\sigma_m(\omega)}{\varepsilon_0 \omega}$$

where, $\sigma_m(\omega)$ is the complex conductivity related to the real and imaginary conductivity $\sigma_{mr}(\omega)$ and $\sigma_{mi}(\omega)$ as $\sigma_m(\omega) = \sigma_{mr}(\omega) + i\sigma_{mi}(\omega)$. Separating the real and imaginary parts yield

$$\sigma_{mr}(\omega) = \varepsilon_0 \omega \varepsilon_{mi}(\omega)$$

$$\sigma_{mi}(\omega) = \varepsilon_0 \omega (1 - \varepsilon_{mr}(\omega))$$

For a non-transition metal high frequency dielectric contribution of metals ε_∞ was considered 1 in Ref. 46. The measured values of dielectric constants from various experiments are theoretically fitted to obtain the values of ω_p and ω_Γ in Ref. 46. It was demonstrated that the dielectric constants could be described by the Drude fitting. The Drude parameters obtained from the theoretical fitting of the experimental data are tabulated in Table 5-1 for the metals of our interest. These Drude parameters are used to reproduce the frequency dependent dielectric constants in the THz frequency. The corresponding conductivities are also calculated from the dielectric constants.

Metal	$\omega_p/2\pi$ (THz)	$\omega_\tau/2\pi$ (THz)
Ag	2197	4.39
Al	3606	19.6
Pb	1879	4.39

Table 5-1 Experimentally determined parameters of Drude fittings for metals given in Ref. 46

Figure 5-2 shows the Drude fitting of the frequency-dependent complex dielectric function of Ag, Al, and Pb at THz frequencies. The vertical dashed lines indicate the corresponding values at the observed [±1, 0] resonance frequencies for metal-silicon mode at 0.55 THz and for metal-air mode at 1.60 THz. The dielectric constant of Ag, Al, and Pb are represented by solid line, dotted line, and dash-dotted line, respectively. Clearly, the absolute values of both the real and imaginary dielectric constants are of few orders of magnitude higher than optical frequencies. The frequency dependent conductivities of the metal are shown in Fig. 5-3. In the low frequency region, the real part of the conductivity is an order of magnitude higher than the imaginary conductivity.

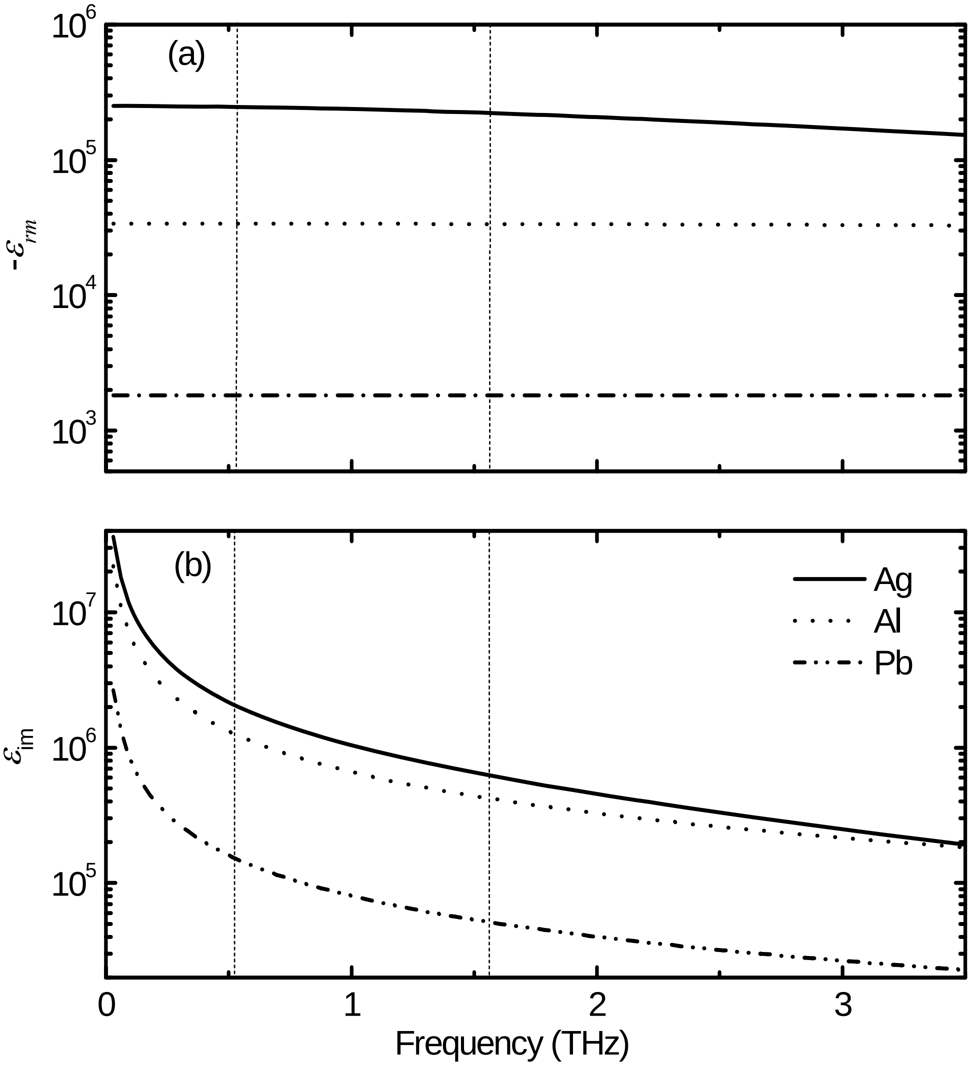

Figure 5-2 Calculated dielectric constant of Ag (solid lines), Al (dotted lines), and Pb (dash-dotted lines) using Drude model; (a) Real dielectric constant, $-\varepsilon_{rm}$; (b) imaginary dielectric constant, ε_{im}. Vertical dashed lines indicate the two fundamental [±1, 0] resonance modes of metal-silicon and metal-air interfaces.

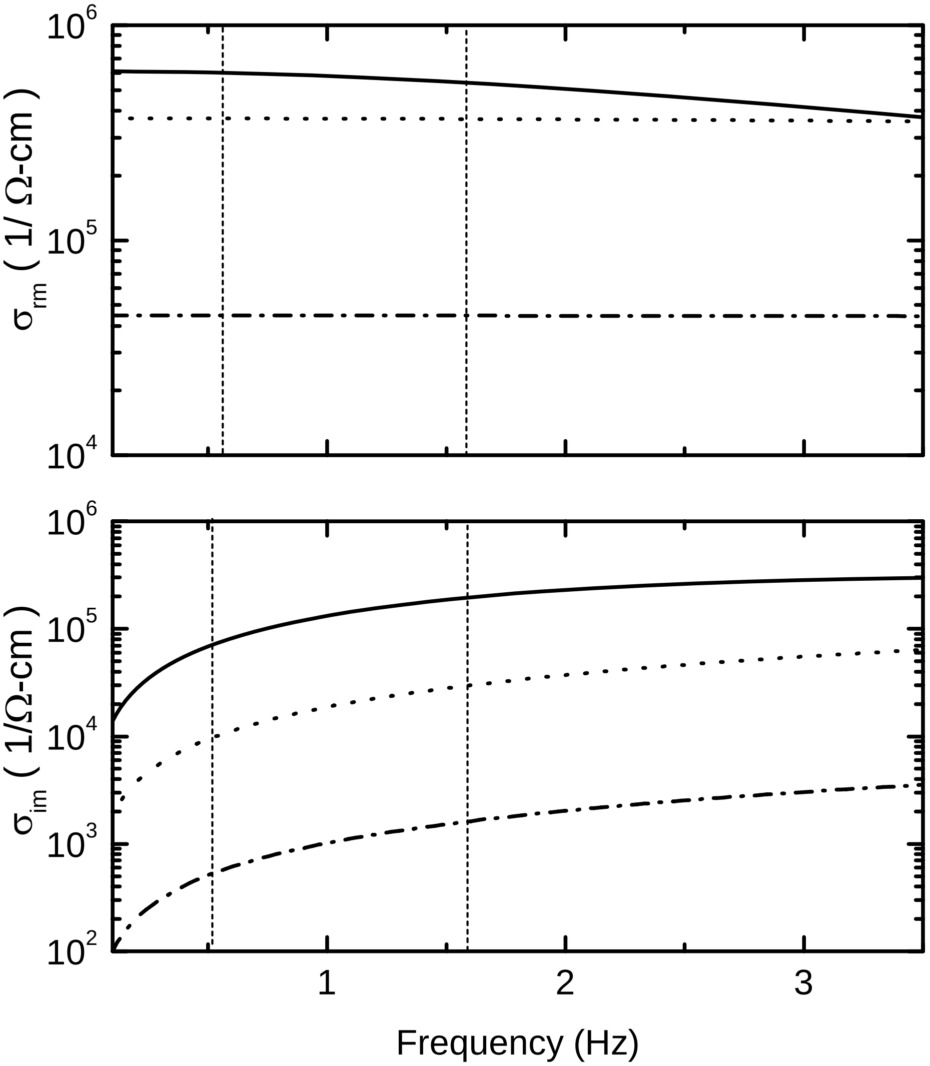

Figure 5-3 Calculated **c**onductivity of Ag (solid lines), Al (dotted lines), and Pb (dash-dotted lines) using Drude model. (a) real dielectric constant, $-\sigma_{rm}$; (b) imaginary dielectric constant, σ_{im}. Vertical dashed lines indicate the two fundamental [±1, 0] resonance modes of metal-silicon and metal-air interfaces.

5. 4 Experiments

To examine the enhanced transmission at the [±1, 0] metal-silicon SPP resonance mode, the metal-array-on-silicon was placed in a way that the polarization of the THz electric field is parallel to the minor axis of the rectangular holes to maximize the zero-order field transmission. The time extent of the THz pulse scans is limited by the strong reflection from the back side of the silicon wafer, which consequently limits the frequency resolution of the numerical Fourier transform of the time-domain pulses. To extrapolate the frequency-dependent transmission with better resolution, the measured time-domain THz pulses were extended four times longer by adding zeros at the end of the these pulses.

A blank silicon wafer, identical to the sample-substrate, is attached next to the sample to obtain the reference THz pulses. Measured THz pulses transmitted through the reference silicon and metal-array-on-silicon and their corresponding frequency spectra are shown in Fig. 5-4. The metal-array-on-silicon for this set of data is made from Ag film. Fig. 5-4 (a) shows the comparison of the THz pulses transmitted through reference and sample. For clarity the sample pulse is displaced both vertically and horizontally. The vertical displacement is -0.4 nA and the horizontal displacement is +1.5 ps. The sample pulses of other arrays made from different metals show similar behaviors. Fig. 5-4 (b) shows the frequency dependent spectra of the corresponding THz pulses. The sample spectrum shows a resonance behavior which is different from the reference spectrum.

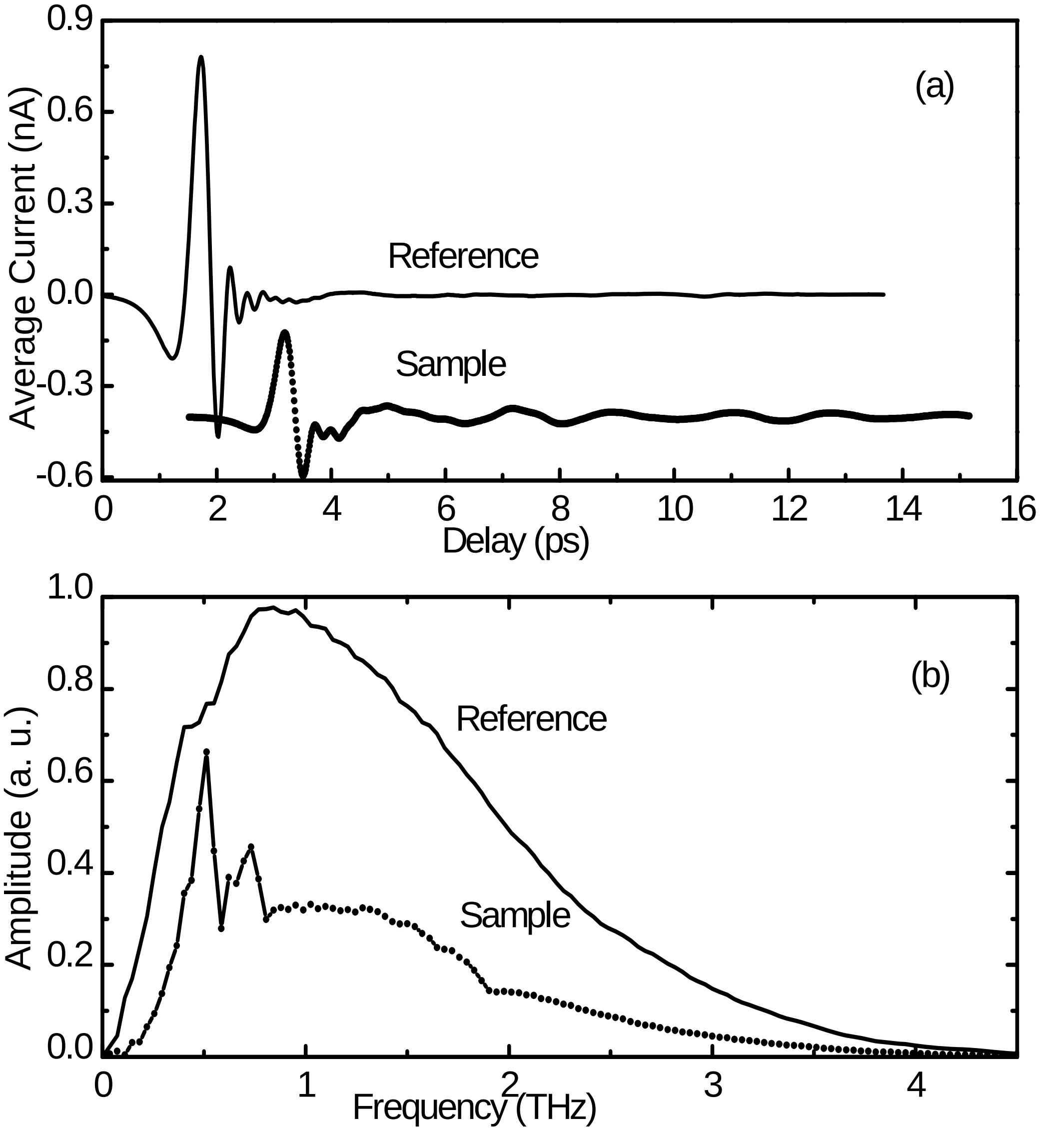

Figure 5-4 (a) Comparison of reference and sample THz pulses. Sample pulse is displaced for clarity by -0.4 nA in the current axis and +1.5 ps in the time axis. (b) Comparison of the corresponding frequency dependent amplitude spectra of the transmitted THz pulses.

The sample THz pulse consists of main THz pulse followed by ringing fields which are the effect of the resonance excitation of the SPPs. The spectrum of the sample shows the presence of resonance structure. The two pronounce peak in the sample spectrum is the signature of the lower order SPP resonance modes.

5. 5 Resonance frequency of SPPs in metals

As derived in Chapter IV, for normal incidence the resonance wavelength of the surface plasmon polaritons in the metal-dielectric interface can be written as,

$$\lambda_{sp}^{m,n} \cong \frac{L}{\sqrt{m^2 + n^2}} \sqrt{\frac{\varepsilon_1 \varepsilon_m}{\varepsilon_1 + \varepsilon_m}},$$

In the THz frequency region, the dielectric constant of highly conducting metals is of few orders higher than the surrounding dielectrics, i.e. $\varepsilon_m >> \varepsilon_1$, where ε_1 is the dielectric constant of the surrounding material. At normal incidence, the resonant wavelengths for the excitation of the THz SPPs of a square lattice structure are approximately given by

$$\lambda_{sp}^{m,n} \cong L\sqrt{\varepsilon_1} \Big/ \sqrt{m^2 + n^2}\ , \tag{5-2}$$

where L is the lattice constant; m and n are the integer mode indices. Based on this relation the calculated first three [m, n] resonance modes are located at 0.548 [±1, 0] and 0.775 [±1, ±1] THz, for the metal-silicon interface; and at 1.875 [±1, 0] THz for the metal-air interface, where we used the value of ε_1=11.70 for silicon and ε_1=1 for air. The vertical dashed line shown in Fig. 5-2 indicates the calculated [±1, 0] metal-silicon resonance. To compare the transmission enhancement as a function of the ratio $-\varepsilon_{rm}/\varepsilon_{im}$, dielectric properties of metals obtained from Fig. 5-2 and Ref. 46, and their ratios are tabulated in Table 5-2 for three resonance frequencies at 0.55 THz, 1.60 THz and 375 THz (optical frequency).

Metal	λ=545μm (0.54 THz)			λ=187μm (1.60 THz)			λ=0.8μm (375 THz)		
	$-\varepsilon_{rm}$ (10^4)	ε_{im} (10^4)	$-\frac{\varepsilon_{rm}}{\varepsilon_{im}}$	$-\varepsilon_{rm}$ (10^4)	ε_{im} (10^4)	$-\frac{\varepsilon_{rm}}{\varepsilon_{im}}$	$-\varepsilon_{rm}$	ε_{im}	$-\frac{\varepsilon_{rm}}{\varepsilon_{im}}$
Ag	24.6	214	0.115	22.1	61.0	0.36	29	1	29
Al	3.38	130	0.026	3.36	41.4	0.08	45	28	1.6
Pb	0.18	16	0.011	0.18	5.0	0.036	14.5	12.3	1.17

Table 5-2 Calculated real and imaginary dielectric constants and their ratios using Drude model of metals. Three different resonance frequencies are compared.

5. 6 Results of metal-arrays-on-silicon

The frequency dependent amplitude and power transmission of the measured spectra can be written as,

$$T_{amplitude}(\omega) = \left| \frac{E_{sample}(\omega)}{E_{reference}(\omega)} \right|$$
$$T_{Power}(\omega) = \left| \frac{E_{sample}(\omega)}{E_{reference}(\omega)} \right|^2 \tag{5-3}$$

where $E_{reference}(\omega)$ and $E_{sample}(\omega)$ are the frequency dependent spectrum of reference and the sample pulses. Fig. 5-5 illustrates the transmission amplitude through the metal-arrays-on-silicon made from Ag, Al, and Pb, respectively. For clarity, the transmission curves are vertically displaced. The experimental data exhibit well defined maxima and minima, which are attributed to the resonant excitation of SPPs and Wood's anomaly, respectively. Amplitude transmission spectra show very high transmission at frequency 0.5 THz. An immediate minimum appeared in the spectrum after the maxima. To understand the contribution of the metal dielectric only the first fundamental SPP resonance mode will be discussed here.

Fig. 5-6 illustrates the corresponding transmittance, or power transmission through the different metal-arrays-on-silicon. For clarity the [±1, 0] metal-silicon SPP resonance mode is shown in an expanded view. The transmittance of Ag, Al, and Pb are represented by solid line, dotted line, and dash-dotted line, respectively.

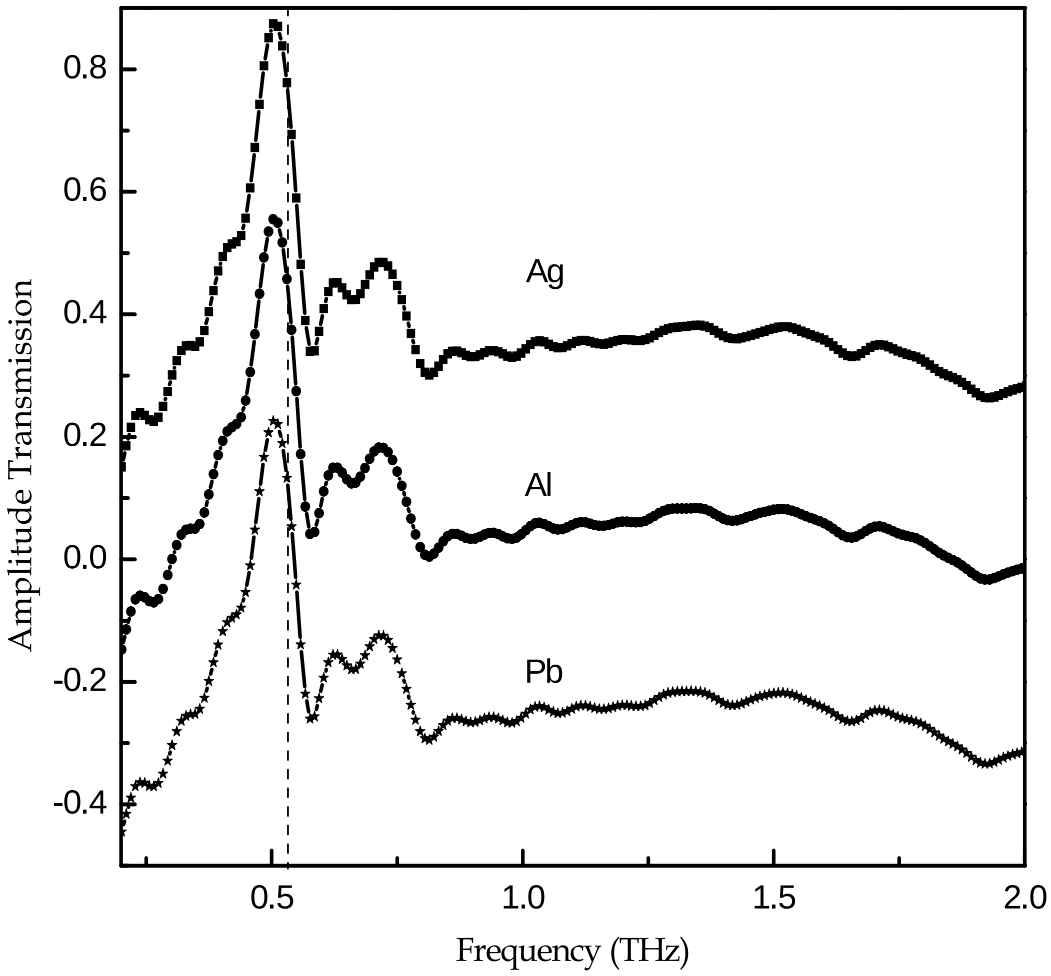

Figure 5-5 Measured amplitude transmission through the array-on-silicon samples made of Ag (squares), Al (circles), and Pb (stars), respectively. For clarity, the spectra of Al, and Pb are moved down by 0.3 and 0.6, respectively. The vertical dashed line indicates the calculated surface plasmon [±1, 0] metal-silicon resonance mode.

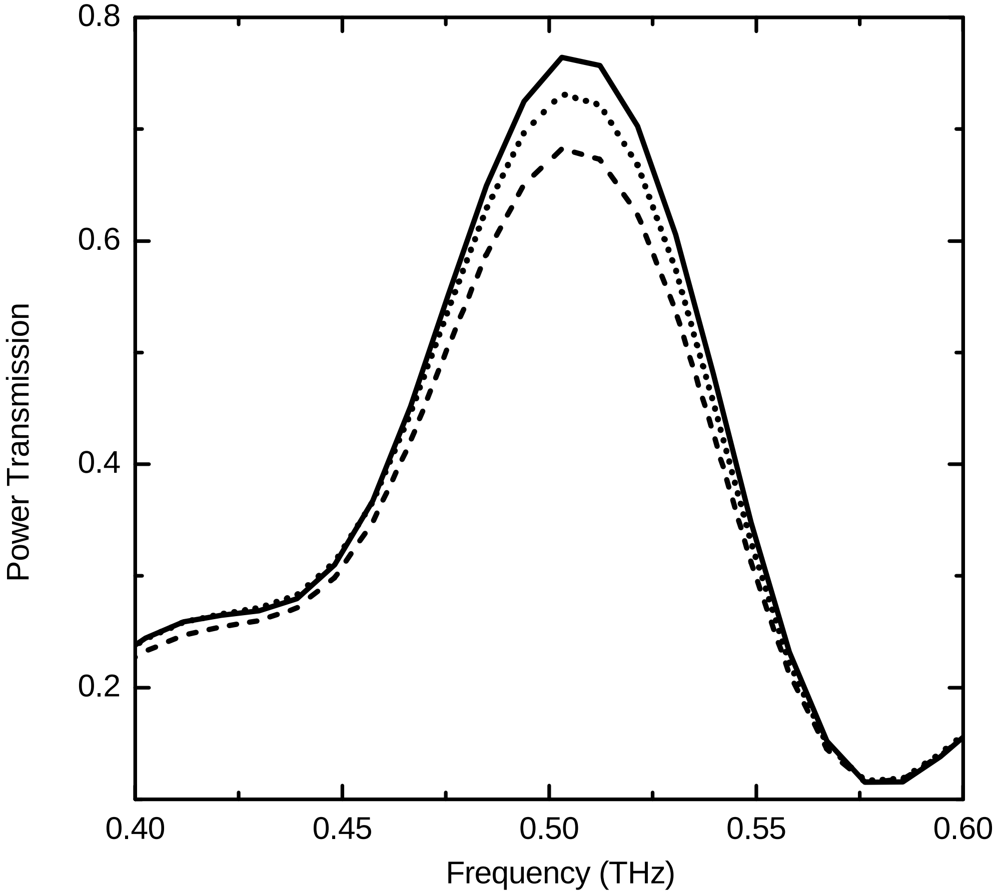

Figure 5-6 Measured transmittance of metal-silicon [±1, 0] resonance mode through the metal-array-on-silicon samples made of Ag (solid line), Al (dotted line), and Pb (dashed line).

It has been experimentally demonstrated that electromagnetic wave having wavelength more than double of the hole size can not propagate through such an array when the array thickness is very high compared to the skin depth. Transmission through such an array below the cutoff frequency decays exponentially with the array thickness. For the array-on-silicon, the cutoff frequency, defined by the length of longer side of the rectangular holes (100 μm), is about 1.5 THz. Measured amplitude transmission shows very high resonance peak at 0.5 THz much below the cutoff frequency defined by the hole size. This high transmission is attributed to the resonance excitation of SPPs at metal-silicon interface.

The measured resonance for the [±1, 0] metal-silicon SPP mode is observed at slightly lower frequency than the calculation. Among these samples, the Ag array shows the highest amplitude transmission of 87±0.4%, Al arrays shows 85.5±0.4%. Besides these good conducting metals, good amplitude transmission also observed through Pb which is generally considered as a poor electrical conductor. Surprisingly, enhanced THz transmission through array-on-silicon made from Pb has shown an amplitude efficiency of up to 82±0.5%. The resonance line width, on the other hand, exhibits no obvious change between these arrays. At optical frequencies, however, the transmission properties of subwavelength arrays made of Ag and Au have shown notable difference in both the resonance amplitude and line width [1]. Measured transmittance of the [±1, 0] metal-silicon SPP mode for Ag, Al, and Pb metal-array-on-silicon are 76.5±0.3%, 73±0.3%, and 68.2±0.5%.

Ag and Al are known as the excellent electrical conductors with dielectric constants of ε_{Ag}= -29.7 + 1.0*i* and ε_{Al}= -45.7 + 28.1*i*, respectively, at optical frequencies (λ = 800 nm), and ε_{Ag} = -2.46×10^5 + 2.14×10^6*i* and ε_{Al} = -3.4×10^4 + 1.30×10^6*i*, respectively, in the THz region (λ = 545 μm). The dielectric constant of Pb is ε_{Pb} = -14.5 + 12.3*i* at λ = 800 nm and ε_{Pb} = -2.0 ×10^3 + 1.6×10^6*i* at 0.55 THz. The dramatic increase of the dielectric constant enables Pb to behave as a better conductor towards the establishment of SPP-enhanced transmission at THz frequencies. At 0.55 THz, the ratio $-\varepsilon_{rm}/\varepsilon_{im}$ for Ag, Al, and Pb are 0.12, 0.03, and 0.01, respectively. In the THz frequencies the complex conductivities of Ag, Al, and Pb are $\sigma_{Ag} = 6.01\times10^5 + i7.46\times10^4$ (1/Ω-cm), $\sigma_{Al} = 3.61\times10^5 + i1.02\times10^4$ (1/Ω-cm), and $\sigma_{Pb} = 4.46\times10^4 + i5.50\times10^2$ (1/Ω-cm) at 0.54 THz and $\sigma_{Ag} = 6.38\times10^5 + i1.96\times10^5$ (1/Ω-cm), $\sigma_{Al} = 3.36\times10^5 + i3..00\times10^4$ (1/Ω-cm), and $\sigma_{Pb} = 4.40\times10^4 + i1.60\times10^3$ (1/Ω-cm), respectively. In the optical frequencies, significant differences have been observed in the both transmission peak amplitude and line shape for the arrays made from Ag, Al, and Pb. But in the THz frequency, these dramatic changes were not observed. However, a signature of the transmission enhancement with the higher ratio $-\varepsilon_{rm}/\varepsilon_{im}$ has been observed for the array metals. This trend is consistent with the observation in the optical frequency region.

5. 7 Results of freestanding-metal-arrays

The freestanding-metal-array has air as surrounding dielectric medium and can excite the metal-air [±1, 0] SPP mode. The cutoff frequency for the freestanding metal arrays can be defined by the length along the major axis, 75 μm of the elliptical holes. There should not be any propagation mode when the wavelength of the incidence radiation $\lambda > 2\times75$ μm, which gives a corresponding cutoff frequency of 2.0 THz. To obtain the maximum transmission through the freestanding-metal-arrays, the sample was placed with major axis of the elliptical hole perpendicular to the incidence THz electric filed.

The measured amplitude transmissions through different metallic arrays are shown in Fig. 5-7. The spectra for different arrays are vertically displaced for clarity. The pronounced resonance peaks around 1.60 THz are attributed to the surface plasmon [±1, 0] resonance mode at the metal-air interfaces. The peak amplitude transmission of Ag, Al, and Pb are 82%, 81%, and 72.5%, respectively. The values of ratio $-\varepsilon_{rm}/\varepsilon_{im}$ for Ag, Al, and Pb at 1.60 THz are 0.36, 0.08, and 0.04, respectively. The corresponding transmittances of the freestanding-metal-arrays are shown in Fig. 5-8 with transmittance 67±0.5%, 65±0.4%, and 52.2±0.7%, for Ag, Al, and Pb, respectively. The transmission enhancement through the freestanding-metallic-arrays shows similar properties as observed for the [±1, 0] metal-silicon resonance mode.

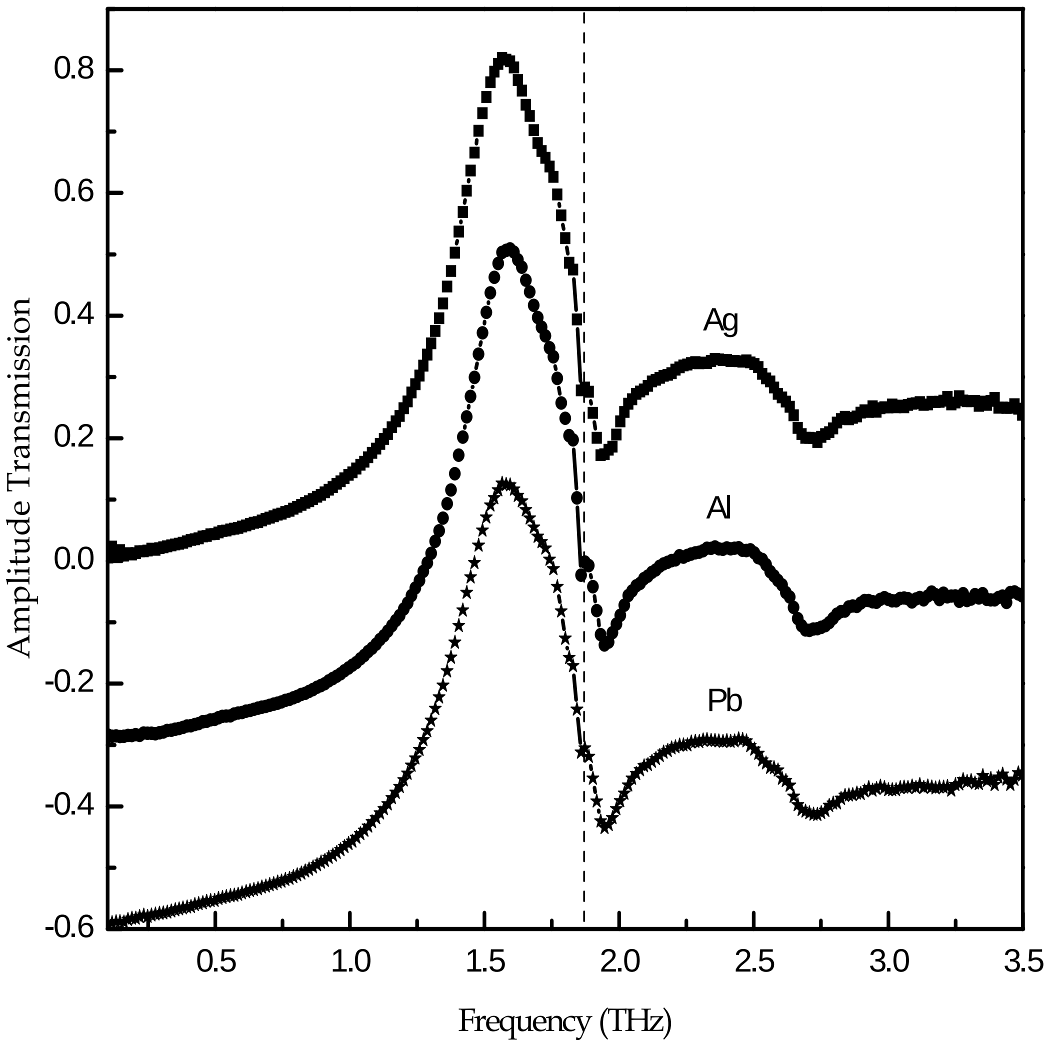

Figure 5-7 Measured amplitude transmission through the freestanding-metal-arrays made from Ag (squares), Al (circles), and Pb (stars), respectively. For clarity, the spectra of Al, and Pb are moved down by 0.3 and 0.6, respectively. The vertical dashed line indicates the calculated surface plasmon [±1, 0] metal-air resonance mode.

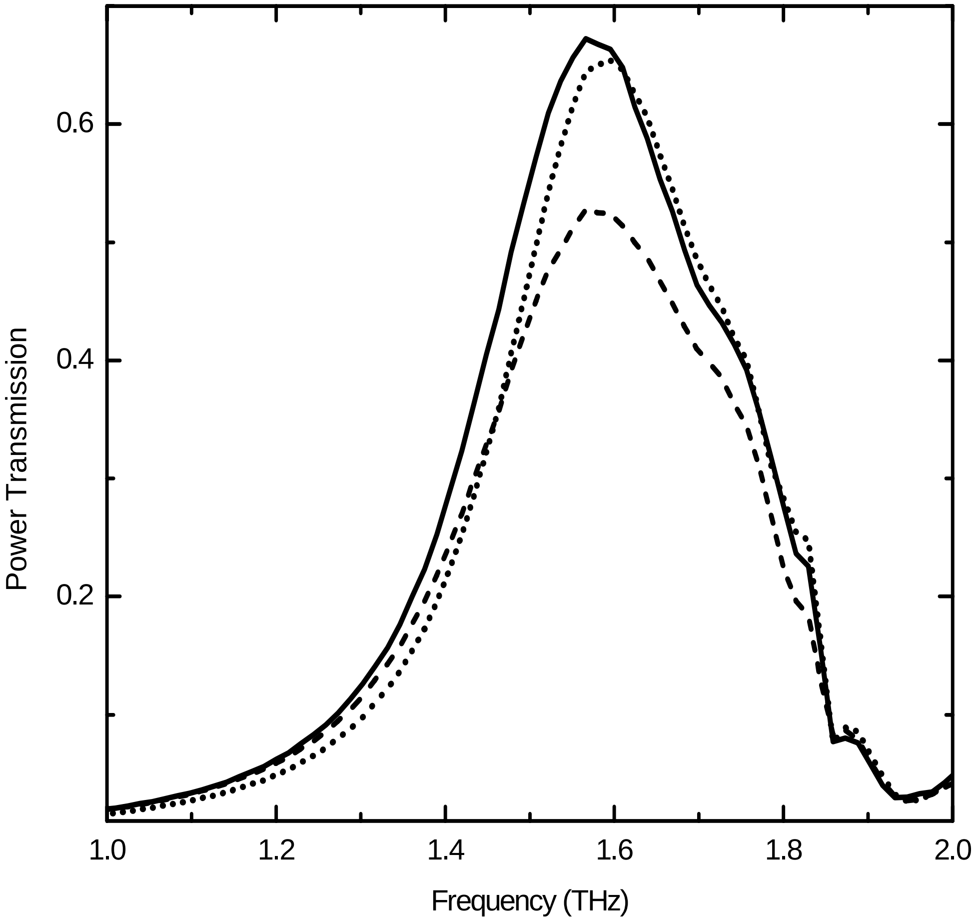

Figure 5-8 Measured transmittance through the freestanding-metal-arrays made from Ag (solid line), Al (dotted line), and Pb (dashed line).

5. 8 Consistency check of the measurements

To check the consistency of the transmission measurement, we made metal-array-on-silicon with three different metal thicknesses in terms of skin-depth. Peak transmissions of [±1, 0] SPPs for metal-silicon interface were measured for Ag, Al, and Pb arrays. The thicknesses of the arrays are selected as one-third, one, and three times of the skin-depth. Graphical presentations of the results are shown in Fig. 5-9 which reveals that Ag has higher transmission than Al and Pb for all thickness. Similarly, Al has higher transmission than Pb.

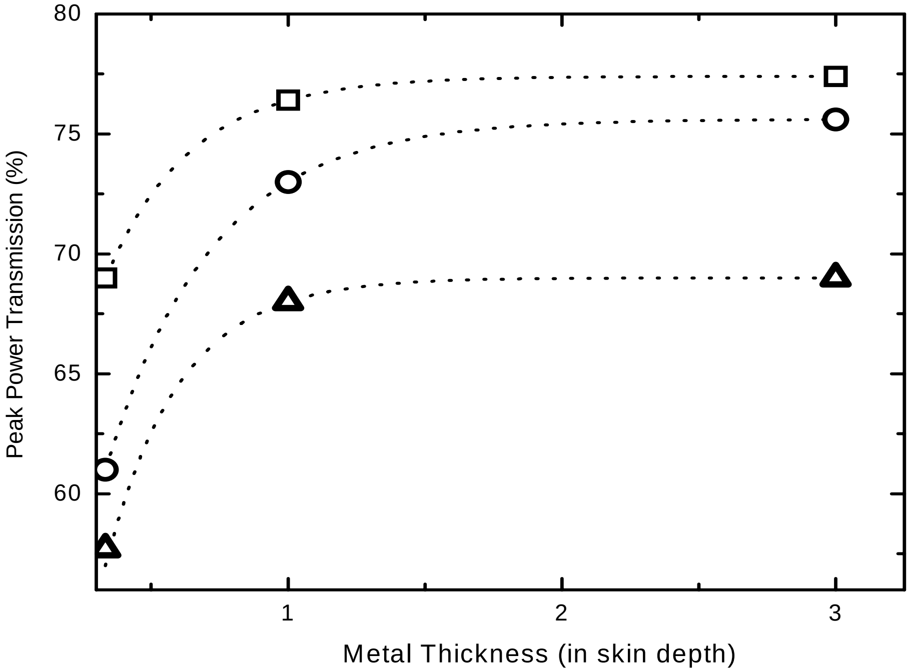

Figure 5-9 Measured peak power of [±1, 0] SPP modes for Ag (open squares), Al (open circles), and Pb (open triangles). The dotted lines are to guide the eyes.

5. 9 Dependence of amplitude transmission on propagation lengths of SPPs

In this section a qualitative explanation of the transmission enhancement with propagation lengths is given. The electric field of a surface plasmon wave propagating on the metal-dielectric surface along x-axis can be described by

$$E = E_0^{\pm} \exp[+i(k_x x \pm k_z z - \omega t)] \qquad (5\text{-}4)$$

where, $k_x = k_x^{/} + ik_x^{//}$ is the complex wavevector along x-axis. The propagation length is defined by the length along the metal surface at which the intensity falls to 1/e.

$$E_x^2 \sim \exp[2k_x^{//}]$$

Propagation length,

$$L_x = 1/2k_x^{//} \qquad (5\text{-}5)$$

The complex k_x is given by,

$$k_x = \frac{\omega}{c}\sqrt{\frac{\varepsilon_m \varepsilon_1}{\varepsilon_m + \varepsilon_1}} = \sqrt{\frac{(\varepsilon_{rm} + i\varepsilon_{im})\varepsilon_1}{(\varepsilon_{rm} + i\varepsilon_{im}) + \varepsilon_1}} \qquad (5\text{-}6)$$

At THz frequencies, $\varepsilon_1 << \varepsilon_m$ and $\varepsilon_{im} > |\varepsilon_{rm}|$, after simplification Eqs. (5-5) and (5-6), we can write,

$$k_x^{//} = \frac{\omega}{c}\frac{\varepsilon_1^{3/2}}{2\varepsilon_{im}}, \qquad \text{and} \qquad L_x = \frac{c}{\omega}\frac{\varepsilon_{im}}{\varepsilon_1^{3/2}} \qquad (5\text{-}7)$$

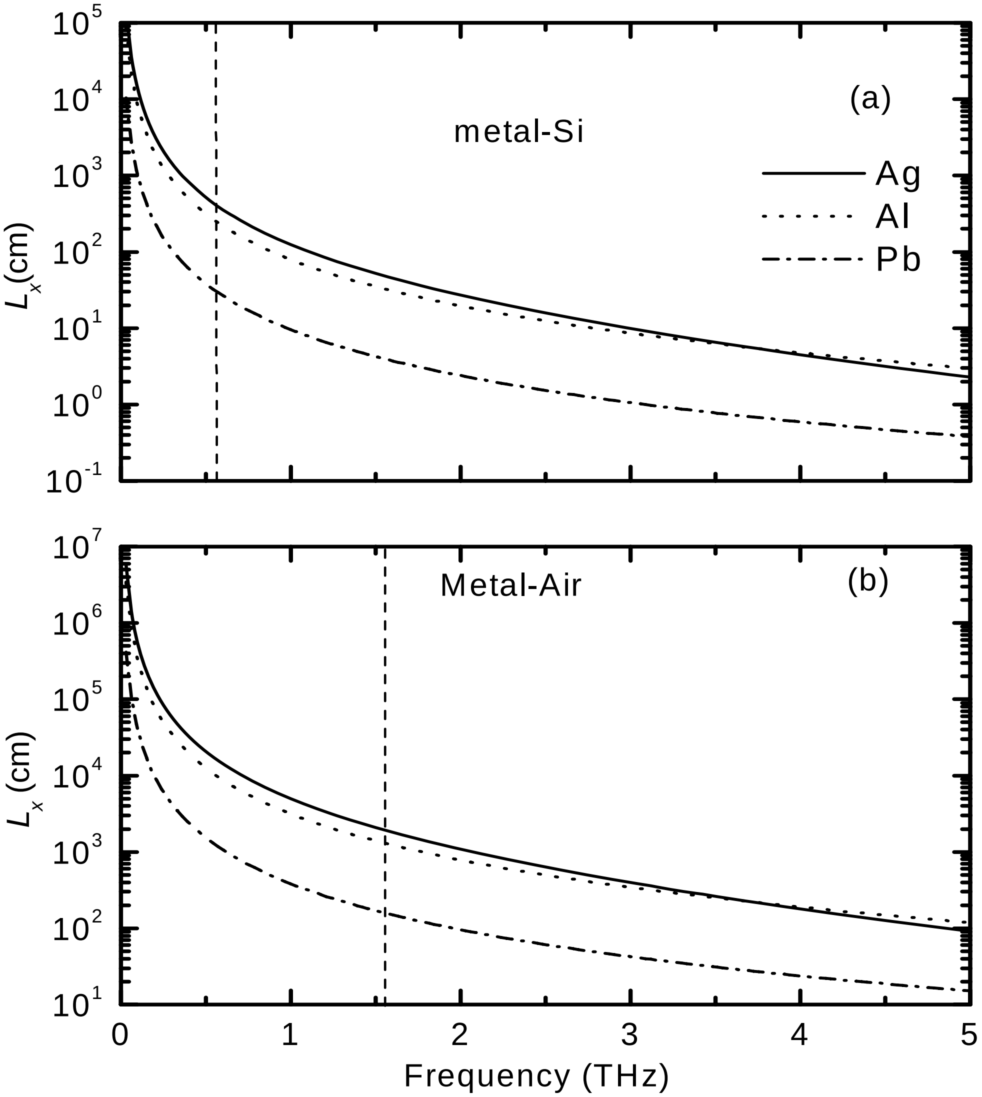

Figure 5-10 (a) Frequency dependent propagation length for metal-silicon interface. Vertical dashed line shows metal-silicon [±1, 0] resonance mode. (b) Frequency dependent propagation length for metal-air interface. Vertical dashed line shows metal-air [±1, 0] resonance mode.

Calculated propagation lengths for metal-silicon interface and metal-air interface are shown in Fig. 5-6 (a) and (b), respectively. Ag, Al, and Pb are represented by solid, dotted, and dashed-dotted lines, respectively. The vertical dashed lines represent resonance frequencies of [±1, 0] mode of metal-silicon and metal-air interfaces.

The propagation length depends on the internal absorption which is governed by $k_x^{//}$. The SPPs excite electron-hole at the Fermi level and the following de-excitation produces phonons and thus heating. This phenomenon of losing energy of the SPPs known as internal damping. The propagation length calculated above by assuming that the surface is smooth. For the rough surface two additional processes have to be regarded which influence the propagation length: transformation of SPPs to electromagnetic radiation into the free space via roughness and the other is scattering of the SPPs into other SPPs of other direction but without changing the absolute value of the wave vector. The mean free path length of radiation L_{rad} and scattering L_{sc} also depend on the dielectric constant of the material, wavelength of surface plasmon, structure of the roughness, and correlation between structures. The intensity of SPP decreases to 1/e after having traveled these lengths. So the total effect of SPP propagation length L_{tot} is given by [34],

$$\frac{1}{L_{tot}} = \frac{1}{L_x} + \frac{1}{L_{rad}} + \frac{1}{L_{sc}}$$

A more detail theoretical calculation is needed to find values of all characteristic lengths to find the effective propagation length on the corrugated surface. The measured amplitude transmission shows higher enhancement for the metal which has the higher L_x propagation length than the other. For our both experimental results we compared the transmission enhancement and the corresponding propagation length which is qualitatively follow the same order. Propagation lengths L_x of the surface plasmons are very high compared to the periodicity of the square hole arrays as well as the sample size. Our experimental results show a direct consequence of the propagation length L_x on transmission enhancement.

CHAPTER VI

RESONANT TRANSMISSION OF OPTICALLY THIN HOLE ARRAYS

Till now, investigations of SPP resonances have focused on optically thick subwavelength hole arrays in both optical and low frequency regions. In the arrays of doped silicon an exponential decay in the peak transmission was observed as the array thickness increased to orders of magnitude higher than that of the skin depth. It is intriguing how the SPP resonances are developed in metallic arrays of sub-skin-depth thickness. In this Chapter an experimental demonstration has been carried out to understand the resonant terahertz transmission through subwavelength hole arrays patterned on metallic films with thickness less than skin depth. Experimental results have revealed a critical array thickness, above which the SPP resonance begins to establish. The maximum amplitude transmission is achieved when the thickness of metal films approaches skin depth. However, enhanced terahertz transmission of up to nine tenths of the maximum transmission can be realized at a film thickness comparable to the skin depth at wavelengths of light, which is only one third of the skin depth at 0.55 THz

6. 1 Skin depth of THz SPP in metals

One of the properties of SPPs is that they propagate along the surface of metal-dielectric interface and decay exponentially in both medium perpendicular to the surface. The electric field has its maximum on the interface. Consider Fig. 6-1 which has a metal dielectric interface at $z = 0$ along x direction.

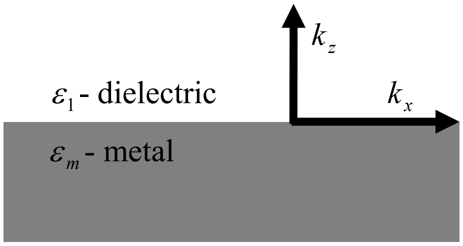

Figure 6-1 Schematic diagram of metal-dielectric interface along x direction.

Surface plasmons propagating along x direction is described by the electric fields as,

$$E = E_0^{\pm} \exp[+i(k_x x \pm k_z z - \omega t)] \tag{6-1}$$

with + for $z \geq 0$, - for $z \leq 0$, and with imaginary k_z, which causes the exponentially decay of the electric field E. Maxwell's equations yield the retarded dispersion relation for such a plane surface [34]

$$k_{zm} = \left[\varepsilon_m \left(\frac{\omega}{c} \right)^2 - k_x^2 \right]^{1/2} \tag{6-2 a}$$

$$k_{z1} = \left[\varepsilon_1 \left(\frac{\omega}{c} \right)^2 - k_x^2 \right]^{1/2} \tag{6-2 b}$$

with, $$k_x = \frac{\omega}{c} \sqrt{\frac{\varepsilon_m \varepsilon_1}{\varepsilon_m + \varepsilon_1}}$$

where, k_{zm} and k_{z1} are the complex wave vector in metal and dielectric, respectively; $\varepsilon_m = \varepsilon_{rm} + i\varepsilon_{im}$ is the complex dielectric of metals and ε_1 is the dielectric of the surrounding medium. Inside metals imaginary part of the k_{zm} is responsible for the exponential decay of fields, $E \sim \exp[-\mathrm{Im}(k_{zm})]$. The skin depth is defined by the propagation length inside the metal at which the electric field drops to 1/e.

Skin depth δ_m is defined as,

$$\delta_m(\omega) = \frac{1}{\mathrm{Im}(k_{zm})} \tag{6-3}$$

At THz frequencies $\varepsilon_1 << \varepsilon_m$ and $\varepsilon_{im} > |\varepsilon_{rm}|$, Eq. 6-2a can be written as,

$$k_{zm} = \mathrm{Re}(k_{zm}) + i\,\mathrm{Im}(k_{zm}) = \left[\varepsilon_m \left(\frac{\omega}{c} \right)^2 - k_x^2 \right]^{1/2}$$

$$= \left[\varepsilon_m \left(\frac{\omega}{c} \right)^2 - \left(\frac{\omega}{c} \right)^2 \frac{\varepsilon_m \varepsilon_1}{\varepsilon_m + \varepsilon_1} \right]^{1/2}$$

$$= \left(\frac{\omega}{c} \right) \sqrt{\varepsilon_m}$$

After simplification the imaginary part of k_{zm} can be written as,

$$\mathrm{Im}(k_{zm}) = \left(\frac{\omega}{c} \right) \sqrt{\frac{\varepsilon_{im}}{2}} \tag{6-4}$$

Skin depth,

$$\delta_m(\omega) = \left(\frac{c}{\omega}\right)\sqrt{\frac{2}{\varepsilon_{im}}} \tag{6-5}$$

In Chapter 5, the relation between the real part of the conductivity and the imaginary part of the dielectric constant is given as, $\sigma_{im}(\omega) = \varepsilon_0 \omega \varepsilon_{mi}$, using this Eq. (6-5) gives,

$$\delta_m(\omega) = \left(\frac{c}{\omega}\right)\sqrt{\frac{2\varepsilon_0 \omega}{\sigma_{rm}}}$$

$$\delta_m(\omega) = \sqrt{\frac{2c^2 \varepsilon_0}{\omega \sigma_{rm}}} \qquad \text{and } c = \frac{1}{\sqrt{\mu_0 \varepsilon_0}}$$

$$\delta_m(\omega) = \sqrt{\frac{2}{\omega \mu_0 \sigma_{rm}}} \tag{6-6}$$

where, μ_0 is the permeability of the free space. So the skin depth of the THz surface plasmons as expressed in Eq.(6-5) is equivalent to the standard skin depth relation in microwave theory. Based on this relation we calculate the skin depths of lead (Pb), aluminum (Al), and silver (Ag) from the published values of the dielectric constants of metals.

The frequency dependence of the skin depth in the frequency range of our interest is plotted in Fig. 6-2. Vertical dashed lines represent the position of two fundamental resonance modes for metal-silicon and metal-air interfaces. At 0.55 THz, the primary surface plasmon [±1, 0] resonance for metal-silicon interface, the skin depths for Pb, Al, and Ag are 320, 110, and 83 nm, respectively. At 1.60 THz, the fundamental [±1, 0] mode of metal-air interface, corresponding skin depths are 180, 75, and 60 nm for Pb, Al, and Ag, respectively.

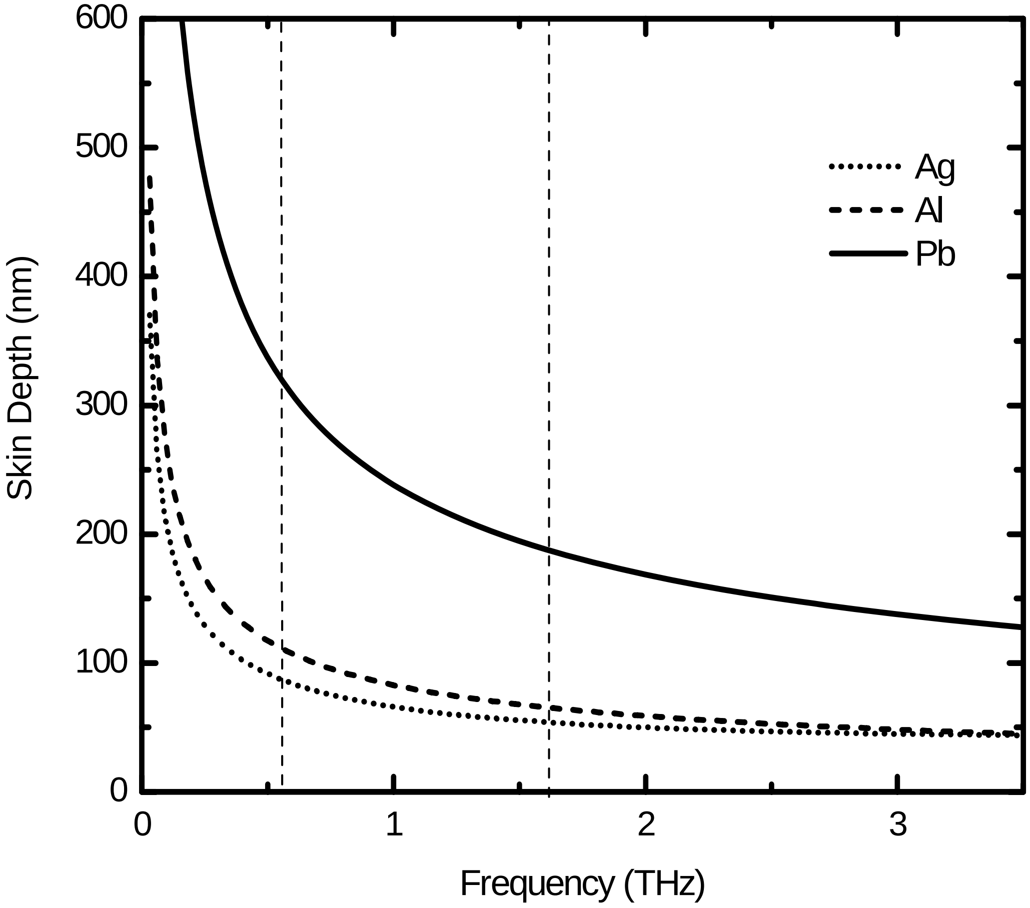

Figure 6-2 Frequency-dependent skin depths of Ag, Al, and Pb calculated from the published values of the dielectric constants. Vertical dashed line, the [±1, 0] surface-plasmon mode at 0.55 THz for the Pb-Si interface.

6. 2 Sample Preparation

Lead (Pb) has been chosen as the constituent metal of the arrays for two reasons. First, extraordinary terahertz transmission in Pb subwavelength hole arrays has been demonstrated with an amplitude efficiency of up to 82% at 0.55 THz for array-on-silicon, which is very close to the performance of arrays made from good electrical conductors such as Ag, Al and Au as demonstrated in Chapter 5. Second, the skin depth of Pb at 0.55 THz is 320 nm, nearly three times of that of Ag and Al. It thus provides a large dynamic range to characterize the evolution of SPP resonance at sub-skin-depth thickness.

Pb arrays with various thicknesses ranging from 60 to 1000 nm were prepared. Sample fabrication process is similar described in Chapter 5. The thin metallic film of lead (Pb) is deposited on a 0.64-mm-thick p-type silicon wafer with a resistivity of $\rho = 20\ \Omega$-cm. Conventional photolithographic process is used to form a 100 μm × 80 μm rectangular hole arrays.

During metallization, the thickness of the metal films controlled with high precisions to get the right thickness. The thickness of the metal deposited on deposition monitor is different than that of the substrate because they have different distances and different angles. A correction factor, called tooling factor, should be obtained for any particular position of the substrate and the monitor to get the accurate film thickness on the substrate. A water cooled deposition monitor FMT6 has a thickness resolution of 0.1 nm. Deposited metal on the monitor's quartz crystal changes its frequency. The change in the frequency and the density of the deposited metal is used to calculate the thickness of the film. To find the tooling factor, three different-thickness-samples were prepared for a particular position of the substrate with respect to the monitor. We recorded the corresponding thicknesses showed in the monitor. The chamber pressure was 2.5×10^{-5} MB and was not allowed to exceed 3.0×10^{-5} MB during the deposition. We adjusted the current to get a deposition rate 1-2 nm/s. After deposition the film thicknesses were measured by atomic microscopy (AFM) system which showed that the real thickness of the metal films on the substrate was approximately 60% of the thickness observed on the monitor. Generally, the thickness of metal film is governed by the cosine law. A schematic diagram of the deposition and the substrate is shown in Fig. 6-3

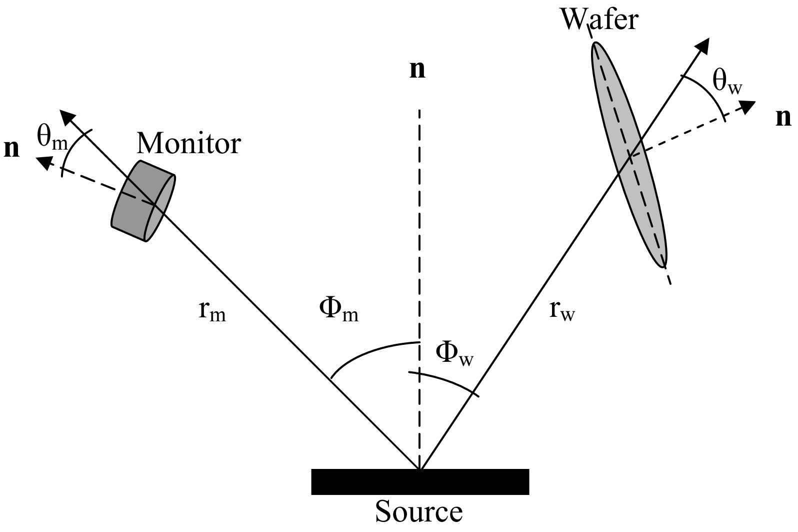

Figure 6-3 Schematic diagram of the deposition monitor and substrate in a vacuum chamber. **n** is the unit vector perpendicular to the surface of substrate or monitor.

In conventional thermal deposition system or physical vapor deposition process the sticking coefficient of the deposited metal is independent of the metal flux incidence angle or energy [47]. Within 0-20˚ impact angle the sticking coefficient is maximum [48]. In general, metal has a very high sticking coefficient for Si <100> substrate and almost unity [49]. Thickness of the deposited film on a surface

$$d = \frac{Me}{\pi r^2} \cos\phi \cos\theta$$

where, *Me* molecular weight, r is the distance of the substrate from source, ϕ is the angular position of the substrate, and θ is the angle between the substrate normal and the direction of flux. The measured value of r, ϕ, and θ for substrate were 210 mm, 23°, and 7°; and for monitor those were 160 mm, 21°, and 25°. If we consider the sticking coefficient of monitor crystal and silicon substrate are same then the calculated tooling factor was ~62%, which was fairly close to the measured value. To find the real thickness of the substrate film, the monitor thickness was always scaled by 60%.

For every metallization, the samples were carefully placed in the same position. For thin film the deposition rate was ~ 0.2-0.3 nm and for the thick film was 1.0-2.0 nm. Density of Ag, Al, and Pb are 10.49, 2.70, and 11.34, respectively.

6. 3 THz measurements

In the terahertz time-domain spectroscopy (THz-TDS) measurements, the input terahertz pulses are polarized along the minor axes (80 μm) of the rectangular holes and penetrate the array at normal incidence. Several transmitted pulses are shown in Fig. 6-4.

Transmitted THz pulses through reference silicon and metal arrays of different thickness are recorded in the time domain. THz pulses transmitted through 60 nm thick arrays shows only attenuation in the pulse amplitude. Arrays of thickness 75 nm shows huge attenuation and ringing structures appear in the pulse followed by the main pulse.

In Fig. 6-5, evolution of the SPP resonance as a function of the array film's thickness is depicted in the Fourier-transformed spectra of the reference and the samples. When the array film is thin, the spectrum shows no resonance but similar features of the reference spectrum with attenuation. At 64 nm, which is observed as a critical thickness for the Pb array, the SPP resonance excited at the Pb-Si interface appears in the spectrum. Above this critical thickness, the resonance peak is enhanced with thicker array film.

In the experiments we found that the deterioration of metal surfaces of the arrays may cause the decline in transmission efficiency. To keep surface-dependent variation to a minimum, the THz-TDS measurements were carried out immediately after completion of the metallization process.

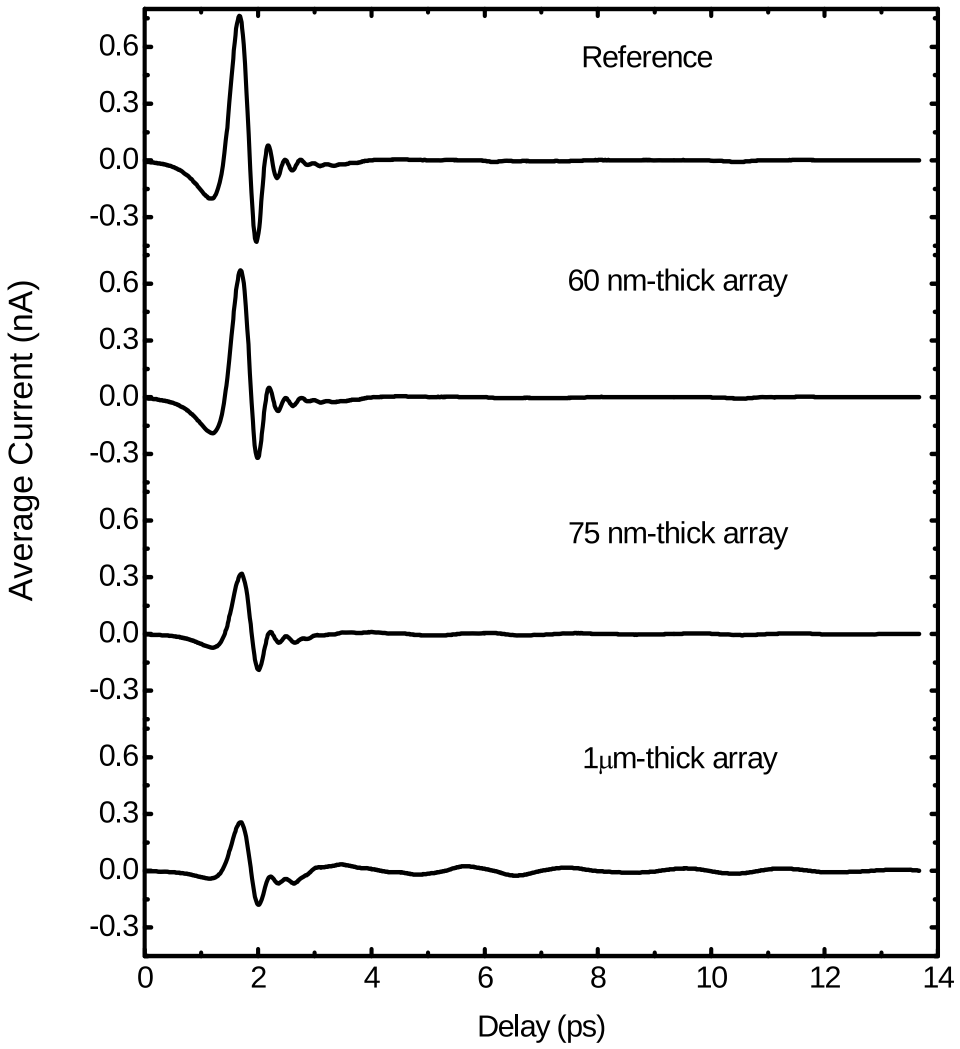

Figure 6-4 Measured THz pulses through reference and the Pb arrays of thickness 60 nm, 75 nm, and 1μm.

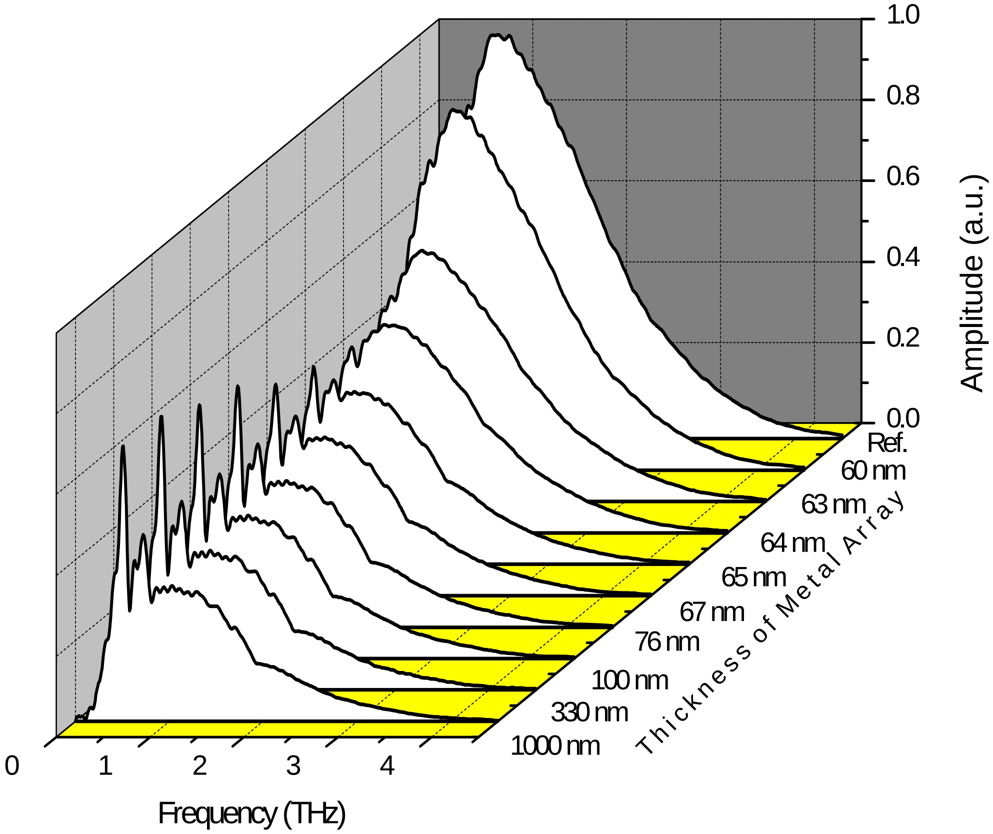

Figure 6-5 Fourier-transformed spectra of the transmitted THz pulses through reference and the subwavelength Pb hole arrays with different film thickness.

6. 4 Analysis of sub-skin-depth SPP

The frequency-dependent amplitude transmission of arrays, defined by the ratio $T(\omega)=\left|E_{sample}(\omega)/E_{reference}(\omega)\right|$, with different film thicknesses is shown in Fig. 6-6. For clarity the curves are vertically displaced. Measured transmission clearly reveals two regions of thickness dependence. Below the critical thickness, 64 nm, the frequency-dependent transmission is nearly flat, showing no resonance peak. Above the critical thickness, a resonance at 0.55 THz appears in the spectra, whose amplitude increases with array thickness while the background transmission is reduced at the same time. This resonance is attributed to the excitation of SPPs at the Pb-Si interface.

The resonance at 0.55 THz corresponds to the [±1, 0] surface-plasmon mode for arrays with L = 160 μm at the Pb-Si interface. Below the critical thickness the metal arrays can not provide in-plane grating momentum which interplays momentum conservation between incidence light and surface plasmons. Immediately above the critical thickness, the resonance amplitude is very sensitive to the thickness of arrays. The dependence of the peak transmission on the thickness above the critical thickness is shown in Fig. 6-7. The amplitude transmission efficiency increases exponentially when the array thickness is below 100 nm. It then saturates gradually and approaches the maximum at the skin depth. The solid line in Fig. 6-7 shows the exponential fitting of the peak amplitude transmission which agrees well with experimentally obtained results.

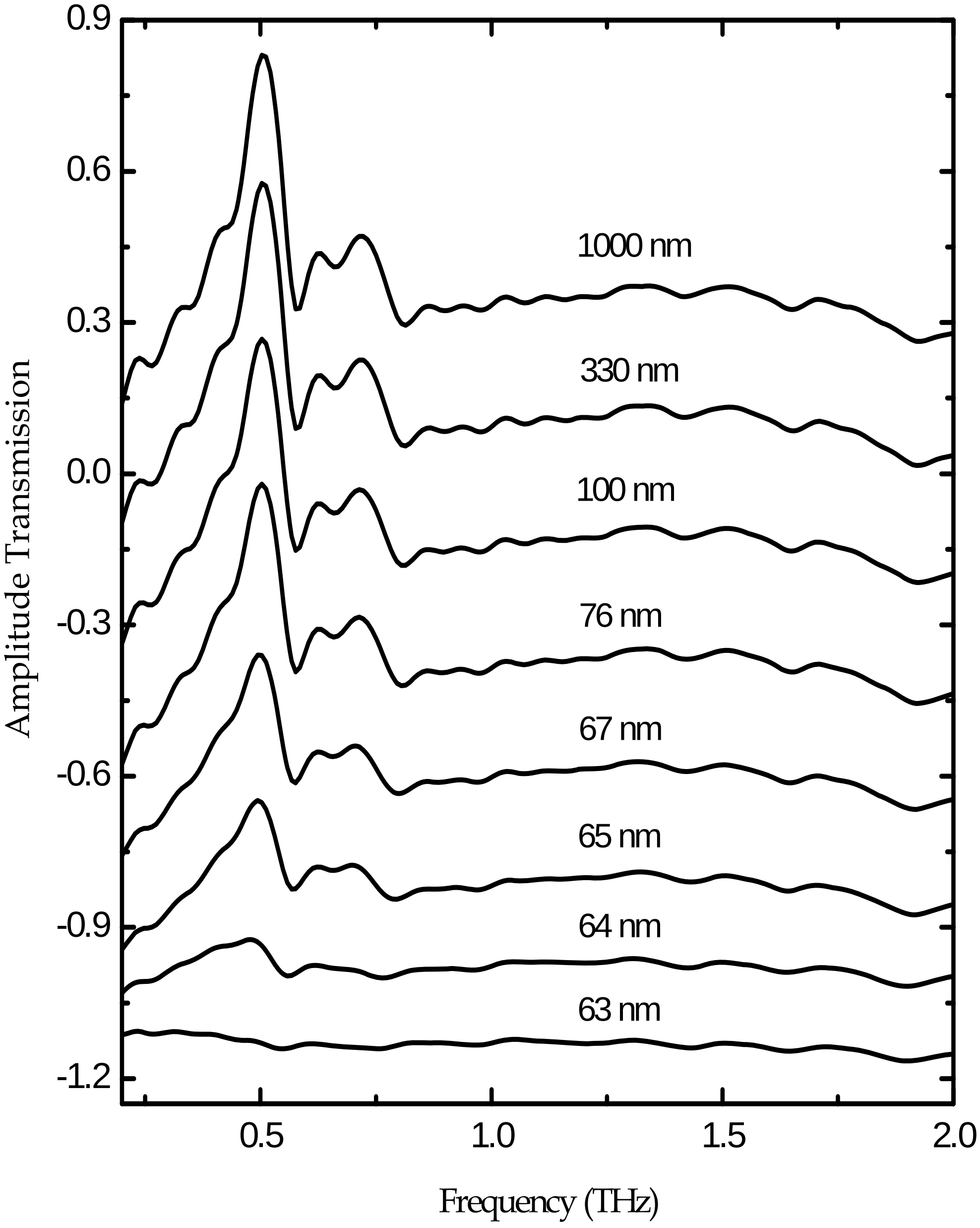

Figure 6-6 Measured amplitude transmission of Pb arrays with different thickness. The curves are vertically displaced for clarity.

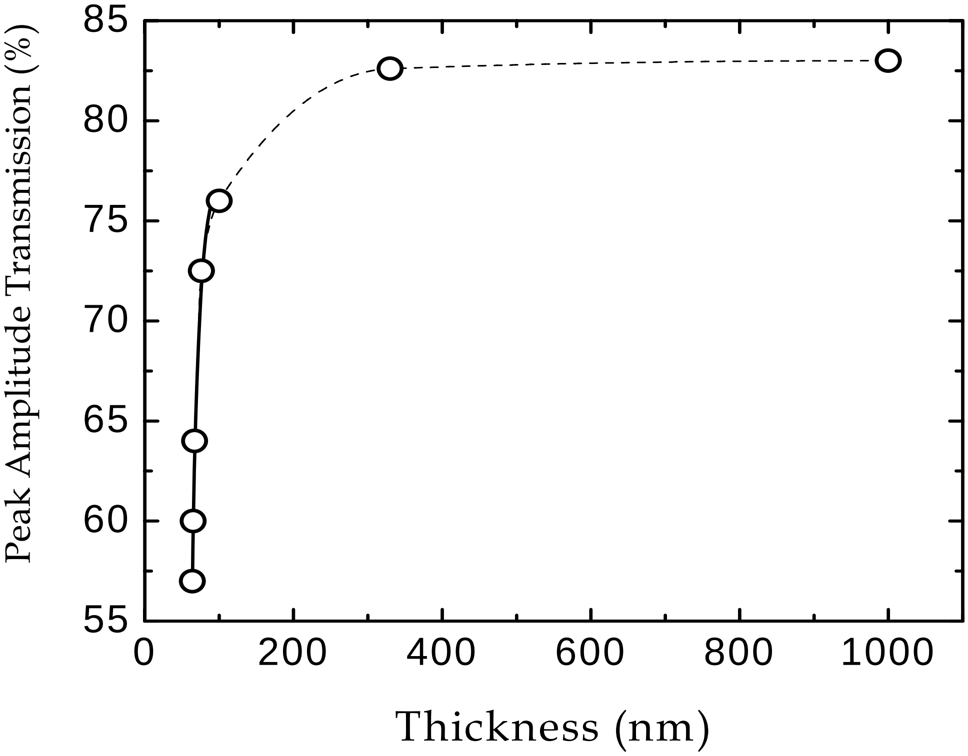

Figure 6-7 Measured peak amplitude of [±1, 0] surface plasmon mode at 0.55 THz as a function of the Pb thickness (open circles), connected by a dashed line to guide the eye. The solid line is an exponential fit for the region of array thickness below 100 nm.

It is worth noting that a transmission efficiency as high as 76% is achieved at the array thickness of 100 nm, only one-third of the skin depth. This value is more than nine tenths of the maximum transmission efficiency achieved at skin depth. For comparison, we have fabricated two additional arrays of same structure but made from Ag and Al. The film thicknesses are 27 nm for Ag and 36 nm for Al; also one-third of their corresponding skin depths. The measured transmission efficiencies are 83.5% and 77.5%, respectively, for Ag and Al arrays. The transmission of Ag and Al arrays of sub-skin-depth thickness are compared with the transmission obtained in Chapter 5 with optically thick metallic arrays made from similar metals. Comparison shows that, all sub-skin-depth arrays have transmission above nine tenths of their maximum transmission efficiencies.

CHAPTER VII

PHOTO-INDUCED SPPs OF SILICONCON SUB-WAVELENGTH HOLE ARRAYS

The tunable properties of surface plasmons are challenging and may lead to miniaturized and active photonic devices and circuits. As well known that the dielectric function of the constituent metals and the surrounding dielectric media plays a substantial role in establishing the surface-plasmon-enhanced transmission. By altering the dielectric function of either the metal or the surrounding media instantaneously the properties of surface plasmons can be tuned in a dynamic range. Recently, by use of nematic liquid crystal as the surrounding media, the resonance frequencies of surface plasmons in the subwavelength hole arrays were tuned simultaneously when the dielectric constant of the liquid crystal media was altered through external magnetic field [50]. However, modifying the dielectric function of metals in a noticeable dynamic range is impossible and still remains challenging. The advantage of semiconductors is that the dielectric function can be modified by changing the number density of free carriers through variable doping concentration, temperature, or optical excitation. This in turn enables tuning and switching of surface plasmons. Recently, switching of THz SPPs in a subwavelength arrays made from doped semiconductor have demonstrated as a result of thermal effect and optical illumination of the arrays [51,52].

This chapter demonstrates enhanced THz transmission through optically excited subwavelengh-silicon-hole-arrays. Dynamic transition of surface-plasmon resonance from out-of-plane photonic crystal effect is observed in a semiconductor array of subwavelength holes under intense optical excitation and probe by teraherz. The dielectric properties of the photo-excited array, well described by the Drude-Smith model, are essentially altered by the intense optical excitation due to photogenerated free carriers. As a result, the array becomes metallic and favors the coupling and propagation of surface plasmons. The well-defined photo-induced maxima and minima shown in the zero-order terahertz transmission spectra are attributed to the fundamental surface-plasmon modes and the Wood's anomaly, respectively.

7. 1 Experimental setup

The terahertz system used in the measurements employs conventional optical pump-terahertz probe with a usable bandwidth of up to 2.5 THz [53]. The terahertz pulses are generated from a 2 mm-thick ZnTe crystals by optical rectification and are detected via an electro-optical sampling process in another 1 mm-thick ZnTe crystal. A femtosecond regenerative Ti:sapphire amplifier (Hurricane, Spectra-Physics), capable of generating 750 mW of average power with a pulse duration of 100 fs and a repetitions rate of 1 kHz, is used as the optical source for terahertz pulse generation, detection, and the silicon array excitation. The generated terahertz radiation is guided towards the detector by using four parabolic mirrors of focal lengths about 4 inches in a confocal configuration. The terahertz focal spot size between the two inner parabolic mirrors is 0.74 mm. The sample is placed at 3 mm before the focal spot, where the terahertz beam diameter is about 1.50 mm. The optical excitation beam is 1.76 mm in diameter and overlaps well with the terahertz spot on the sample.

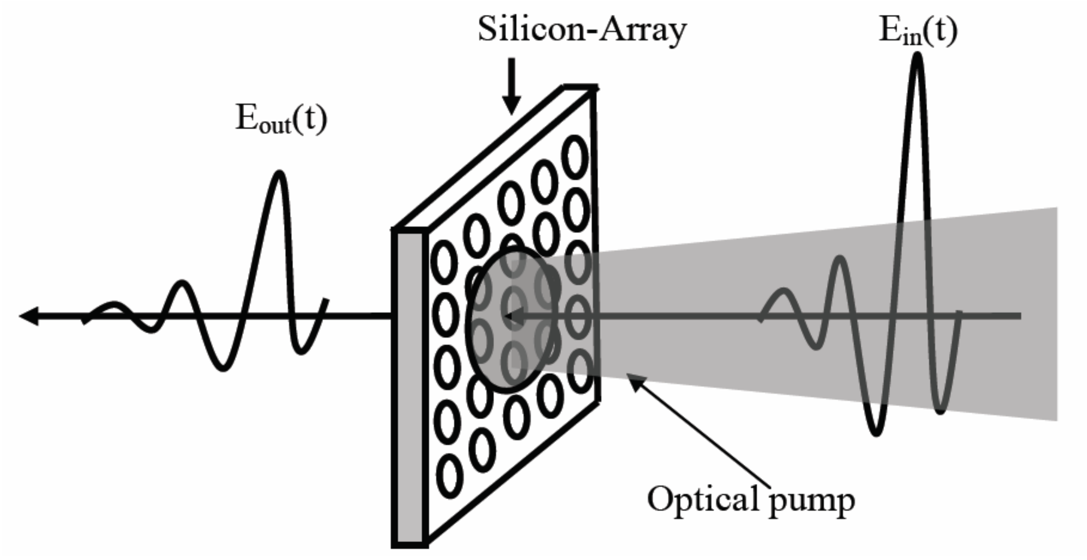

Figure 7-1 Schematic diagram of optically excited SPPs.

The hole arrays used in this experiment was made from a commercially available 30-μm-thick n-doped silicon wafer with a resistivity of 10-Ω cm and a corresponding carrier concentration of $4\times10^{14}\,\mathrm{cm}^{-3}$. The silicon wafer is fairly transparent to the THz radiation in the absence of optical excitation at room temperature. The sample was processed by using standard photolithography and reactive ion etching (RIE) techniques as explained in Chapter 4. The sample is a 10 mm×10 mm subwavelength hole arrays of square lattice with a periodicity of 160 μm. Holes have the dimensions of 80 μm along the major axis and 40 μm along the minor axis. The schematic diagram of optical pump and THz probe set up is shown in Fig. 7-1.

Solid gray color shows the idea of optical excitation (λ = 800 nm) on one surface of the arrays. Due to the finite propagation length of the excitation optical beam the silicon array can be considered as a stack of photo-excited/non-excited silicon. The propagation length at λ = 800 nm is approximately 10 μm [54]. Upon excitation the dielectric properties of 10-μm-thick-excited-layer are altered and allow the formation of SPPs. The propagated THz beam then encounters a stack of Air/excited-silicon(10 μm)/unexcited-silicon (20 μm). The p-polarized THz beam has a diameter of 1.50 mm on the sample surface which is expected to cover more than sixty holes of the arrays.

7. 2 Measurements

To measure the optically excited SPPs the silicon-arrays was attached to a 5.0 mm-diameter aperture centered on the terahertz beam and a similar clear aperture is used to obtain the free space reference terahertz radiation. The system was placed in a plastic chamber and purged with nitrogen. The optical excitation beam was focused on the array surface centered on both THz beam and the aperture holder with a diameter of 1.76 mm. The incident light on silicon generates photo-carriers which are subjected to recombination and the time between creation and recombination of the photo-carriers is called the carrier life time (τ). Due to the indirect band gap the recombination of photo-carriers in single crystal bulk silicon requires very high carrier life time (τ ~ 20 ms) [55]. The femtosecond laser pulses had a repetition rate of 1 kHz, corresponding to 1 ms pulse separation which is less than the carrier life time of the silicon arrays. The photo-excitation femtosecond laser pulse hits the array surface 67 ps before the THz pulse. Due to the RIE assisted under cutting the hole size and shape was not identical on the both surface of the silicon arrays. The array was excited by the optical pump from the smaller hole side which had elliptical shape.

The THz pulses transmitted through the clear aperture and the arrays before and after photo-excitation were recorded under the normal incidence geometry. The arrays were placed in two orthogonal orientations: major axis of the elliptical hole perpendicular to the THz electric field and major axis parallel to the THz electric field which were represented as perpendicular and parallel orientations, respectively. Fig. 7-2 shows the THz pulses transmitted through reference and samples.

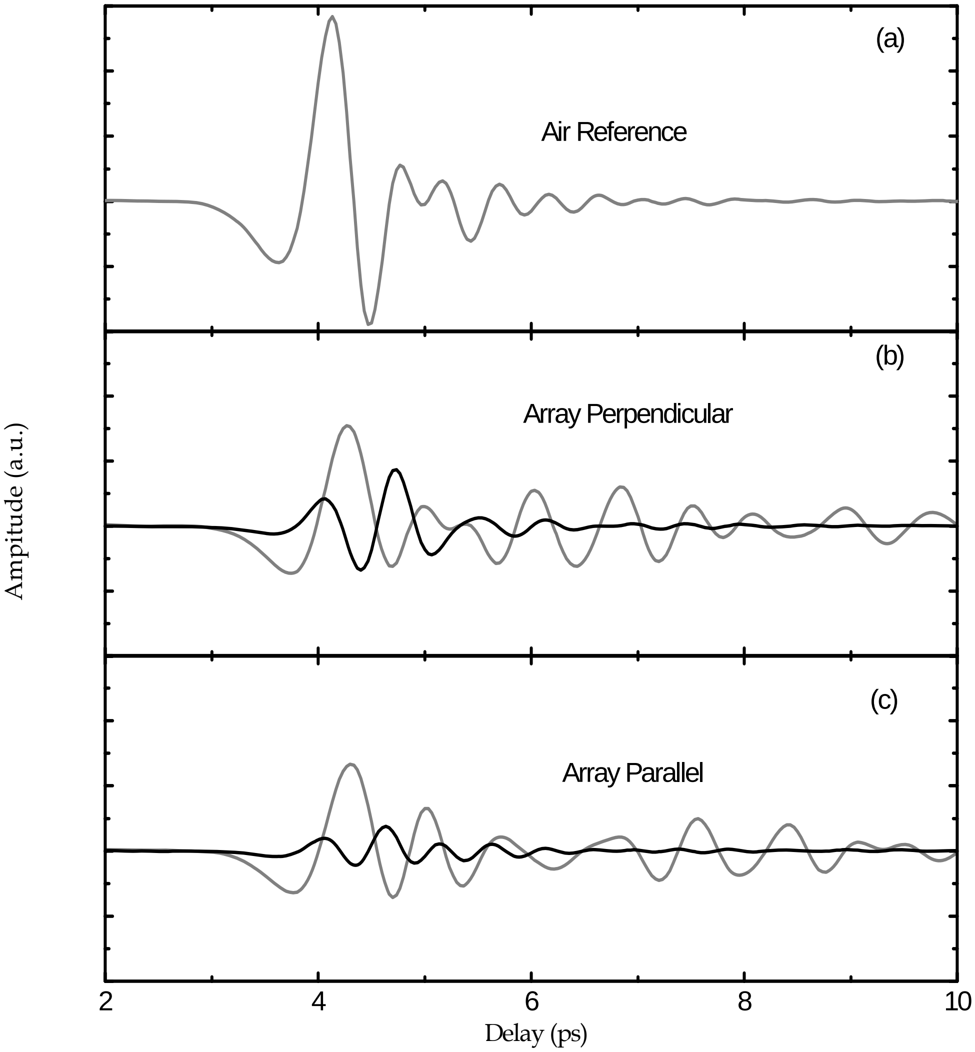

Figure 7-2 Measured transmitted THz pulses through (a) clear aperture (b) silicon arrays in perpendicular orientation, and (c) silicon arrays in parallel orientation. Grey lines represent the THz pulses before photo-excitation and black lines represent the THz pulses under intense optical excitation with 111 mW of average power.

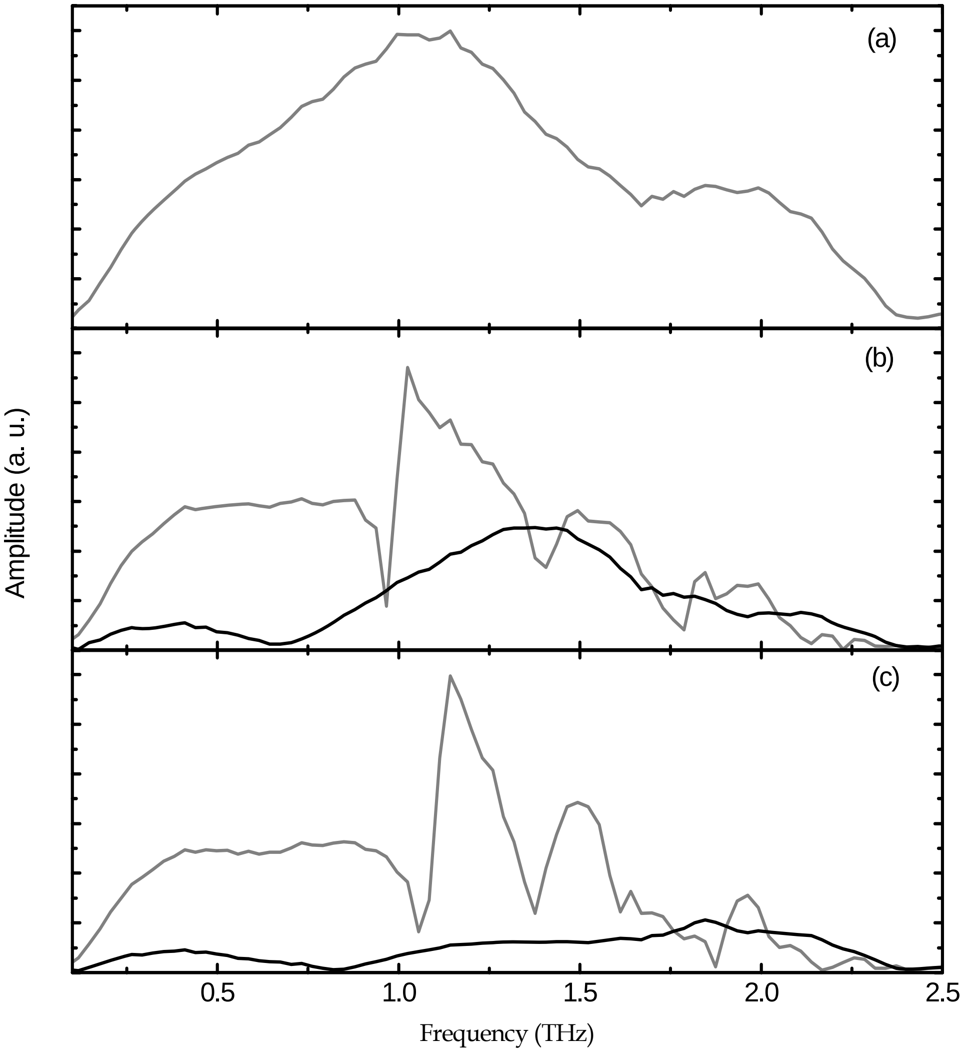

Figure 7-3 Frequency dependent spectra of the measured THz pulses transmitted through (a) clear aperture (b) silicon arrays in perpendicular orientation, and (c) silicon arrays in parallel orientation. Grey lines represent the THz pulses before photo-excitation and black lines represent the THz pulses under intense optical excitation with 111 mW of average power.

Fig. 7-3 shows the corresponding frequency spectra of the measured THz pulses. In the absence of the intense optical excitation the transmission spectra through silicon arrays show complicated spectral structure. Periodic dips are appeared in the frequency dependent spectra. Observed period of the perpendicular orientation is 0.4 THz but for the parallel orientation is about 0.3 THz. Similar structure has been observed when a planner silicon photonic crystal is illuminated with THz radiation at normal incidence [56]. Under the influence of the intense optical excitation those complicated structure disappeared from the spectra in stead a completely new peak appeared at different frequency of the spectrum. These dramatic changes of the spectra are described as the result of the photo-carriers generated in the optically excited portion of the silicon arrays. The amplitudes of the time-domain THz pulses reduced under the optical excitation in both orientations.

To get an idea of THz propagation through the silicon only at the similar photo-excitation condition, a piece of unstructured-blank silicon wafer of similar to the arrays was used. Due to the finite thickness of the silicon wafer, 30 μm, the transmitted THz pulses suffer from multiple reflections. The main THz transmitted pulse could not be separated from the multiple reflection pulses. However, under the intense optical illumination (110 mW) generated photo-carriers change the dielectric properties of the excited portion of the silicon. The transmitted THz pulses and the corresponding spectra through the silicon wafer before and after photo-excitation are shown in Fig. 7-4. Under intense optical excitation transmitted THz signals attenuate severely and Fig. 7-4c reveals that between 1.2-2.0 THz amplitude transmission is below 5% when compared with free space.

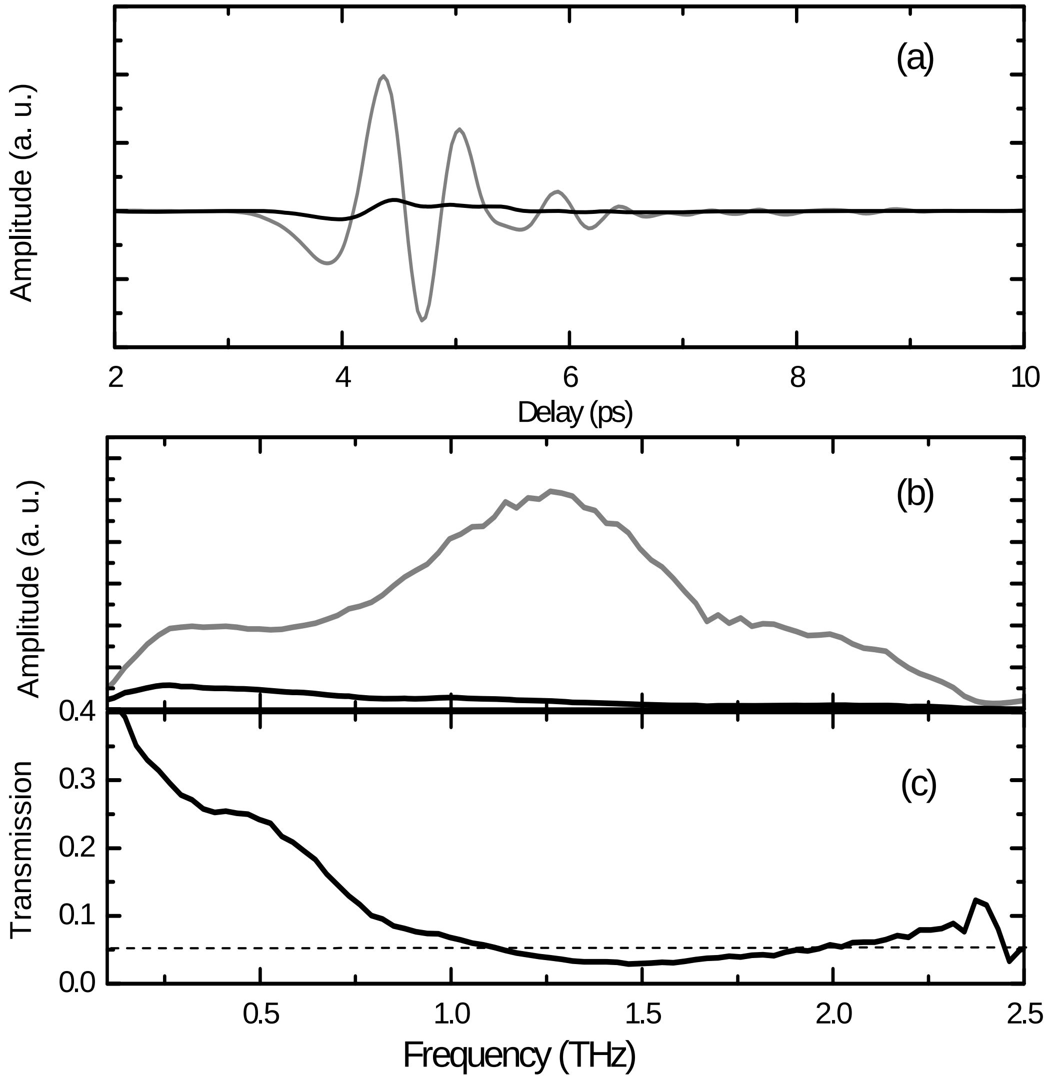

Figure 7-4 (a) Transmitted THz pulses through clear silicon before (gray line) and after (Black line) photo-excitation. (b) Corresponding frequency dependent spectra. (c) Amplitude transmission spectra of the photo-excited silicon (111 mW) defined as the ratio of propagation through free space and excited silicon. The horizontal line indicates 5% transmissions.

7. 3 Results of enhanced THz transmission due to optical excitation

The frequency-dependent amplitude transmissions of the photo-excited array for both orientations are plotted in Fig. 7-5. The amplitude transmission is determined by the ratio of $\left|E_{sam}(\omega)/E_{ref}(\omega)\right|$, where $E_{sam}(\omega)$ and $E_{ref}(\omega)$ are the transmission spectra of the terahertz pulses through the silicon array under optical excitation (111 mW) and the air reference, respectively. The observed transmission enhancement is attributed to the fundamental surface plasmon 1.5 [±1, 0] THz mode for perpendicular orientation, and 1.8 [0, ±1] THz for parallel orientation occurred at the metallic silicon-air interface. The orientation-dependent transmission properties are consistent with those of the highly doped silicon hole arrays explained in Chapter 4. Fig. 7-5 reveals that the optical excitation favors to excite the SPPs in the silicon arrays.

As seen from the previous section, the optically excited clear silicon wafer behaves like a metal film and the transmission is lower than 5% above 1 THz. According to the classical diffraction theory subwavelength holes of the arrays should not support high transmission below the cutoff frequency which defined by the hole size. The transmission peak of perpendicular and parallel orientation show amplitude transmission about 70% and 40%, respectively. The peak frequencies are observed below the cutoff frequency (1.87 THz). The transmission spectra of the photo-excited arrays have completely different transmission characteristics than the unexcited arrays. The photonic bandgap features of the unexcited arrays are disappeared under the influence of optical excitation.

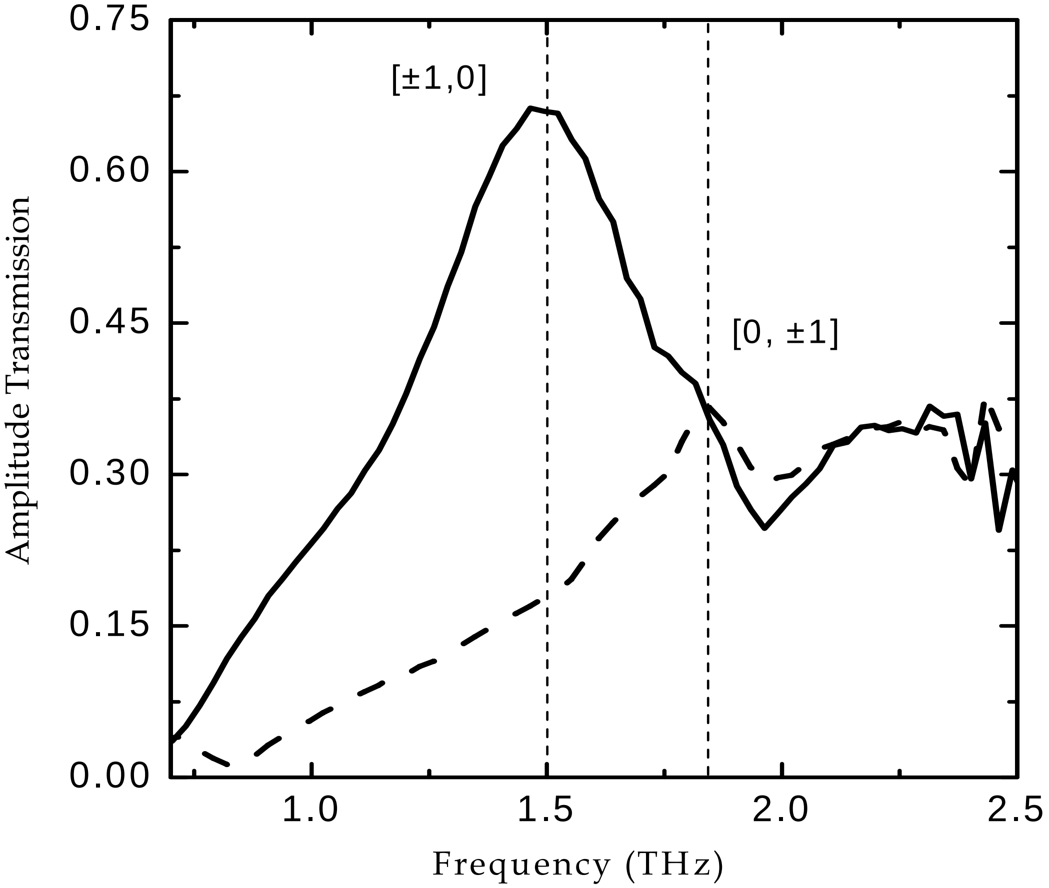

Figure 7-5 Spectra of transmission magnitude of THz pulses through the silicon arrays under the influence of 111 mW optical excitation. The perpendicular and parallel orientations are represented by solid line and dashed line, respectively. Vertical dashed lines represent the measured peak position of the fundamental [±1, 0] SPP resonance mode.

These resonance modes are approximately described by the dispersion relation for two-dimensional metallic gratings with a square lattice at normal incidence, $\lambda_{sp}^{m,n} = \left(L/\sqrt{m^2+n^2}\right)\sqrt{\varepsilon_1\varepsilon_2/(\varepsilon_1+\varepsilon_2)}$, where $\varepsilon_2 = \varepsilon_{r2} + i\varepsilon_{i2}$ is the complex dielectric constant of the metallic medium, and ε_1 is the dielectric constant of the surrounding medium; L is the lattice constant; m and n are the integer mode indices. The metallic behavior of the array medium is mainly determined by the negative value of real dielectric constant, $\varepsilon_{r2} < 0$. The unexcited silicon used for the array has a positive value of ε_{r2} and does not favor the establishment of surface plasmon resonances. Under the influence of intense optical excitation, the array sample becomes a complex multilayer medium, composing of a stack of photoexcited silicon and silicon layers. At terahertz frequencies, the ε_{r2} value of the photoexcited layer may turn to negative under appropriate laser excitation and hence the sample behaves as a metallic array. The thickness of the photoexcited layer depends on the penetration depth δ_L at the excitation laser wavelength, here $\delta_L = 10\,\mu\text{m}$ for silicon at $\lambda = 800\,\text{nm}$ [54].

Figure 7-7 shows the frequency-dependent complex dielectric constant of the photoexcited silicon layer at 111 mW laser excitation. As can be seen, the real part of dielectric constant turns to negative above 0.8 THz. At 1.5 THz, the [±1, 0] surface plasmon mode for perpendicular orientation, the real and imaginary part of the dielectric constant are $\varepsilon_{r2} = -50$ and $\varepsilon_{i2} = 85$, respectively. Optical excitation generates equal number of electrons and holes. Due to the higher mobility, electrons are considered to be the main contributors to the electrical conductivity. Measured conductivity and dielectric constants are tried to fit with the simplified Drude model, which cannot explain the measured data. Smith model which is the modified version of the Drude model can fit the data better [57]. Fig 7-6 and Fig 7-7 show conductivity and dielectric constant of the photo-excited silicon, respectively: the open circles show the measured values, dotted lines are the Drude fitting, and the solid curves are the Drude-Smith fitting, respectively. The complex dielectric constant can be written based on the relation $\varepsilon(\omega) = \varepsilon_r + i\varepsilon_i = \varepsilon_\infty + i\sigma(\omega)/\omega\varepsilon_0$. According to the Smith model the complex conductivity, $\sigma(\omega)$ has a general form [57],

$$\sigma(\omega) = \frac{\varepsilon_0 \omega_p^2 \tau}{(1 - i\omega\tau)} \left[1 + \sum_{n=1}^{\infty} \frac{C_n}{(1 - i\omega\tau)^n} \right], \tag{7-1}$$

where $\omega_p{}^2 = Ne^2/\varepsilon_0 m^*$ is the plasma frequency, N is the carrier density, m^* is the carrier effective mass for electron $m^* = 0.26\ m_0$ with m_0 mass of free electron, e is the charge of an electron, ε_0 is the free space permittivity, τ is the carrier collision time, ω is the angular frequency, and C_n is the fraction of the carrier's initial velocity retained after nth collision. C_n is the memory of velocity effect. For elastic collision C can be represent as $\langle \cos\theta \rangle$, where θ is the scattering angle. The value of C can vary from -1 to +1. Given the parameters $\omega_p / 2\pi = 17.5$ THz, $\tau = 0.20$ ps, C_1 = -0.98, and photo-carrier density $N = 0.99 \times 10^{18}$ cm^{-3}, the fit agrees well with the data above 0.80 THz. Negative value of C implies predominant backscattering and the net current carried by the electron system actually reverses direction before relaxing to its equilibrium value of zero. The Drude fitting can be obtained by considering C_n = 0. The inconsistency in the measured dielectric function at lower frequencies below 0.75 THz is due to the fact that the excitation laser beam is not large enough to produce a uniform distribution of carrier density across the large low-frequency terahertz beam [58]. Enlarged excitation area with increased laser power is needed to provide consistent carrier distribution if the interested resonance was located at the low-frequencies.

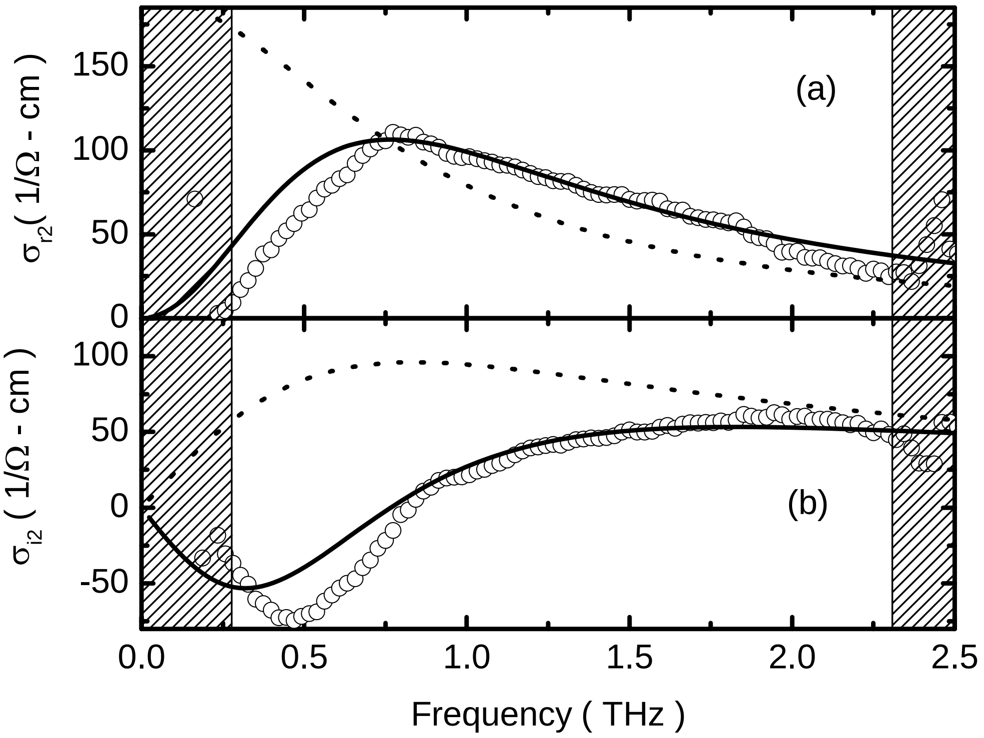

Figure 7-6 Frequency-dependent complex conductivity of the photo-excited silicon under 111-mw average power: (a) real part σ_r; (b) imaginary part σ_i. The open circles, dotted line, and solid curves represent the measured data, Drude fitting, and the Drude-Smith fitting, respectively.

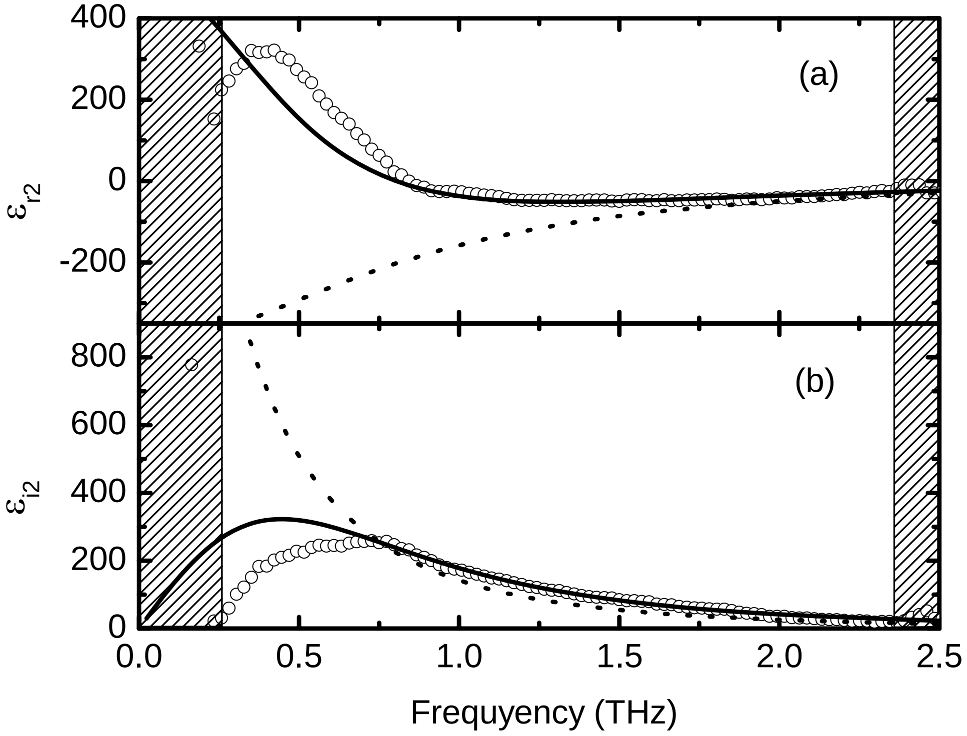

Figure 7-7 Frequency-dependent complex dielectric constant of the photo-excited silicon under 111-mw average power: (a) real part ε_{r2}; (b) imaginary part ε_{i2}. The open circles, dotted lines, and solid curves represent the measured data, Drude fitting, and the Drude-Smith fitting, respectively.

7. 4 Dynamic evolution of SPP with optical excitation

To explore the dynamic evolution of the photo-induced surface-plasmon resonance, the laser excitation power was varied from 0 to 111 mW for both array orientations. The transmission spectra and the frequency-dependent amplitude transmission for perpendicular orientation are plotted in Fig. 7-8 and the corresponding amplitude transmission is shown in Fig. 7-9. At low intensity of optical excitation, the transmission spectra are dominated by dips near 1.0 and 1.4 THz as result of complicated photonic out-of-plane dispersion. When the laser power is increased to 12.5 mW, the photonic dips nearly disappear and a resonance peak occurs near 1.6 THz, which is due to the excitation of surface plasmons. The further increase in excitation power gives rise to an enhanced terahertz transmission and a red-shift of the resonance. This red-shift is an indication that the photonic dips are totally removed by the intense laser excitation as the number density of the photogenerated free carriers is increased, and the photoexcited silicon layer becomes opaque to terahertz waves. The transmission efficiency at the surface plasmon resonance 1.5 THz is found to increase with increasing power of laser excitation. At 25 mW excitation, the maximum power transmission or transmittance of terahertz pulses is 25.5%, while it is increased to 70% under 111-mW excitation. This phenomenon can be understood that the photoexcited silicon layer shows improved metallic properties with increasing excitation intensity that favors the establishment of surface plasmon resonances.

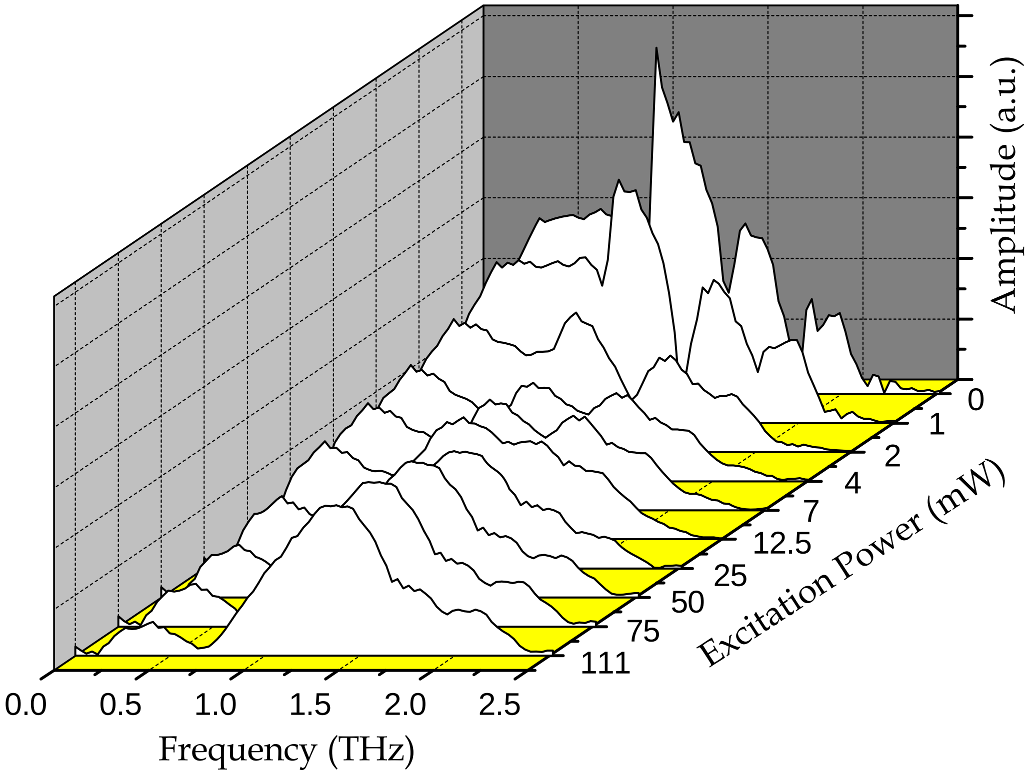

Figure 7-8 Fourier-transformed spectra of the transmitted terahertz pulses through the subwavelength silicon array of perpendicular orientation optically excited with various laser power ranging from 0 to 111 mW.

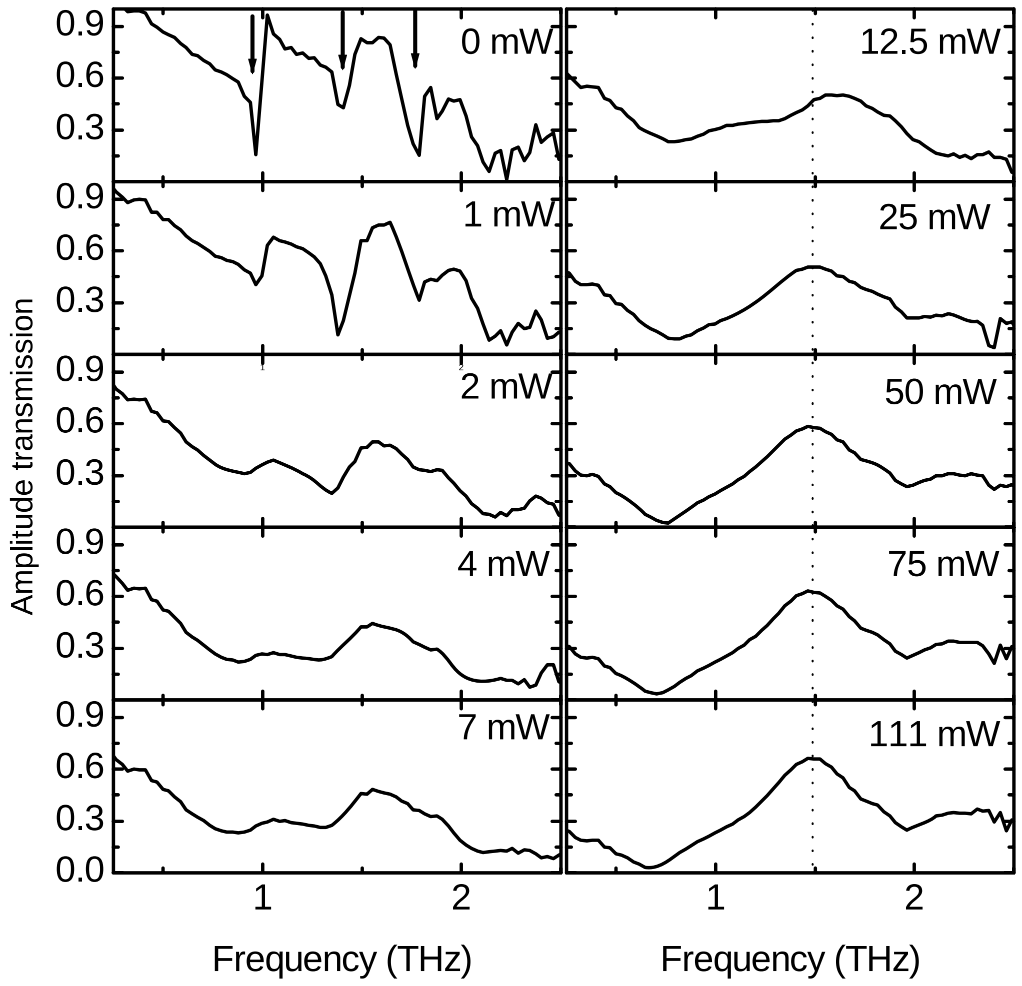

Figure 7-9 Measured amplitude transmission of the photo-excited silicon array of perpendicular orientation under various laser excitation power ranging from 0 to 111 mW. The vertical dotted line represents the SPP [±1, 0] mode. Vertical arrows show the dips of out-of-plane photonic band structure.

Three prominent dips in the transmission spectra are indicated by the arrows. These dips are not exactly the photonic band gap but the similar complicated structure has been observed in the transmission under normal incidence. It is evident from Fig. 7-9 that the strength of the dips reduces when the excitation laser power increases. Well buildup SPP [±1, 0] resonance mode due to the metal-air interface is observed for 25 mW of average power. The peak transmission then increases with the higher excitation power. The measured frequency-dependent dielectric constants are shown in Fig. 7-10.

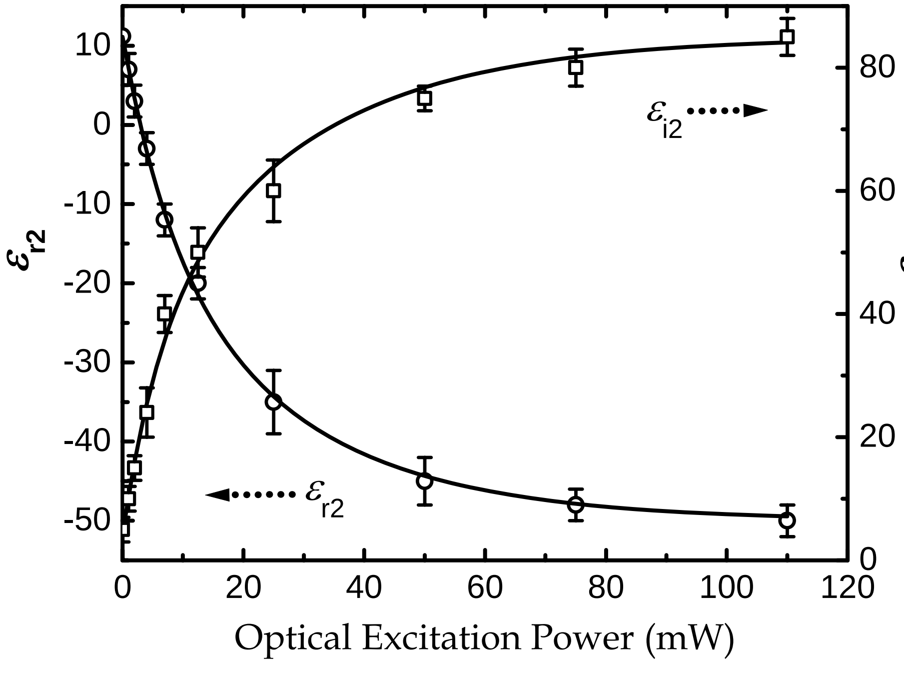

Figure 7-10 Measured dielectric constants of the photo-excited silicon for various laser excitation powers. The real and imaginary parts are represented by solid circles and solid boxes. Solid lines are to guide the eye.

The dielectric constants show exponent nature with the optical excitation power. With higher optical excitation the arrays become more metallic with higher negative value of real dielectric and boost the transmission peak. This phenomenon is opposite to the result obtained by Janke *et. al.* [52] where they used a pre-existing doping concentration capable of supporting SPPs. An InSb grating with a doping concentration of ~10^{16} cm^{-3} was excited optically to tune up the carrier concentration to 3.4×10^{17} cm^{-3}, which gave rise to a reduction in the transmission peak with a maximum switching coefficient of $-8.8 \pm 2.2 \times 10^{-3}$ at room temperature. This phenomenon was interpreted as the contraction of the effective aperture size due to modification of the finite semiconductor skin depth at increased carrier concentration.

Due to the higher optical excitation the effective hole size might be reduced. However, this contraction of the hole size is insignificant compared to the dielectric enhancement in photo-excited silicon hole arrays. With increased intensity of optical excitation, the propagation length or skin depth of terahertz waves in the photo-excited silicon layer becomes very thin. The calculated propagation length is $\delta_{THz} = 2\,\mu\text{m}$ at 1.5 THz under 111-mW excitation. In addition, a transmission minimum also occurs in the spectra at 1.95 THz due to the Wood's anomaly. The Wood's anomaly appeared at the transmission spectra when the average excitation optical power was 25 mW and became more prominent with the higher excitation which was a clear evidence of the metallic behavior of the photo-excited silicon arrays.

CHAPTER VIII

CONCLUSIONS

Demonstration of extraordinary THz transmission in subwavelength plasmonic arrays has been presented. Clearly identifiable maxima and minima appear in the transmission spectra. The peak transmittance is higher than unity when normalized to the area occupied by holes. This extraordinary transmission is successfully demonstrated as a result of resonant excitation of SPPs in the metal-dielectric interface. Incident THz radiation resonantly couples to the SPPs of metallic arrays and the SPPs squeeze and propagate through the subwavelength holes and finally re-radiate as freely propagating THz radiation on the far side of the hole arrays.

During this demonstration, effects of several parameters on the SPP-enhanced THz transmission have been studied. Effect of thickness of metallic arrays, role of the hole shape and dielectric constants of the metal and surrounding materials have been demonstrated successfully. Our doped silicon-array shows higher transmission than the predicted values. This higher value is due to the higher carrier concentration and hole shape effect. Doped semiconductor hole arrays are thus a suitable choice for use in THz plasmonic devices as their transmission properties can be changed by adjusting the doping strength or by the optical excitation.

Highly sensitive nature of the SPP-resonance frequency has been demonstrated by changing the surrounding dielectric. Resonance frequency shows red-shift and reduction in peak amplitude with surrounding dielectrics having higher permittivity.

Our observation of SPP resonances on different metals suggests that a large range of metals can be used for THz plasmonic device fabrication. Besides the electrically good conducting materials, the generally poor conducting materials, such as Pb, can also be used for efficient THz SPPs excitation.

We have also demonstrated resonant THz transmission through optically-thin metal arrays. Metal arrays require a critical thickness to establish the SPP effect. Above this thickness the peak amplitudes of SPPs start growing exponentially with thickness and saturate when array thickness reaches the skin depth. Efficient SPP-enhanced transmission is observed at array thickness of one third of the skin depth which might reduce the need of the metals for THz plasmonic devices.

Extraordinary terahertz transmission is observed in a photo-induced surface-plasmon subwavelength hole array. In general, the transmission spectrum of terahertz pulses through a static hole array made from moderately doped silicon shows typical photonic crystal effect. However, when the array is optically excited with intense laser pulses, the photo-generated free carriers alter the dielectric properties of the excited silicon layer. Consequently, the array becomes metallic and supports the coupling and propagation of surface plasmons at terahertz frequencies. By varying the optical excitation intensity, we observe a dynamic evolution of the terahertz transmission spectra between photonic bandgaps and surface-plasmon resonance. With increasing excitation, the photonic crystal effect is found to diminish while the surface plasmon resonance occurs and becomes dominant. This result offers the potential for developing all-optical, tunable plasmonic terahertz devices.

BIBLIOGRAPHY

1. T. Ebbesen, H. Lezec, H. Ghaemi, T. Thio, and P. Wolff, "Extraordinary optical transmission through sub-wavelength hole arrays," Nature (London) **391**, 667 (1998).
2. H. F. Ghaemi, T. Thio, D. E. Grupp, T. W. Ebbesen , and H. J. Lezec, "Surface plasmons enhance optical transmission through subwavelength holes," Phys. Rev. B **58**, 6779 (1998).
3. U. Schröter and D. Heitmann, "Surface-plasmon-enhanced transmission through metallic gratings," Phys. Rev. B **58**, 15 419 (1998).
4. W. –C. Tan, T. W. Preist, and R. J. Sambles, "Resonant tunneling of light through thin metal films via strongly localized surface plasmons," Phys. Rev. B **62**, 11 134 (2000).
5. L. Martín-Moreno, F. García-Vidal, H. Lezec, K. Pellerin, T. Thio, J. Pendry, and T. Ebbesen, "Theory of Extraordinary Optical Transmission through Subwavelength Hole Arrays," Phys. Rev. Lett. **86**, 1114 (2001).
6. T. Kim, T. Thio, T. Ebbesen, D. Grupp, and H. Lezec, "Control of optical transmission through metals perforated with subwavelength hole arrays," Opt. Lett. **24**, 256 (1999).

7. D. E. Grupp, H. J. Lezec, T. W. Ebbesen, K. M. Pellerin, and T. Thio, " Crucial role of metal surface in enhanced transmission through subwavelength apertures**,**" Appl. Phys. Lett. **77**, 1569 (2000).

8. E. Altewischer, M. P. Van Exter, and J. P. Woerdman, "Plasmon-assisted transmission of entangled photons**,**" Nature (London), **418**, 304 (2002).

9. W. –C. Liu and D. P. Tsai, "Optical tunneling effect of surface plasmon polaritons and localized surface plasmon resonance**,**" Phys. Rev. B. **65**, 155423 (2002).

10. K. J. K. Koerkamp, S. Enoch, F. B. Segerink, N. F. Van Hulst, and L.Kuipers, "Strong Influence of Hole Shape on Extraordinary Transmission through Periodic Arrays of Subwavelength Holes**,**" Phys. Rev. Lett. **92**, 183901 (2004).

11. R. Gordon, A. G. Brolo, A. McKinnon, A. Rajora, B. Leathem, and K. L. Kavanagh, "Strong Polarization in the Optical Transmission through Elliptical Nanohole Arrays**,**" Phys. Rev. Lett. **92**, 037401 (2004).

12. H. Lezec, A. Degiron, E. Devaux, R. Linke, L. M. Moreno, F. G. Vidal, and T. Ebbesen, "Beaming Light from a Subwavelength Aperture**,**" Science, **297**, 820 (2002).

13. F. García-Vidal, L. Martín-Moreno, H. Lezec, and T. Ebbesen, "Focusing light with a single subwavelength aperture flanked by surface corrugations**,**" Phys. Rev. Lett. **83**, 4500 (2003).

14. L. Martín-Moreno, F. García-Vidal, H. Lezec, A. Degiron, and T. Ebbesen, "Theory of Highly Directional Emission from a Single Subwavelength Aperture Surrounded by Surface Corrugations**,**" Phys. Rev. Lett. **90**, 167401 (2003).

15. W. Barnes, A. Dereux, and T. Ebbesen, “Surface plasmon subwavelength optics,” Nature (London) **424**, 824 (2003).
16. S. Shinada, J. Hashizume, and F. Koyama, “Surface plasmon resonance on microaperture vertical-cavity surface-emitting laser with metal grating,” Appl. Phys. Lett. **83**, 836 (2003).
17. D. Qu, D. Grischkowsky, and W. Zhang, “Terahertz transmission properties of thin, subwavelength metallic hole arrays,” Opt. Lett. **29**, 896 (2004).
18. H. Cao and A. Nahata, “Resonantly enhanced transmission of terahertz radiation through a periodic array of subwavelength apertures,” Opt. Express **12**, 1004 (2004).
19. D. Qu, D. Grischkowsky, “Observation of a New Type of THz Resonance of Surface Plasmons Propagating on Metal-Film Hole Arrays,” Phys. Rev. Lett. **93**, 196804 (2004).
20. H. Cao, A. Agrawal, and A. Nahata, “Influence of aperture shape on the transmission properties of a periodic array of subwavelength apertures,” Opt. Express **12**, 3664 (2004).
21. F. Miyamaru, and M. Hangyo, “Finite size effect of transmission property for metal hole arrays in subterahertz region,” Appl. Phys. Lett. **84**, 2742 (2004).
22. H. Cao, A. Agrawal, and A. Nahata, “Controlling the transmission resonance lineshape of a single subwavelength aperture,” Opt. Express **13**, 763 (2005).
23. A. K. Azad and W. Zhang, “Resonant terahertz transmission in subwavelength metallic hole arrays of sub-skin-depth thickness,” Opt. Lett. **30**, 2945 (2005).

24. J. Saxler, J. G. Rivas, C. Janke, H. P. M. Pellemans, P.H. Bolver, and H. Kurz, "Time-domain measurements of surface plasmon polaritons in the terahertz frequency range," Phys. Rev. B **69**, 155427 (2004)

25. J. Gómez Rivas, C. Schotsch, P. Haring Bolivar, and H. Kurz, "Enhanced transmission of THz radiation through subwavelength holes," Phys. Rev. B **68**, 201306 (2004)

26. C Janke, J. G. Rivas, C. Schotch, L. Beckmann, P. H. Bolivar, and H. Kurz, "Optimization of enhanced terahertz transmission through arrays of subwavelength apertures," Phys. Rev. B **69**, 205314 (2004)

27. A. K. Azad, Y. Zhao, and W. Zhang, "Transmission properties of terahertz pulses through an ultrathin subwavelength silicon hole array," Appl. Phys. Lett. **86**, 141102 (2005).

28. J. Gómez Rivas, P. Haring Bolivar, and H. Kurz, "Thermal switching of the enhanced transmission of terahertz radiation through subwavelength apertures," Opt. Lett. **29**, 1680-1682 (2004).

29. J. Gómez Rivas, C. Janke, P. Haring Bolivar, and H. Kurz, "Transmission of THz radiation through InSb gratings of subwavelength apertures," Opt. Exp. **13**, 847-859 (2005).

30. R. Mendis and D. Grischkowsky, "THz Interconnect with Low Loss and Low Group Velocity Dispersion," IEEE Microw. Wirel. Compon. Lett. **11**, 444 (2001).

31. J. Dai, S. Colman, and D. Grischkowsky, "Planar THz quasioptics," Appl. Phys. Lett. **85**, 884 (2004).

32. R. H. Ritchie, "Plasma Losses by Fast Electrons in Thin Films**,**" Phys. Rev. **106**, 874 (1957).

33. Jorg Saxler, Diploma Thesis , November (2003).

34. H. Raether, *Surface plasmons on smooth and rough surfaces and on gratings* (Springer-Verlag, Berlin, 1988).

35. J. F. O'Hara, R. D. Averitt, and A. J. Taylor, "Terahertz surface plasmon polariton coupling on metallic gratings**,**" Opt. Express. **12**, 6397 (2004)

36. J. F. O'Hara, R. D. Averitt, and A. J. Taylor, "Prism coupling to terahertz surface plasmon polaritons**,**" Opt. Express. **13**, 6117 (2005)

37. R. Mendis, Ph. D. Thesis, "First Broadband Experimental study of planar Terahertz Waveguides," December (2001).

38. D. Grischkowsky, S. Keiding, M. van Exter, and Ch. Fattinger, "Far-Infrared Time-Domain Spectroscopy with Terahertz Beams of Dielectrics and Semiconductors**,**" J. Opt. Soc. Am. B **7**, 2006 (1990).

39. L. Thamizhmani, A. K. Azad, J. Dai, W. Zhang, "Far-infrared optical and dielectric response of ZnS measured by terahertz time-domain spectroscopy**,**" Appl. Phys. Lett. **86**, 131111 (2005).

40. H. Bethe, "Theory of Diffraction by Small Holes**,**" Phys. Rev. **66**, 163 (1944).

41. T. –I. Jeon, D. Grischkowsky, "Nature of Conduction in Doped Silicon**,**" Phys. Rev. Lett. **78**, 1106 (1997).

42. T. Thio, H. Ghaemi, H. Lezec, P. Wolff, and T. Ebbesen, "Surface-plasmon-enhanced transmission through hole arrays in Cr films**,**" J. Opt. Soc. Am. B **16**, 1743 (1999).

43. C. Janke, J. G. Rivas, C. Schotch, L. Beckmann, P. H. Bolivar, and H. Kurz, "Optimization of enhanced terahertz transmission through arrays of subwavelength apertures," Phys. Rev. B **69**, 205314 (2004).

44. R. Gordon, A. G. Brolo, A. McKinno, A. Rajora, B. Leathem, K. L. Kanagh, "Strong Polarization in the Optical Transmission through Elliptical Nanohole Arrays," Phys. Rev. Lett. **92**, 037401 (2004).

45. R. W. Wood, "Anomalous Diffraction Gratings," Phys. Rev. B **48**, 928 (1935).

46. M. A. Ordal, L. L. Long, R. J. Bell, S. E. Bell, R. R. Bell, R. W. Alexander, Jr., and C. A. Ward, "Optical properties of the metals Al, Co, Cu, Au, Fe, Pb, Ni, Pd, Pt, Ag, Ti, and W in the infrared and far infrared," Appl. Opt. **22**, 1099 (1983).

47. X. Y. Liu, M. S. Daw, J. D. Kress, D. E. Hanson, V. Arunchalam, D. G. Coronell, C. L. Liu, and A. F. Voter, "Ion solid surface interactions in ionized copper physical vapor deposition," Thin Solid Films **422**, 141 (2002).

48. C. Buzea, K. Kaminska, G. Beydaghyan, T. Brown, C. Elliott, C. Dean, and K. Robbie, "Thickness and density evaluation for nanostructured thin films by glancing angle deposition," J. Vac. Sci. Technol. B, 23, 2545 (2005).

49. D. E. Starr, J. T. Ranney, J. H. Larsen, J. E. Musgrove, and C. T. Campbell, "Measurement of the Energetics of Metal Film Growth on a Semiconductor: *Ag/Si*(100)-(2×1)," Phys. Rev. Lett. 87, 106102 (2001).

50. L. Pan, C. F. Hsieh, R. P. Pan, M. Tanaka, F. Miyamaru, M. Tani, and M. Hangyo, "Control of enhanced THz transmission through metallic hole arrays using nematic liquid crystal," Opt. Express, **13**, 3921 (2005).

51. J. G. Rivas, P. H. Bolivar, and H. Kurz, “Thermal switching of the enhanced transmission of terahertz radiation through subwavelength apertures**,**” Opt. Lett. **29**, 1680 (2004).

52. C. Janke, J. G. Rivas, P. H. Bolivar, and H. Kurz, “All optical switching of the transmission of electromagnetic radiation through subwavelength apertures**,**” Opt. Lett. **30**, 2357 (2005).

53. B. I. Greene, John F. Federici, D. R. Dykaar, A. F. J. Levi, L. Pfeiffer, “Picosecond pump and probe spectroscopy utilizing freely propagating terahertz radiation**,**” Opt. Lett. **16**, 48 (1991).

54. G. P. Agrawal, Govind P. Agrawal, *Fiber-Optic Communication Systems* (Wiley Series in Microwave and Optical Engineering).

55. A. H. L. Rosa, B. I. Yakobson, and H. D. Hallen, “Optical imaging of carrier dynamics in silicon with subwavelength resolution**,**” Appl. Phys. Lett. **70**, 1656 (1997).

56. Z. Jian and D. Mittleman, “Out-of-plane dispersion and homogenization in photonic crystal slabs**,**” Appl. Phys. Lett. **87**, 191113 (2005).

57. N. V. Smith, “Classical generalization of the Drude formula for the optical conductivity**,**” Phys. Rev. B. **64**, 155106 (2001).

58. M. C. Beard, G. M. Turner, and C. A. Schmuttenmear, “Transient photoconductivity in GaAs as measured by time-resolved terahertz spectroscopy**,**” Phys. Rev. B **62**, 15764 (2000).

APPENDIX

Appendix A

Dispersion relation of SPP in smooth surface

Maxwell's equation and the material properties in Gaussian system can be written as,

$$\begin{aligned}
\nabla \times \boldsymbol{E} &= -\frac{1}{c}\frac{\partial}{\partial \boldsymbol{t}}\boldsymbol{H} \\
\nabla \times \boldsymbol{H} &= \frac{\varepsilon}{c}\frac{\partial}{\partial \boldsymbol{t}}\boldsymbol{E} \\
\nabla \bullet \boldsymbol{D} &= 0 \\
\nabla \bullet \boldsymbol{B} &= 0
\end{aligned} \qquad \text{(A-1)}$$

$$\begin{aligned}
\boldsymbol{D} &= \varepsilon \boldsymbol{E} \\
\boldsymbol{B} &= \boldsymbol{H}
\end{aligned}$$

where, ***E*** is the electric field density, ***H*** is the magnetic field density, ***D*** is the electric flux density and ***B*** is the magnetic flux density, c is the speed of light in vacuum, and ε is the material permittivity.

As described in Fig. 2-2, the electromagnetic wave properties related to the SPPs on a metal-dielectric interface can be described completely by three field components, which are $\boldsymbol{E_x}$, $\boldsymbol{E_z}$, and $\boldsymbol{H_y}$. The general form of the electric field can be written as,

$$\boldsymbol{E} = \boldsymbol{E}_0^{\pm} \exp\left[+i\left(k_x x \pm k_z z - \omega t\right)\right] \tag{A-2}$$

where, + for z ≥ 0 in medium 1, - for z ≤ 0 in medium 2, k_z is the imaginary wave vector along z-direction ,and k_x is the wave vector along x-direction. The fields in medium 1 and medium 2 can be written as,

$$\begin{aligned} \boldsymbol{E_{x1}} &= \hat{x}E_{x1} \exp\left[+i\left(k_{x1}x + k_{z1}z - \omega t\right)\right] \\ \boldsymbol{E_{z1}} &= \hat{z}E_{z1} \exp\left[+i\left(k_{x1}x + k_{z1}z - \omega t\right)\right] \quad z > 0 \\ \boldsymbol{H}_1 &= \hat{y}H_{y1} \exp\left[+i\left(k_{x1}x + k_{z1}z - \omega t\right)\right] \end{aligned} \tag{A-3}$$

$$\begin{aligned} \boldsymbol{E_{x2}} &= \hat{x}E_{x2} \exp\left[+i\left(k_{x2}x - k_{z2}z - \omega t\right)\right] \\ \boldsymbol{E}_{z2} &= \hat{z}E_{z2} \exp\left[+i\left(k_{x2}x - k_{z2}z - \omega t\right)\right] \quad z < 0 \\ \boldsymbol{H}_2 &= \hat{y}H_{y2} \exp\left[+i\left(k_{x2}x - k_{z2}z - \omega t\right)\right] \end{aligned} \tag{A-4}$$

Second equation of Eq. A-1 gives,

$$\nabla \times \boldsymbol{H} = \frac{\boldsymbol{-i}\omega\varepsilon}{\boldsymbol{c}}\boldsymbol{E} \tag{A-5}$$

and,

$$\nabla \times \boldsymbol{H} = -\hat{x}\left(\frac{\partial H_y}{\partial z}\right) + \hat{z}\left(\frac{\partial H_y}{\partial x}\right) \tag{A-6}$$

By comparing the components of A-5 and A-6,

$$-\frac{\partial \boldsymbol{H}_1}{\partial z} = \frac{-i\omega\varepsilon_1}{c} E_{x1} \exp\left[+i\left(k_{x1}x + k_{z1}z - \omega t\right)\right]$$

$$k_{z1}H_{y1} = \frac{\omega\varepsilon_1}{c} E_{x1} \tag{A-7}$$

and,
$$\frac{\partial \boldsymbol{H}_1}{\partial x} = \frac{-i\omega\varepsilon_1}{c} E_{z1} \exp[+i(k_x x + k_z z - \omega t)]$$
$$k_{x1} H_{y1} = \frac{-\omega\varepsilon_1}{c} E_{z1} \tag{A-8}$$

Similar way it is possible to show that

$$k_{z2} H_{y2} = -\frac{\omega\varepsilon_2}{c} E_{x2}$$
$$k_{x2} H_{y2} = \frac{\omega\varepsilon_2}{c} E_{z2} \tag{A-9}$$

From the boundary conditions described in chapter 2, the continuity relations can be written as,

$$\begin{aligned} E_{x1} &= E_{x2} \\ H_{y1} &= H_{y2} \\ \varepsilon_1 E_{z1} &= \varepsilon_2 E_{z2} \\ k_{x1} &= k_{x2} = k_x \end{aligned} \tag{A-10}$$

From A-7, A-9, and A-10 we can write,

$$\begin{aligned} \frac{k_{z1}}{\varepsilon_1} H_{y1} + \frac{k_{z2}}{\varepsilon_2} H_{y2} &= 0 \\ \frac{k_{z1}}{\varepsilon_1} &= -\frac{k_{z2}}{\varepsilon_2} \end{aligned} \tag{A-11}$$

Using the first equation of Eq. A-1,

$$\nabla \times \boldsymbol{E} = -\frac{1}{c}\frac{\partial}{\partial \boldsymbol{t}} \boldsymbol{H} \tag{A-12}$$

$$\nabla \times \boldsymbol{E} = \hat{x}\left(\frac{\partial \boldsymbol{E_z}}{\partial y}\right) + \hat{y}\left(\frac{\partial \boldsymbol{E_x}}{\partial z} - \frac{\partial \boldsymbol{E_z}}{\partial x}\right) - \hat{z}\left(\frac{\partial \boldsymbol{E_x}}{\partial y}\right) \tag{A-13}$$

Computing the components of Eq. A-12 and A-13, for z > 0,

$$\left(\frac{\partial \boldsymbol{E}_{x1}}{\partial z}-\frac{\partial \boldsymbol{E}_{z1}}{\partial x}\right)=\frac{i\omega}{c}H_{y1}\exp\left[+i\left(k_{x1}x+k_{z1}z-\omega t\right)\right]$$

$$(E_{x1}ik_{z1}+E_{z1}ik_{x1})=\frac{i\omega}{c}H_{y1} \tag{A-14}$$

For, z < 0, $$(-E_{x2}ik_{z2}+E_{z2}ik_{x2})=\frac{i\omega}{c}H_{y2} \tag{A-15}$$

Third equation of Eq. A-1 gives

For z > 0 $$E_{x1}=-E_{z1}\frac{k_{z1}}{k_{x1}} \tag{A-16}$$

For z < 0 $$E_{x2}=E_{z2}\frac{k_{z2}}{k_{x2}}$$

Now substituting these values,

$$k_x^2=\varepsilon_1\left(\frac{\omega}{c}\right)^2-k_{z1}^2$$

$$k_x^2=\varepsilon_2\left(\frac{\omega}{c}\right)^2-k_{z2}^2 \tag{2-17}$$

Eq. A-17 gives

$$\varepsilon_1\left(\frac{\omega}{c}\right)^2-k_{z1}^2=\varepsilon_2\left(\frac{\omega}{c}\right)^2-\left(-k_{z1}\frac{\varepsilon_2}{\varepsilon_1}\right)^2$$

$$k_{z1}^2=\left(\frac{\omega}{c}\right)^2\frac{\varepsilon_1^2}{\varepsilon_1+\varepsilon_2} \tag{A-18}$$

By replacing the value of *k_{z1}*

$$k_x^2=\varepsilon_1\left(\frac{\omega}{c}\right)^2-\left(\frac{\omega}{c}\right)^2\frac{\varepsilon_1^2}{\varepsilon_1+\varepsilon_2}$$

$$k_x^2=\left(\frac{\omega}{c}\right)^2\left(\varepsilon_1-\frac{\varepsilon_1^2}{\varepsilon_1+\varepsilon_2}\right)$$

which finally gives, $$k_x=\frac{\omega}{c}\sqrt{\frac{\varepsilon_1\varepsilon_2}{\varepsilon_1+\varepsilon_2}} \tag{A-19}$$

Appendix B

Propagation length of SPP on smooth surface at THz

Dispersion relation,

$$k_x = \frac{\omega}{c}\left(\frac{\varepsilon_1\varepsilon_2}{\varepsilon_1+\varepsilon_2}\right)^{\frac{1}{2}} = k'_x + ik''_x \qquad \text{(B-1)}$$

where, $\varepsilon_1 = \varepsilon'_1 + i\varepsilon''_1$ is the dielectric constant of metal and ε_2 is the dielectric constant of the surrounding medium. As stated in chapter 5 the propagation length of the SPP is given by, $L_x = 1/2k_x^{//}$.

$$\frac{\varepsilon_1\varepsilon_2}{\varepsilon_1+\varepsilon_2} = \varepsilon_2\frac{\varepsilon'_1 + i\varepsilon''_1}{\varepsilon'_1+\varepsilon_2+i\varepsilon''_1}$$

$$= \varepsilon_2\frac{(\varepsilon'_1+i\varepsilon''_1)(\varepsilon'_1+\varepsilon_2-i\varepsilon''_1)}{(\varepsilon'_1+\varepsilon_2+i\varepsilon''_1)(\varepsilon'_1+\varepsilon_2-i\varepsilon''_1)}$$

$$= \varepsilon_2\frac{\varepsilon'^2_1+\varepsilon'_1\varepsilon_2+\varepsilon''^2_1+i\varepsilon''_1\varepsilon_2}{(\varepsilon'_1+\varepsilon_2)^2+\varepsilon''^2_1}, \qquad \varepsilon_2 << \varepsilon_1$$

$$= \varepsilon_2\frac{\varepsilon'^2_1+\varepsilon''^2_1+i\varepsilon''_1\varepsilon_2}{\varepsilon'^2_1+\varepsilon''^2_1}, \qquad \varepsilon''_1 > |\varepsilon'_1|$$

$$= \varepsilon_2\frac{\varepsilon''^2_1+i\varepsilon''_1\varepsilon_2}{\varepsilon''^2_1}$$

$$= \varepsilon_2\left(1+i\frac{\varepsilon_2}{\varepsilon''_1}\right)$$

$$= \varepsilon_2(1+x) \qquad \text{(B-2)}$$

where, $x = i\dfrac{\varepsilon_2}{\varepsilon_1''}$, then

$$\left(\frac{\varepsilon_1\varepsilon_2}{\varepsilon_1+\varepsilon_2}\right)^{\frac{1}{2}} = \sqrt{\varepsilon_2}\sqrt{1+x} = \sqrt{\varepsilon_2}\left(1+\frac{1}{2}x\right) \tag{B-3}$$

$$\sqrt{1+x} = 1+\frac{1}{2}x-\frac{1}{2\cdot 4}x^2+\frac{1\cdot 3}{2\cdot 4\cdot 6}x^3-\frac{1\cdot 3\cdot 5}{2\cdot 4\cdot 6\cdot 8}x^4+\ldots \qquad (-1 < x < 1)$$

then

$$\left(\frac{\varepsilon_1\varepsilon_2}{\varepsilon_1+\varepsilon_2}\right)^{\frac{1}{2}} = \sqrt{\varepsilon_2}\left(1+i\frac{\varepsilon_2}{2\varepsilon_1''}\right),$$

$$= \sqrt{\varepsilon_2}+i\frac{\varepsilon_2^{3/2}}{2\varepsilon_1''} \tag{B-4}$$

Therefore,

$$k_x = \frac{\omega}{c}\left(\frac{\varepsilon_1\varepsilon_2}{\varepsilon_1+\varepsilon_2}\right)^{\frac{1}{2}} = k_x' + ik_x'' = \frac{\omega}{c}\left(\sqrt{\varepsilon_2}+i\frac{\varepsilon_2^{3/2}}{2\varepsilon_1''}\right) \tag{B-5}$$

$$k_x' = \frac{\omega}{c}\sqrt{\varepsilon_2} \tag{B-6}$$

$$k_x'' = \frac{\omega}{c}\frac{\varepsilon_2^{3/2}}{2\varepsilon_1''} \tag{B-7}$$

$$L_x = \frac{c}{\omega}\frac{\varepsilon_1''}{\varepsilon_2^{3/2}} \tag{B-8}$$

Appendix C

Skin depth of THz SPP inside metal

Skin depth δ_m is defined as,

$$\delta_m(\omega) = \frac{1}{\mathrm{Im}(k_{zm})} \tag{C-1}$$

At THz frequencies $\varepsilon_1 << \varepsilon_m$ and $\varepsilon_{im} > |\varepsilon_{rm}|$, Eq. 6-2 can be written as,

$$\begin{aligned}
k_{zm} = \mathrm{Re}(k_{zm}) + i\,\mathrm{Im}(k_{zm}) &= \left[\varepsilon_m\left(\frac{\omega}{c}\right)^2 - k_x^2\right]^{1/2} \\
&= \left[\varepsilon_m\left(\frac{\omega}{c}\right)^2 - \left(\frac{\omega}{c}\right)^2 \frac{\varepsilon_m\varepsilon_1}{\varepsilon_m + \varepsilon_1}\right]^{1/2} \\
&= \left(\frac{\omega}{c}\right)\left[\varepsilon_m - \frac{\varepsilon_m\varepsilon_1}{\varepsilon_m + \varepsilon_1}\right]^{1/2} \\
&= \left(\frac{\omega}{c}\right)\left[\frac{\varepsilon_m^2 + \varepsilon_m\varepsilon_1 - \varepsilon_m\varepsilon_1}{\varepsilon_m + \varepsilon_1}\right]^{1/2} \\
&= \left(\frac{\omega}{c}\right)\left[\frac{\varepsilon_m^2}{\varepsilon_m + \varepsilon_1}\right]^{1/2} \\
&= \left(\frac{\omega}{c}\right)\sqrt{\varepsilon_m}
\end{aligned}$$

$$\mathrm{Re}(k_{zm}) + i\,\mathrm{Im}(k_{zm}) = \left(\frac{\omega}{c}\right)\sqrt{\varepsilon_{rm} + i\varepsilon_{im}}$$

$$= \left(\frac{\omega}{c}\right)\sqrt{i\varepsilon_{im}}\sqrt{1+\left(\frac{\varepsilon_{rm}}{i\varepsilon_{im}}\right)}, \text{ but } \left|\frac{\varepsilon_{rm}}{\varepsilon_{im}}\right| < 1$$

$$\sqrt{1+x} = 1 + \frac{1}{2}x - \frac{1}{2\cdot 4}x^2 + \frac{1\cdot 3}{2\cdot 4\cdot 6}x^3 - \frac{1\cdot 3\cdot 5}{2\cdot 4\cdot 6\cdot 8}x^4 + \ldots \qquad (-1 < x < 1)$$

$$= \left(\frac{\omega}{c}\right)\sqrt{i\varepsilon_{im}}\sqrt{1+\left(\frac{\varepsilon_{rm}}{i\varepsilon_{im}}\right)}$$

$$= \left(\frac{\omega}{c}\right)\sqrt{i\varepsilon_{im}}\left(1+\frac{\varepsilon_{rm}}{i2\varepsilon_{im}}\right)$$

$$= \frac{1}{\sqrt{2}}(1+i)\left(\frac{\omega}{c}\right)\sqrt{\varepsilon_{im}}\left(1+\frac{\varepsilon_{rm}}{i2\varepsilon_{im}}\right) \;;\sqrt{i} = \frac{1}{\sqrt{2}}(1+i)$$

$$= \frac{1}{\sqrt{2}}(1+i)\left(\frac{\omega}{c}\right)\sqrt{\varepsilon_{im}}\left(1+\frac{\varepsilon_{rm}}{i2\varepsilon_{im}}\right)$$

$$= \frac{1}{\sqrt{2}}\left(\frac{\omega}{c}\right)\sqrt{\varepsilon_{im}}\left[\left(1+\frac{\varepsilon_{rm}}{2\varepsilon_{im}}\right)+i\left(1-\frac{\varepsilon_{rm}}{2\varepsilon_{im}}\right)\right]$$

Which gives, $\mathrm{Im}(k_{zm}) = \frac{1}{\sqrt{2}}\left(\frac{\omega}{c}\right)\sqrt{\varepsilon_{im}}\left[\left(1-\frac{\varepsilon_{rm}}{2\varepsilon_{im}}\right)\right],$ but, $\left|\frac{\varepsilon_{rm}}{2\varepsilon_{im}}\right| << 1$

$$\mathrm{Im}(k_{zm}) = \left(\frac{\omega}{c}\right)\sqrt{\frac{\varepsilon_{im}}{2}} \qquad \text{(C-2)}$$

Skin depth,

$$\delta_m(\omega) = \left(\frac{c}{\omega}\right)\sqrt{\frac{2}{\varepsilon_{im}}} \qquad \text{(C-3)}$$

VITA

Md. Abul Kalam Azad

Candidate for the Degree of

Doctor of Philosophy of Science

Thesis: RESONANT TERAHERTZ TRANSMISSION OF PLASMONIC SUBWAVELENGTH HOLE ARRAYS

Major Field: Electrical Engineering

Biography:

Personal Data: Born in Dhaka, Bangladesh, on 1st January, 1970, son of Mozaffar Hossein and Abishkar.

Education: Graduated from Devendra College, Dhaka, Bangladesh, in October 1988; received Bachelor of Science degree with honors in Physics from University of Dhaka, Dhaka, Bangladesh in May 1996; received Master of Science in Electrical Engineering from Oklahoma State University, Stillwater, Oklahoma in May 2003. Completed the requirements for the Doctor of Philosophy of Science degree with a major in Electrical Engineering at Oklahoma State University in May, 2006.

Experiences: Employed by Optics laboratory, University of Dhaka, Dhaka, Bangladesh, as a research assistant; employed by UNICEF, Dhaka, Bangladesh as a computer programmer; employed by Beximco Textiles, Dhaka, Bangladesh, as a communication engineer; employed by Oklahoma State University, Department of Physics as a teaching assistant, 2000 to 2001; employed by Oklahoma State University, Department of Electrical Engineering as a research assistant, 2001 to present.

Name: Md. Abul Kalam Azad Date of Degree: May, 2006

Institution: Oklahoma State University Location: Stillwater, Oklahoma

Title of Study: RESONANT TERAHERTZ TRANSMISSION OF PLASMONIC SUBWAVELENGTH HOLE ARRAYS

Pages in Study: 130 Candidate for the Degree of Doctor of Philosophy of Science

Major Field: Electrical and Computer Engineering

Scope and Method of Study: The purpose of this study was to examine the extraordinary terahertz (THz) transmission through subwavelength hole arrays structured on metals, highly doped and photo-doped silicon. Conventional photolithography process was used to structure subwavelength hole arrays on good and poor metallic conductors as well as on thin, doped silicon wafers. The transmission properties of the THz radiation through these hole arrays were investigated using terahertz time-domain spectroscopy (THz-TDS) and optical pump-THz probe techniques.

Findings and Conclusions: The frequency-dependent transmission spectra through hole arrays show extraordinary transmission at resonance peaks. This phenomenon is attributed to the resonance excitation of surface plasmon polaritos (SPPs) which might find applications in THz photonic devices. The incident THz radiation excites SPPs on the incidence surface of the array; the SPPs then tunnel through the subwavelength holes and reradiate as THz radiation from the other surface. This study demonstrated the effect of hole shape, dielectric properties of the metallic and surrounding media, polarization dependence, and the metal thickness on the enhanced THz transmission. Rectangular and elliptical hole shapes show higher peak transmission when the polarization of incident THz beam is perpendicular to the longer axis of the holes. Amplitude of the peak resonance decreases and shifts toward the lower frequencies when the dielectric constant of the surrounding medium increases. Efficiently enhanced transmission has been realized with the metallic arrays having thickness of one-third of the skin depth. For similar array, transmission is higher for the array made from metals having higher electrical conductivity. Furthermore, the transmission properties of a lightly doped silicon hole array can be dynamically tuned from two-dimensional photonic crystal features to SPPs resonance with increased photo-doping density by varying external optical excitation power.

ADVISER'S APPROVAL: ______________________________